

**Length-controlled Gas-liquid Segment Flow in
Microchannel and Application to NanoFe₃O₄ Synthesis**

JIANG XIAOYANG

2023

Abstract

Segmented flow, one of the most important flow patterns in microchannels, has been widely employed in gas–liquid microreactor systems because it enhances mass transfer through the biphasic interface. The segment length is determined by the channel parameters (e.g., size, material type), fluid flow rate (F), and fluid properties. Thus, it is difficult to manipulate the gas–liquid segment length without affecting the residence time of the fluid.

Previous studies evaluating an increased F have reported an increased volumetric mass transfer coefficient ($k_L a$) and reduced segment length (L). However, the relationship between $k_L a$ and L has not been systemically investigated under the same F .

Magnetic Fe₃O₄ nanoparticles boast wide-ranging applications from magnetic separation to imaging, labeling, and remote control of targeted drug delivery. However, the conventional Fe₃O₄ nanoparticles synthesis in a batch reactor is time- and energy-intensive. In the currently developed continuous synthesis strategies, the complexity of the rotating packed bed reactor and the low capacity of the microfluidic chip impedes the application of these devices for the fabrication of Fe₃O₄ nanoparticles. Hence, for the continuous synthesis of Fe₃O₄ nanoparticles, a simple and convenient device with high throughput is urgently required.

In this work we successfully achieved regularly segment length control by introducing a high-speed valve into a gas–liquid microchannel system. Varying the frequency of the valve (f) installed in the gas-phase tube to allow gas and liquid segment lengths to be controlled within a large range. Furthermore, a gas/liquid flow rate ratio in the range of 0.7–1.2 was deemed necessary for steady segmented flow. Finally, a correlation was proposed to predict L using parameters such as f and F , and it matched the experimental data well.

Subsequently, the influence of L on $k_L a$ is investigated by altering the valve frequency f . The results indicate that $k_L a$ in the segmented flow is negatively correlated with L at constant F and reaches 0.149 s^{-1} (332.6 times larger than that in the bubble), whereas the specific area (a) of the segmented flow increases with increasing f before the liquid phase is saturated. Moreover, a and $k_L a$ can be predicted using f , F , and the microchannel diameter.

By leveraging the benefits of segmented flow, continuous synthesis of Fe_3O_4 nanoparticles was achieved in microchannel, utilizing the coprecipitation method. The influence of iron concentration, reaction temperature, and the $\text{Fe}^{2+}:\text{Fe}^{3+}$ ratio on the synthesis of Fe_3O_4 nanoparticles were investigated thoroughly. This segmented flow synthesis strategy was proved to be capable of fabricating Fe_3O_4 nanoparticles of approximately 6 nm. Moreover, by increasing f , thus reducing L , the size distribution range of nanoparticles was reduced and uniform nanoparticles were synthesized.

The continuous synthesis of Fe_3O_4 nanoparticles was extended through a process of partial oxidation coprecipitation of Fe^{2+} within the gas-liquid segmented flow. The optimum conditions for nucleating agent addition, oxidation time, acid additive source, and $\text{H}^+:\text{Fe}^{2+}$ and $\text{OH}^+:\text{Fe}^{2+}$ ratios were determined through different experiments. The results indicate that adding a nucleating agent to the NaOH solution and HCl to the FeCl_2 solution, with an oxidation time of 19.2 s and a $\text{H}^+:\text{OH}^+:\text{Fe}^{2+}$ ratio of 0.67:8.5:1, yields Fe_3O_4 nanoparticles with diameters of approximately 8 nm and a narrow size distribution range of 5–13 nm.

The results of this research will not only enhance the efficiency of gas-liquid reactions within microreactors, but also deepen our grasp of mass transfer phenomena in gas-liquid segmented flows. Moreover, our developed continuous synthesis method for Fe_3O_4 nanoparticles presents substantial advantages in terms of both productivity and manufacturing cost compared to existing technologies. This positions it as a promising avenue for large-scale, continuous production in industrial settings. These advancements also make notable contributions to the broader understanding of microreactor systems and

propel advancements in microreactor system design.

Key words: multiphase flow; high-speed valve; segment length control; continuous synthesis; nanoparticle

Content

Abstract	I
Content	V
Nomenclature	IX
1 Introduction	1
1.1 Microreactor.....	1
1.1.1 Development of microreactor.....	1
1.1.2 Advantages of microreactor	4
1.1.3 Flow types in microreactor.....	6
1.2 Segmented flow	10
1.2.1 Formation mechanism	10
1.2.2 Characteristics	11
1.2.3 Mass transfer in segmented flow.....	12
1.2.4 Application of segmented flow	14
1.3 Segment length control	15
1.3.1 By changing flow rate	16
1.3.2 By using valve.....	17
1.3.3 By other methods	19
1.3.4 Research gaps.....	20
1.4 Fe ₃ O ₄ nanoparticle	20
1.4.1 Background	20
1.4.2 Conventional synthesis methods	21
1.4.3 Continuous synthesis methods	22
1.4.4 Research gaps.....	24
1.5 Research plan.....	25
1.5.1 Objectives.....	25

Content

1.5.2 Strategies and outlines of the thesis	25
Part I: Strategy of Segment Length Control and Mass Transfer Measurement	27
2 Methodology.....	29
2.1 Experimental set-up	29
2.1.1 Apparatus and instruments	29
2.1.2 High-speed valve.....	30
2.1.3 Segmented flow generation system.....	31
2.2 Methods	33
2.2.1 Chemicals	33
2.2.2 Measurement of segment length	33
2.2.3 Evaluation of mass transfer	35
2.2.4 Fundamental correlations	37
2.3 Preparation and characterization.....	39
3 Segment Length Control by Using a High-speed Valve	41
3.1 Segment lengths at low frequencies.....	41
3.1.1 Influence of valve frequency on segment length	41
3.1.2 Reproducibility.....	43
3.2 Segment lengths at higher frequencies	45
3.2.1 Experimental results.....	45
3.2.2 Explanation based on segment formation mechanism	47
3.3 Influence of flow rate on segment length	50
3.3.1 By changing flow rate ratio	50
3.3.2 By changing total flow rate	51
3.4 Correlation for predicting segment length	53
3.5 Conclusions.....	55
4 Mass Transfer Measurement in Length-controlled Segmented Flow	57
4.1 Influence of valve frequency on volumetric mass transfer coefficient.....	57
4.2 Influence of tube length on volumetric mass transfer coefficient.....	59
4.3 Influence of segment length on instinct volumetric mass transfer coefficient ..	62

Content

4.4 Influence of valve frequency on the specific area	64
4.5 Conclusion	68
Part II: Continuous Synthesis of Size-controlled Fe₃O₄ Nanoparticles in Segmented Flow.....	69
5 Continuous Synthesis of Size-controlled NanoFe₃O₄ by Coprecipitation	71
5.1 Experimental.....	71
5.1.1 Experimental setup.....	71
5.1.2 Chemicals	73
5.1.3 Strategy for continuous operation	73
5.2 Continuous synthesis of nanoFe ₃ O ₄	74
5.3 Influence of iron concentration on nanoFe ₃ O ₄ synthesis.....	77
5.4 Influence of temperature on nanoFe ₃ O ₄ synthesis.....	79
5.5 Influence of Fe ²⁺ :Fe ³⁺ ratio on nanoFe ₃ O ₄ synthesis.....	81
5.6 Influence of valve frequency on nanoFe ₃ O ₄ size.....	82
5.7 Principle of coprecipitation in segmented flow	85
5.8 Comparison with other synthesis methods	86
5.9 Conclusions.....	89
6 Continuous Synthesis of NanoFe₃O₄ by Partial Oxidation Coprecipitation	91
6.1 Experimental.....	92
6.1.1 Experimental setup.....	92
6.1.2 Chemicals	93
6.1.3 Strategy of partial oxidation and continuous coprecipitation in the microchannel	94
6.2 Influence of the nucleating agent addition method on Fe ₃ O ₄ nanoparticle formation.....	95
6.3 Influence of oxidation time on Fe ₃ O ₄ nanoparticle formation.....	99
6.4 Influence of acid additives on Fe ₃ O ₄ nanoparticle formation.....	101
6.5 Influence of H ⁺ :Fe ²⁺ ratio on the Fe ₃ O ₄ nanoparticle size.....	104
6.6 Influence of OH ⁻ :Fe ²⁺ ratio on the Fe ₃ O ₄ nanoparticle size	106
6.7 Comparison with directly coprecipitation strategy.....	108

Content

6.8 Conclusions.....	108
7 Conclusions	111
References.....	115
Supplementary Materials	129
A: Control logic of high-speed valve.....	129
B: Strategy for stable segmented flow generation	131
B-1 Influence of gas pressure on segmented flow formation under low liquid flowrate.....	132
B-2 Influence of liquid flowrate on segmented flow formation.....	133
B-3 Influence of gas pressure on segmented flow formation under higher liquid flowrate.....	134
B-4 Influence of gas flow rate on segmented flow formation under higher liquid flow rate.....	135
B-5 Repetitive experiments	136
List of Tables	139
List of Figures	141
List of publications	145
Acknowledgements	147

Nomenclature

a	specific surface area, m^2/m^3
C^*	equilibrium concentration of oxygen in water, mol/m^3
C	concentration of oxygen measured by the DO meter, mol/m^3
C_0	concentration of oxygen in water at time 0, mol/m^3
d	diameter, m
f	high-speed valve frequency, s^{-1}
F	flow rate, m^3/s
K	Scherrer constant, equals 0.89
k_{La}	liquid side volumetric mass transfer coefficient, s^{-1}
k_L	liquid side mass transfer coefficient, $\text{m}\cdot\text{s}^{-1}$
L	length, m
N	the rate of gas absorption per unit volume, $\text{mol}/\text{m}^2\cdot\text{s}^{-1}$
p	pressure, kPa
t	time, s
V	volume, m^3
v	velocity, m/s
β	the full width at half maximum of the peak
τ	contact time, s
λ	X-ray wavelength, equals 1.5406, Å
θ	the Bragg diffraction angle

Subscripts

<i>a</i>	static condition
<i>b</i>	bubble in the flask
<i>C</i>	continuous
<i>c</i>	calculated
<i>d</i>	dynamic condition
<i>Fu</i>	fundamental
<i>f</i>	filling
<i>g</i>	gas
<i>I</i>	interruption
<i>i</i>	inner
<i>l</i>	liquid
<i>min</i>	minimum
<i>max</i>	maximum
<i>p</i>	particle
<i>R</i>	reaction
<i>s</i>	segment in the microchannel
<i>sq</i>	squeezing
<i>t</i>	total

1

Introduction

1.1 Microreactor

1.1.1 Development of microreactor

In 1981, to solve the requirement for effective and compact heat removal of very-large-integrated circuits, Tuckerman and Pease [1] introduced the concept of ‘micro heat exchanger’ and designed a compact heat sink, as shown in Fig. 1.1. After that, microchannel began to draw increasing attention of chemical engineers for its excellent heat and mass transfer performance. DuPont developed [2,3] the first ‘minichemical reactor’ (shown in Fig. 1.2) in the world for processing toxic chemicals in 1990s, and continued the research in this area by collaborating with the Massachusetts Institute of Technology. Chemical companies like UOP, BASF, Bayer, Corning, and Shell also added related researches in their plans; the Japanese government listed microreactor as a new chemical technology in the ‘National industrial technology strategy’ in 2000.

In Academia, the International Microreaction Technology Conference (IMRET) has been held for 16 times from 1997. On April 2004, the first ‘International Conference on Microchannels and Minichannels’ defined the critical dimension of the microchannel to be 10 μ m-3mm. During the last several decades, microreactors had been widely studied

1. Introduction

all over the world from different aspects, including shape design and optimization, hydraulics, heat and mass transfer, and application in various of chemical reactions [4,5].

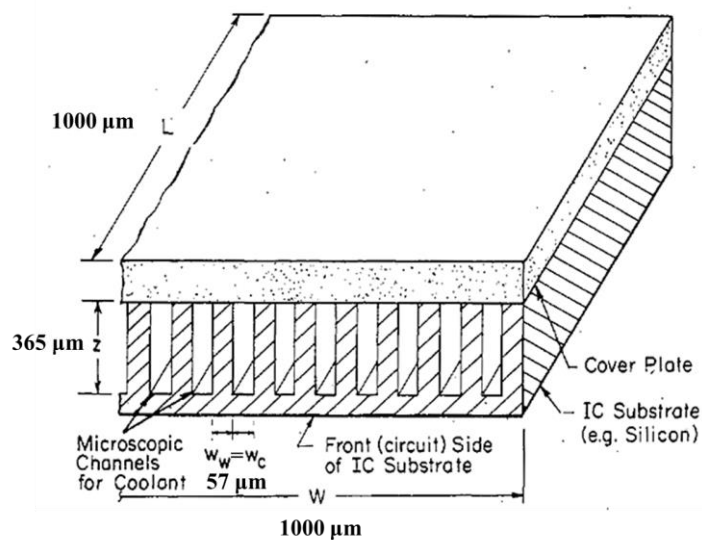


Fig. 1.1 Schematic of the compact heat sink incorporated into an integrated circuit chip [1]

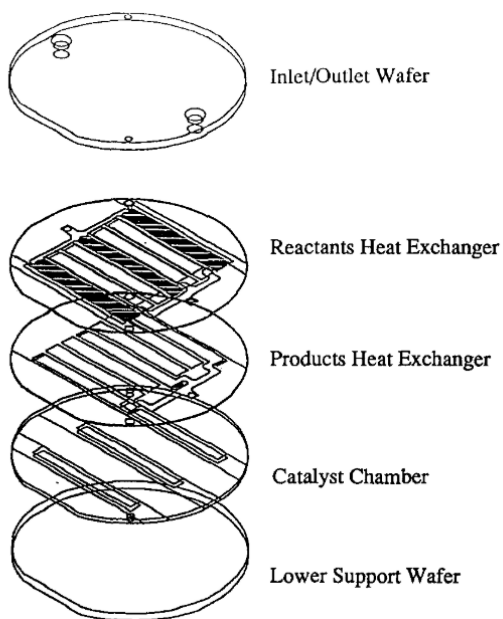


Fig. 1.2 The first microfabricated reactor by DuPont [2]

1. Introduction

In recent years, some leading companies have already provided microreactor products to the market. For example, Corning [6] developed a chip G1 reactor (Fig. 1.3) made of glass (or SiC), which can meet the requirements of caustic or photo reactions, offering a productivity of 80 t/y for single chip; Ehrfeld provides microreactor solutions for both laboratory and production scale, represented by modular microreaction system [7] (Fig. 1.4) and Miprowa, respectively.

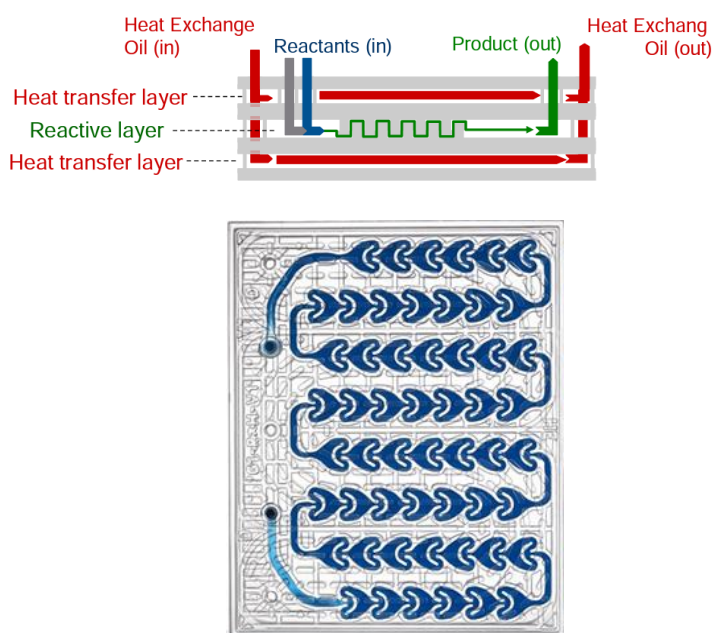


Fig. 1.3 Corning G1 reactor (155×125 mm) [6]

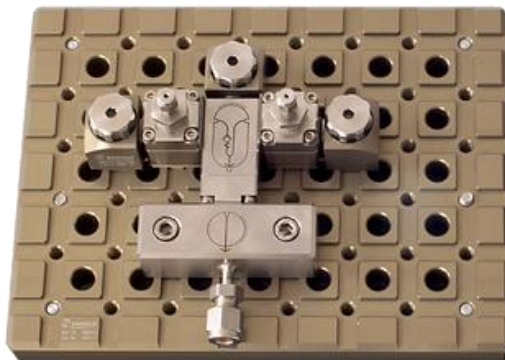


Fig. 1.4 Ehrfeld's modular microreaction system [7]

1. Introduction

1.1.2 Advantages of microreactor

The primary advantage of microreactor lies in the extremely large surface-to-volume ratio, which can reach as high as $100,000 \text{ m}^2/\text{m}^3$ [8]. Due to this feature, the heat and mass transfer can be improved significantly in the microchannel, enabling microreactor to be a promising way for process intensification. It is well known that the mass and heat transfer rates achieved using traditional reactors are restricted, resulting in relatively low reaction efficiencies [9]. However, owing to the scaling effects of microchannels, mass and heat transfer processes in microreactors can be significantly enhanced, thus enabling improvements in reaction efficiency [10–12]. Consequently, microreactors are considered suitable for overcoming the transport limitations of reactions with a large heat of reaction and those requiring fast mixing.

For example, compared to conventional reactors, microreactors have significantly improved the efficiency of reforming reactions, allowing for CH_4 conversion to nearly reach equilibrium at $500\text{--}800 \text{ }^\circ\text{C}$ [13,14]. Wang et al. [15] developed a microreactor for methanol steam reforming, which achieved a maximum energy efficiency of 67.85% and a maximum methanol conversion of 98.7%. The streamlined feature and precise control of microreactors allow continuous or even selective synthesis of various materials such as quantum dots, star polymers, nanoparticles, and catalysts [16–21], and also continuous crystallization with controllable crystal size and shape [22]. Furthermore, microreactors have been successfully used by biochemists to separate products and obtain the highest reported yield for a specific product [10,23,24].

Compared to conventional reactors, the reaction time can be reduced to seconds order in microreactors for the same reaction, and this makes it possible to carry out some batch reactions continuously in a microreactor.

Table 1.1 shows a comparison of the parameters of a low temperature organolithium reaction using conventional batch reactor and Bayer's microreactor [25]. It can be seen clearly that even the volume of the microreactor is 133 times smaller than batch reactor,

1. Introduction

the productivity becomes 1.8 times larger. That is to say, for the same footprint, the production capacity of microreactor is more than 200 times higher than batch reactor. Moreover, the enhanced mass transfer improves the selectivity of the product. To prevent the decomposition of the intermediate product, the reaction is conducted at -70 °C in batch operation; after using microreactor, the reaction residence time is reduced to 3-4 min, which makes it possible to operate the reaction near the decomposition temperature (-40 °C) of the intermediate product, and reduces the energy consumption and operation complexity effectively. Meanwhile, the small volume of the microreactor lowered the material holdup, thus reduces the risk level of the process.

Table 1.1 Parameters of organolithium reaction in batch and micro-reactor [25]

Parameter	Batch reactor	Microreactor
Volume (L)	400	3
Productivity (kg/h)	0.83	1.5
Residence time (min)	--	3-4
Selectivity (%)	89	94
Temperature (°C)	-70	-40
Operation complexity	Complex	Easy
Risk level	High	Low

Therefore, microreactor is regarded as an alternative technology of traditional batch reactor to address the bottleneck problems such as large energy consumption, high wastages, low safety, and extensive reaction control. Furthermore, the dimension of a microreactor allows compact design of the whole process, and decreases the labor requirement and cost of the operation.

In recent years, microfluidic technology has attracted increasing attention in many fields, owing to its precise control and high efficiency in various processes. The enhanced

1. Introduction

mass transfer in the microchannel makes it possible to carry out some synthetic processes continuously and improve the productivities of many products that are inefficient in complex batch operations [26–33].

1.1.3 Flow types in microreactor

A better understanding of the flow behaviors in the microchannel is the fundamental of applying microreactor. Essentially, the flow behaviors are mainly determined by the fluid properties. Based on the phases (liquid, gas, solid) of the fluids, the flow in microchannel exhibits different types. Owing to the tiny flow pass, it is difficult to involve solid particles in the microchannel, because it is easy to clog the channel. Thus, the discussion about flow type in microchannel commonly focus on gas and liquid phases. Consequently, the flow in the microchannel can be distinguished as homogeneous and heterogeneous flow according to the intermiscibility of the fluids.

1.1.3.1 Homogeneous flow

When two (or more) miscible liquids or gases encounter in a microchannel, they will mix with each other, the microchannel works more like a mixer. At the macroscale, the mixing process in traditional vessels rely on natural convection and diffusion to promote mixing over time. Due to reduced dimensions of microchannel, diffusion becomes a slower process, and the flow becomes more laminar (known as the ‘laminar flow regime’). As a result, the mixing is slower and less efficient in microchannels compared to macroscopic vessels. Therefore, homogenous flow might not be the primary focus in microchannel.

1. Introduction

1.1.3.2 Heterogeneous flow

Heterogeneous flow occurs in microchannels when two or more immiscible fluid encountered in the microchannel, this typically involves the presence of at least one liquid phase, and another liquid or gas phase. The flow patterns of immiscible fluids in multiphase microchannels, which include segmented flow, parallel flow, and droplet flow, are significantly influenced by the inertia and viscous forces of the fluid. The flow rate also affects the flow pattern, and the mass transfer behavior is closely associated with the flow pattern [24,34–36]. Among flow patterns, segmented flow has drawn the most attention because strong internal circulation in each segment results in a high interfacial mass transfer rate [37,38]. The most commonly observed manifestations of heterogeneous flow in microchannels are liquid-liquid flow, which involves the interaction of immiscible liquid phases, and gas-liquid flow, where a gaseous phase coexists with a liquid phase.

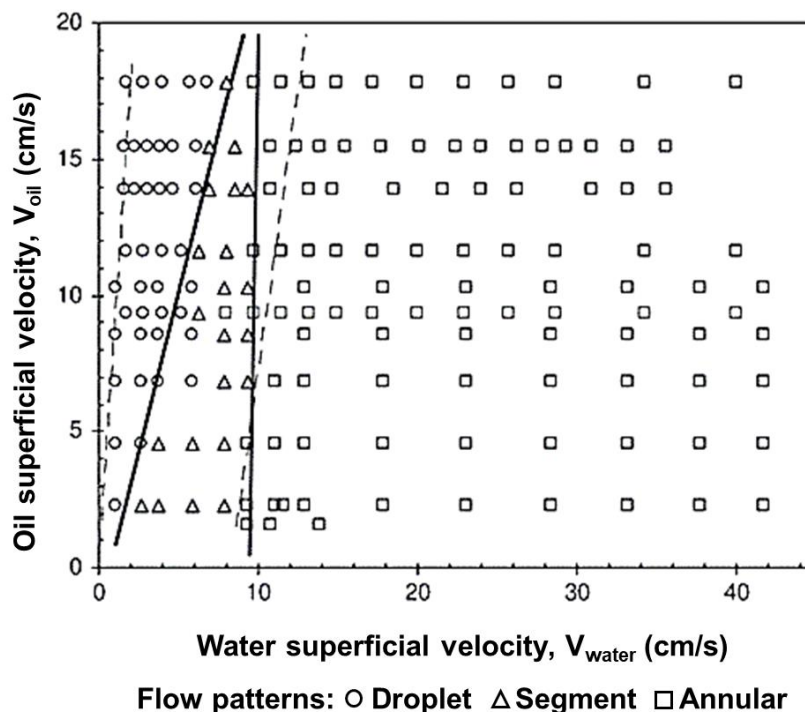


Fig. 1.5. Flow pattern transitions in microchannels initially saturated with oil as a function of oil and water velocities [39]

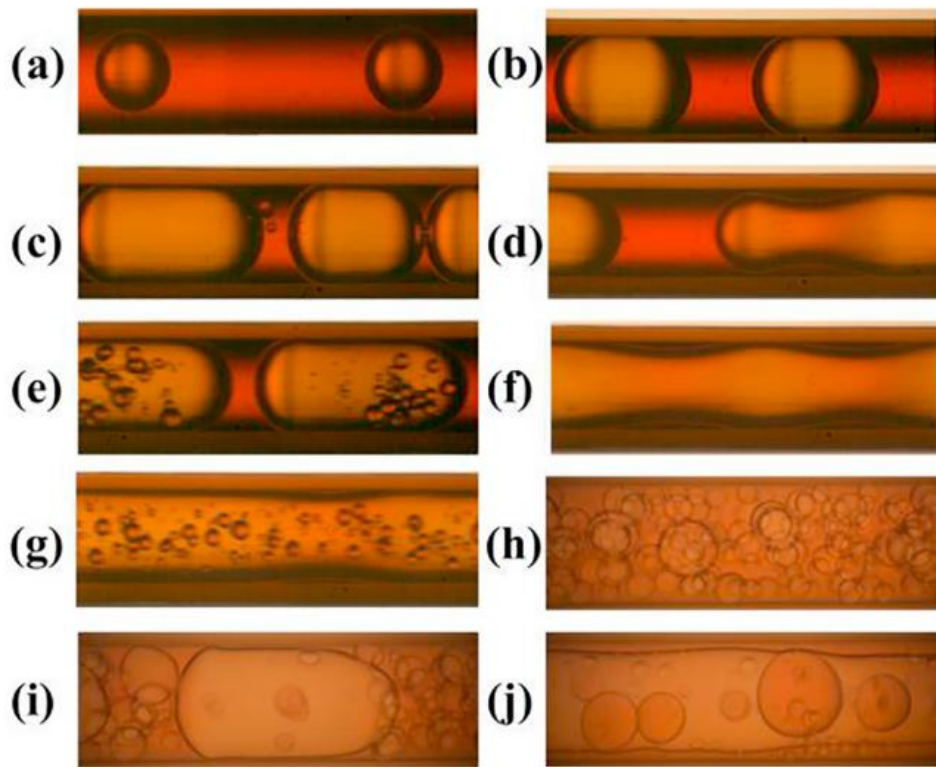


Fig. 1.6. Typical flow patterns observed in the microchannel with 1.2 mm inner diameter and at 0.5 °C [41]

(a)-(g) for toluene-water system and (h)-(j) for ethyl acetate-water system. (a) droplet flow; (b) segmented flow; (c) irregular segmented flow, (d) segment-annular flow, (e) slug-dispersed flow, (f) annular flow, (g) annular-dispersed flow, (h) droplet-dispersed flow, (i) segment-dispersed flow, (j) annular-dispersed.

The most reported liquid-liquid flow patterns in microchannels are segmented flow (Taylor flow, or segmented flow), annular flow, and droplet flow, as shown in Fig. 1.5 [39,40]. When the flow rates of the two phases are altered, the flow pattern undergoes a transformation once the velocity surpasses a threshold. Beside the typical flow patterns, with smaller interfacial tension and property difference between the two phases, there will be some more complex flow patterns as a result of the changing of inertia and viscous force, as shown in Fig. 1.6 [41].

1. Introduction

However, complex flow pattern, such as slug-dispersed flow, droplet dispersed flow and annular-dispersed flow are difficult to control in the microchannel, the inner behavior occurs occasionally. In contrast, segmented flow exhibits a consistent distribution of segments throughout the microchannel, simplifying the control of flow characteristics. As a result, segmented flow has been extensively studied and applied across diverse fields.

Moreover, it's possible to introduce a solid phase into segmented flow, resulting in a triphasic flow within the microchannel. Nano- or mesoporous particles can be suspended in the liquid phase, forming a liquid slurry within the microchannel.

This configuration allows segmented flow to facilitate catalytic reactions within the microchannel (Fig. 1.7) [37]. Nevertheless, the presence of a solid phase can lead to potential blockages in the microchannel and may present a challenge when it comes to separating the final product. As a result, a significant portion of research focuses on biphasic segmented flow.

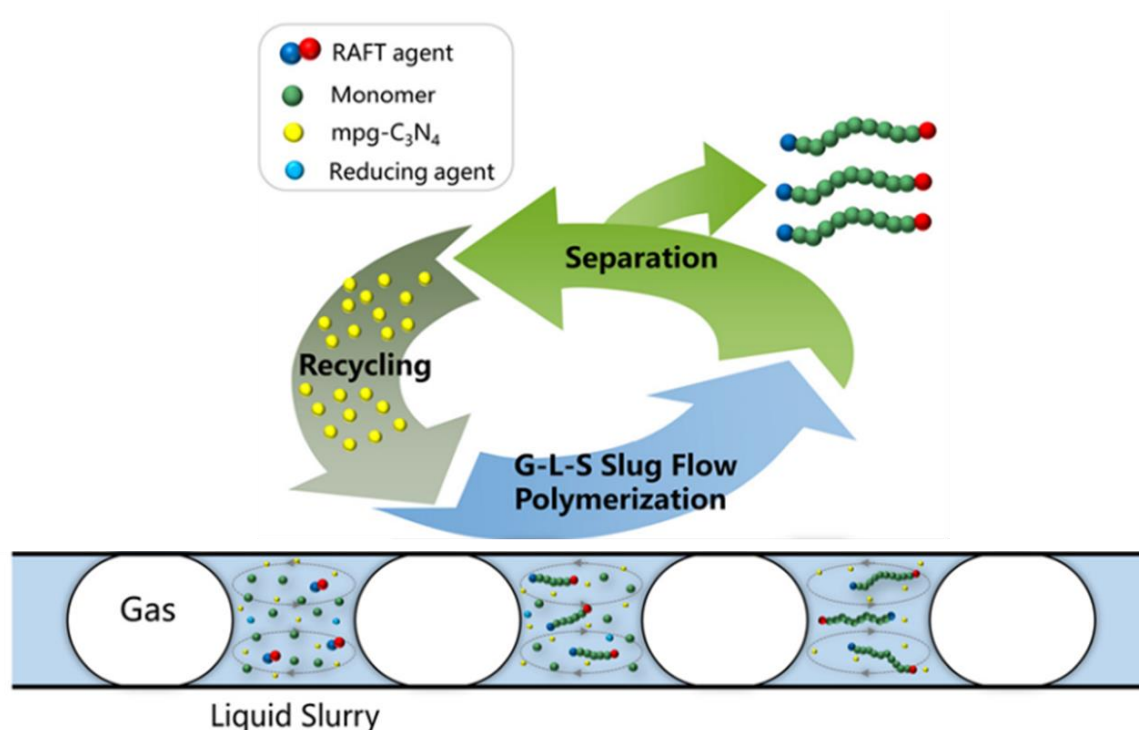


Fig. 1.7. Continuous Gas-Liquid-Solid segmented flow for PET-RAFT polymerization [37]

1. Introduction

1.2 Segmented flow

1.2.1 Formation mechanism

T-junction is usually used to generate segmented flow, it has been widely acknowledged that the formation of segment in T-junction consists two periods—the filling period and the squeezing period [42,43].

Fig. 1.8 [43] shows the formation mechanism of gas-liquid segmented flow at a planar T-junction. During the filling period, the gas phase entered the main channel from the side channel and forms a gas bubble; the bubble keeps growing up, when the bubble fill-up the junction, the fill period ended, and the volume of the bubble is defined as V_{fill} .

In the following squeezing period, the forming bubble is squeezed by the liquid phase and continue to grow up, the squeezing period will finish when the bubble pinches-off, the increment of the bubble volume during this period is defined as $V_{squeeze}$.

In the existing model of segment size estimation, V_{fill} is mainly determined by the volumetric liquid flow rate and the channel shape, while $V_{squeeze}$ is depend on the velocities of both the gas and liquid phases.

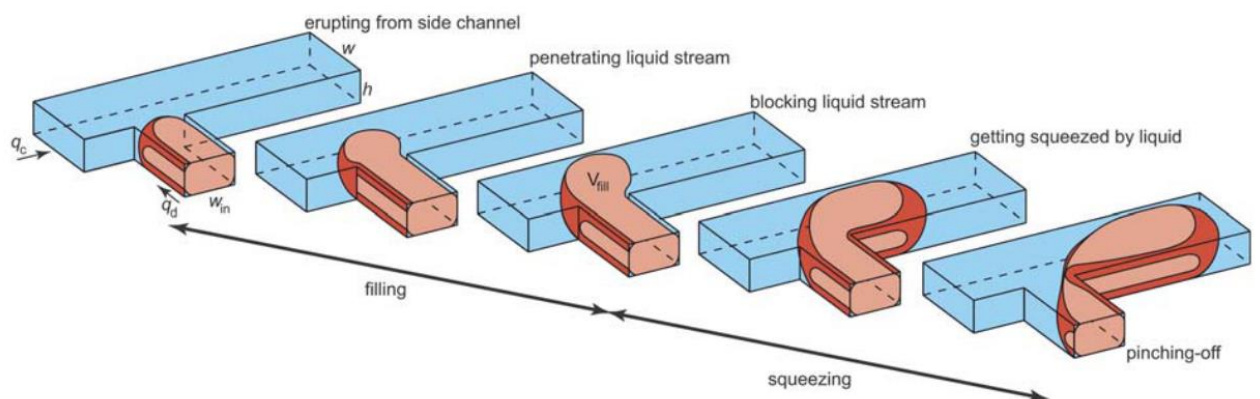


Fig. 1.8. Formation of segment at a planar T-junction [43]

1. Introduction

1.2.2 Characteristics

When a biphasic segmented flow occurs in a microchannel, the liquid phase that exhibits superior wetting properties to the channel wall will act as the continuous phase, while the other phase act as dispersed phase [44]. There is a wall film formed by the continuous phase, and the dispersed phase will flow alongside the film, taking on an elliptical head segment shape. The flow direction of the segmented flow flows the velocity of the continuous phase, and the absolute velocity of the segmented flow is determined by the total flow rates of the two phases and the channel geometric size.

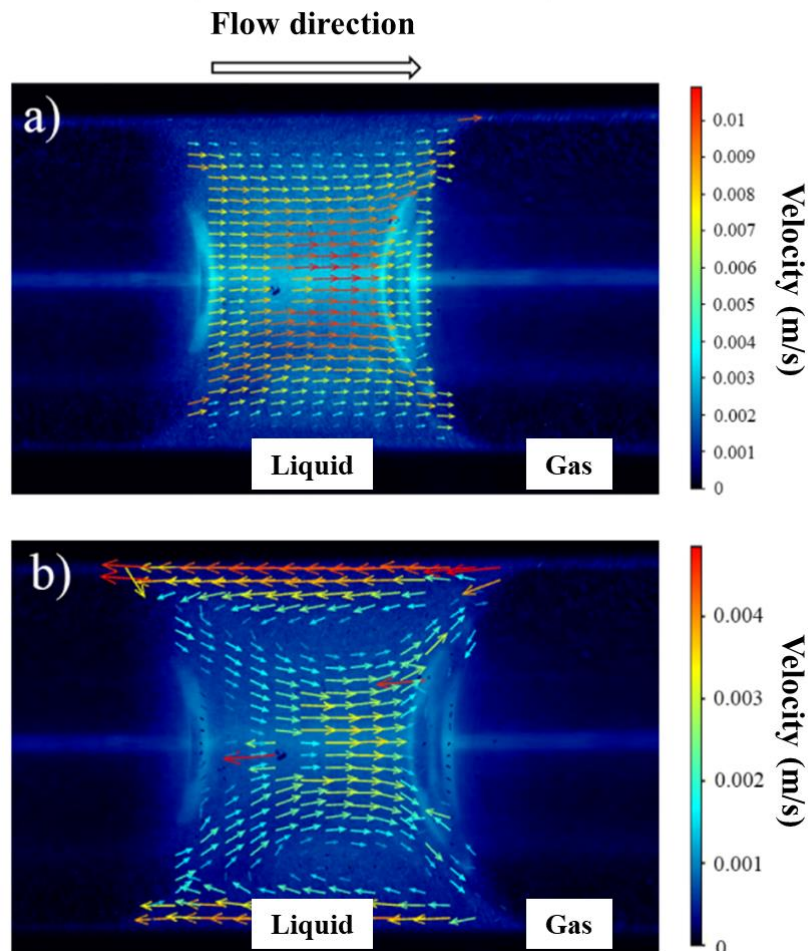


Fig. 1.9. Velocity field of the G–L–S segmented flow in capillary tube [37]

(a) absolute velocity; (b) relative velocity.

1. Introduction

When the segment moves in the microchannel, the shear force between the tube wall and the segment axis arises internal circulation simultaneously with in each segment [37,44,45]. The internal circulation serves to diminish the thickness of the boundary layer at the phase interface, consequently augmenting the diffusive penetration. The absolute value of swirling strength accurately reflects the level of internal circulation intensity, and these two factors share a positive correlation. Fig. 1.9 [37] depicts the velocity distribution within the segmented flow in a capillary tube. It reveals that while there is pronounced recirculation within the segment, there exists a stagnant zone characterized by very low liquid velocity.

1.2.3 Mass transfer in segmented flow

The immiscibility of fluids in heterogeneous systems renders mass transfer substantially more difficult than in homogeneous systems. However, the small size of the microchannel enables the generation of a stable bubble or segmented flow, which provides a sufficiently large interface area to improve the mass transfer performance [41,46].

Based on the flow characteristic of segmented flow, the mass transfer in segmented flow is distinguished as several sub-processes [47]. Fig. 1.10 illustrates the sub-processes in gas-liquid segmented flow, involving mass transfer:

- (a) from gas segment to wall through liquid film
 - from gas segment to liquid film
 - from liquid film to wall
- (b) from gas segment to liquid segment
- (c) from liquid segment to wall

In cases where the wall is coated with a catalyst, all the aforementioned mass transfer processes take place within the segmented flow. However, in the absence of catalyst

1. Introduction

coating, only the first two steps occur. It's worth noting that the majority of research on mass transfer in segmented flow focuses on the latter scenario.

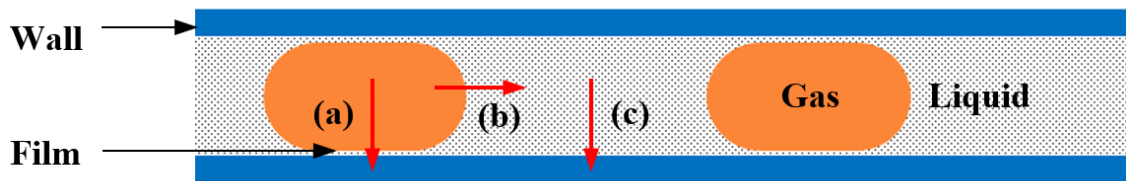


Fig. 1.10. Mass transfer in Gas-Liquid segmented flow

The mass transfer phenomenon in segmented flow have been extensively studied for both physical and chemical adsorption processes on a global scale, examining aspects such as mass transfer coefficients and interfacial area [48–55]. In general, mass transfer coefficient is primarily influenced by the physical properties of the fluids involved, including properties like viscosity, density, diffusivity, and solubility.

Indeed, the internal circulation within the segment plays a crucial role in enabling rapid renewal of material near the interface. This dynamic leads to a significantly enhanced mass transfer coefficient in segmented flow, often ranging from one to two orders of magnitude larger compared to conventional processes. Most researchers believe that the volumetric mass transfer coefficient increases with the segment velocity owing to the enhanced internal circulation flow rate in each segment [56–59]. Reportedly, an increased fluid velocity also shortens the segment length [4,52,60,61].

Furthermore, segmented flow systems present a substantial increase in interfacial area between the phases, the interfacial area between the segments exhibits linear growth against the fluid velocity [57]. This extended interfacial area is a pivotal factor in augmenting the efficiency of mass transfer.

1. Introduction

1.2.4 Application of segmented flow

The enhanced mass transfer in segmented flow makes it capable to serve as a way of process intensification. Because of this feature, segmented flow has not only been applied to perform chemical reactions but also for extraction and crystallization [10,62–70]. The strong recirculation motion of fluids in segmented flow enables each segment to behave as a separate microreactor [4,56,57].

Segmented flow has demonstrated its capabilities in continuously synthesizing Au or Ag nanoparticles [71–73]. Segmented flow provides a simple way to produce Au nanoparticle at room temperature, and the narrow residence time distribution enables the formation of more monodisperse Au nanoparticles. Moreover, it allows for control over the nanoparticle size by adjusting the residence time (or flow rate) of the reactant within the microchannel.

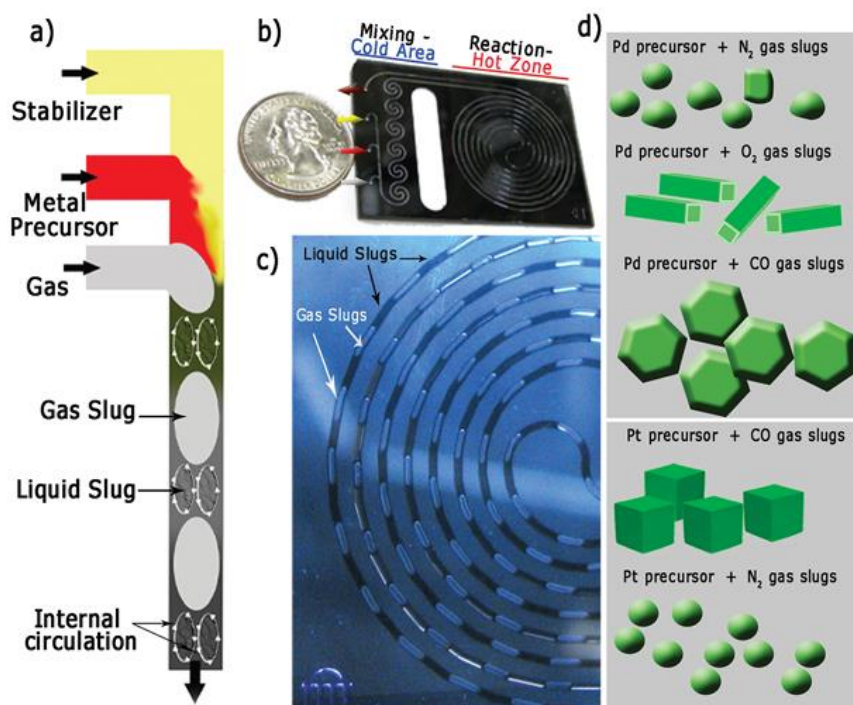


Fig. 1.11. Gas-liquid segmented flow for synthesizing shape-controlled Pt nanocrystals [74]

1. Introduction

Furthermore, the enhanced heat and mass transfer in gas-liquid segmented flow also enable fine control of nanoparticle shape and size (Fig. 1.11) [74]. By changing the gas phase in the segmented flow, faceted nanocrystals with different morphologies were synthesized. When the gas phase is nitrogen, the obtained Pd nanoparticles are formless. After substituting the gas to oxygen, the exposure of metal precursor to oxygen facilitates the anisotropic growth of Pd nanorod, and the aspect ratio can be adjusted by controlling the oxygen to liquid ratio. While CO gas can promote the formation of Pd nanosheet. As the case of Pt nanoparticle, the application of CO and N₂ result in cubic and spherical nanoparticles, respectively.

The large specific interfacial area and the intensified mass transfer through also makes liquid-liquid segmented flow a promising way for extraction. The extraction in segmented flow is considerably faster than that in batch reactors, the time necessary to reach equilibrium reduced from 1 h to 90 s in a reactive extraction case [69]. By introducing gas agitation in liquid-liquid system, the flow rate will increase and forms stable gas-liquid-liquid segmented flow in wider flow rate range. What is more, the shear force produced by the gas injection accelerates the breakup of the liquid, providing larger interface for the extraction process and result in higher efficiency [65].

1.3 Segment length control

Segment length is expected to influence mass transfer, and studies on the formation mechanism of segmented flow in millimeter-scale devices have demonstrated that segment size is determined by the channel geometry and material, liquid-to-gas flow ratio, fluid velocity, and gas pressure stability [10,38,42,75–77]. For a specific microreactor system, the channel size and the material properties are seldom changed. Thus, the control of segment length is always achieved by the other methods.

1.3.1 By changing flow rate

In conventional segmented flow generation system, the fluids are pumped or injected to the junction directly to form the segments in the outlet channel. In order to change the segment length in the same channel, the most employed way is to change the flow rate of the fluids.

As shown in Fig. 1.12 [38], when the flow rate increase, the average segment length become shorter. This result can be explained by the formation mechanism discussed in section 1.2.1. With the increase of the flow rate, the squeeze time during the segment formation becomes shorter, resulting in a reduced $V_{squeeze}$. Therefore, the segment length will decrease consequently.

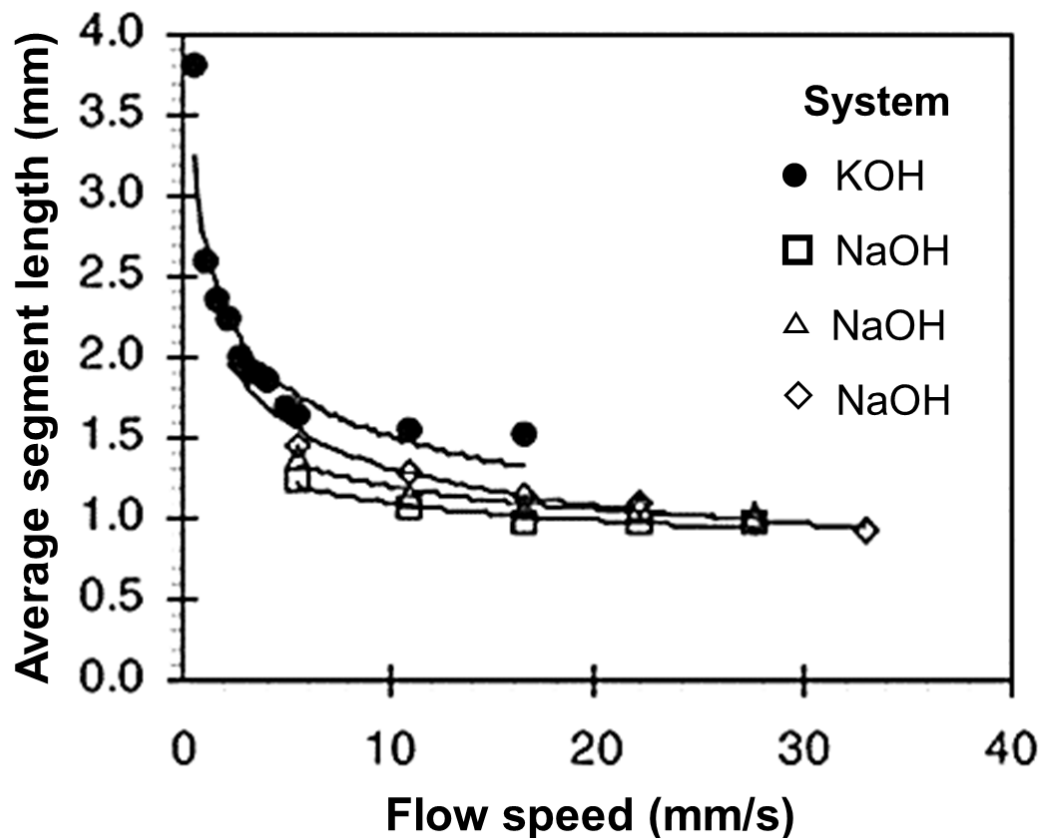


Fig. 1.12. Average segmented length at different flow rate [38]

1. Introduction

Table 1.2 Typical correlations for predicting segment length

Correlation	Parameters	Reference
$L/w = 1 + \alpha Q_{in}/Q_{out}$	Q -- Flow rates w -- channel width	[77]
$L = (Q_G + Q_L) t_G/A$ $L = (Q_G + Q_L) t_L/A$	Q -- Flow rates t -- flow period A -- tube cross section area	[78]
$L/w = -0.78 + 3.55 Ca_c^{-0.04} q^{0.34} (Ca_c < 0.0058)$ $L/w = -1 + 1.65 Ca_c^{-0.18} q^{0.31} (0.0058 < Ca_c < 0.012)$	Q -- Flow rates w -- channel width Ca -- capillary number	[34]

Furthermore, most of the proposed correlations for predicting the segment length in different research are functions of the flow rates [34,77,78], indicating that segment length can only be changed by adjusting the flow rate in a specific microchannel.

1.3.2 By using valve

To change the segment length in the microchannel, several attempts have been made in liquid–liquid systems using valves. Kawakami *et al.* [79] developed a sliding valve with electromagnetic drive, and proposed a new chemical reaction process, namely “micro beaker process”. Controllable slug length was achieved by changing the driving frequency of the sliding valve, and this system can achieve even mixing of the solution and increased reaction efficiency.

Kadowaki *et al.* [80] substituted the valve to a three-port valve (Fig. 1.13) and obtained similar conclusion. Furthermore, the three-port valve was used to generate controllable segmented flow that did not depend on the characteristics and flow rates of the liquids, and developed separation and extraction process successfully [81–83]. The three-port valve system realized high efficiency in water/oil separation process, the separation rate reached 95.3% and 97.3 for the two phases, respectively.

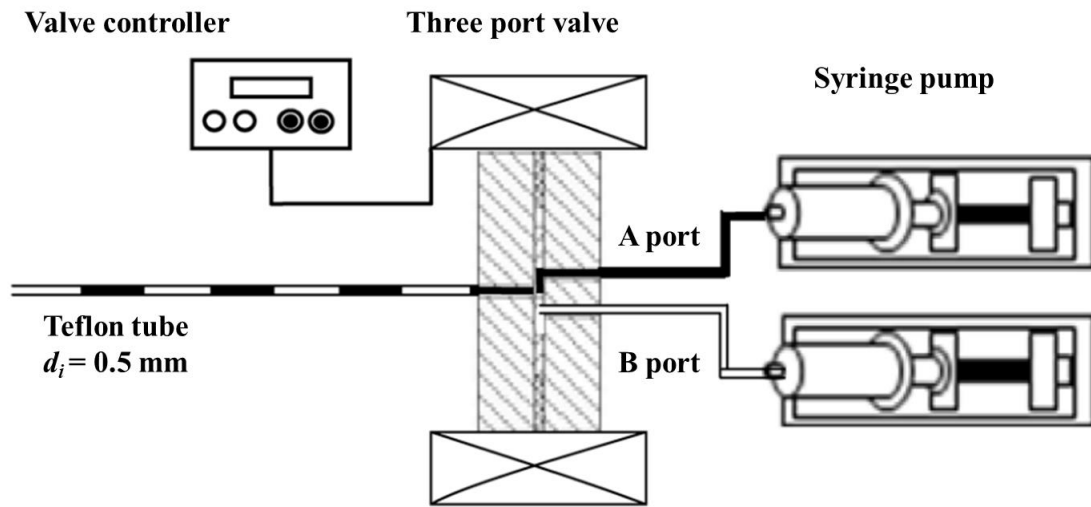


Fig. 1.13. The application of three-port valve for segmented flow generation [80]

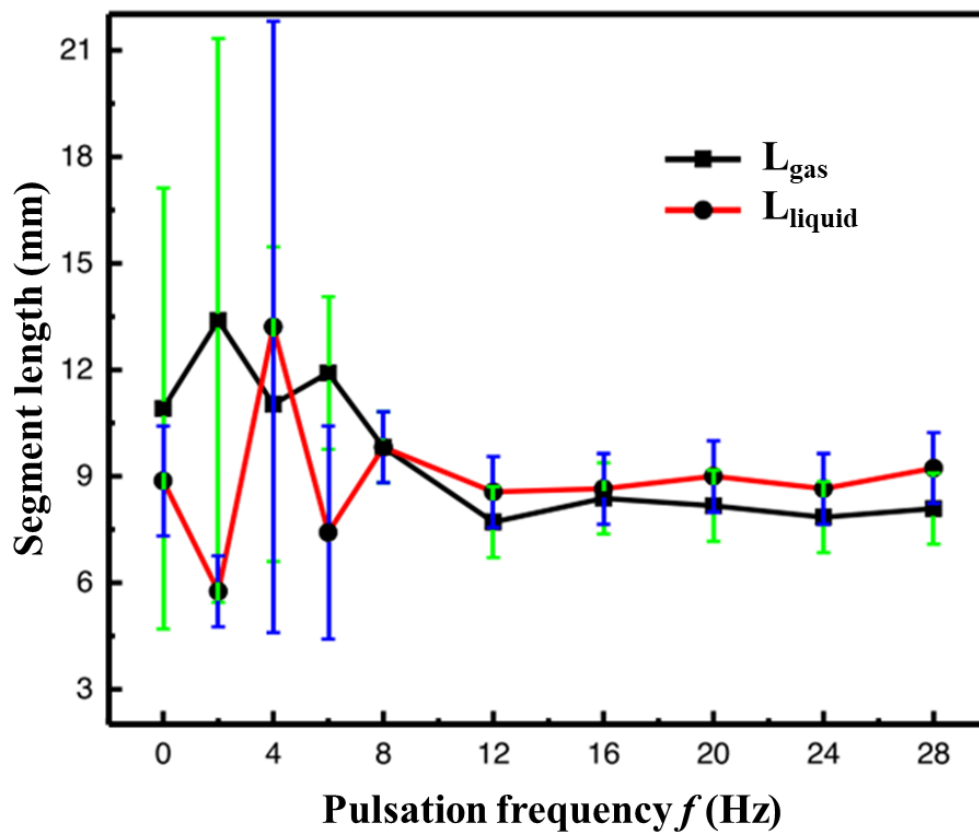


Fig. 1.14. Bubble and liquid segment lengths with different pulsating frequencies [84]

1. Introduction

Compared to liquid–liquid systems, segment length control in gas–liquid systems is more difficult owing to the compressibility of the gas. Few studies have investigated the use of valves to control the segment length in gas–liquid microsystems. Zhang *et al.* [84] attempted to regulate the gas–liquid slug length using a solenoid valve in a microchannel. Although the pulsating gas intake successfully changed the slug length, large deviations in the slug length occurred at low pulsating frequencies, as shown in Fig. 1.14. Thus, it is difficult to confirm that the slug length was precisely controlled, which adds to the growing evidence that gas–liquid segment length control is significantly challenging.

1.3.3 By other methods

Alternative techniques have also been developed to manipulate the multiphase segment length in a series of creative works by researchers from Technical University Dortmund. By employing an adjustable coaxial mixer geometry (Fig. 1.15) [60], the alteration of the mixing point geometry enables controlled generation of liquid–liquid segmented flow, consequently allowing for the adjustment of segment length in a continuous manner.

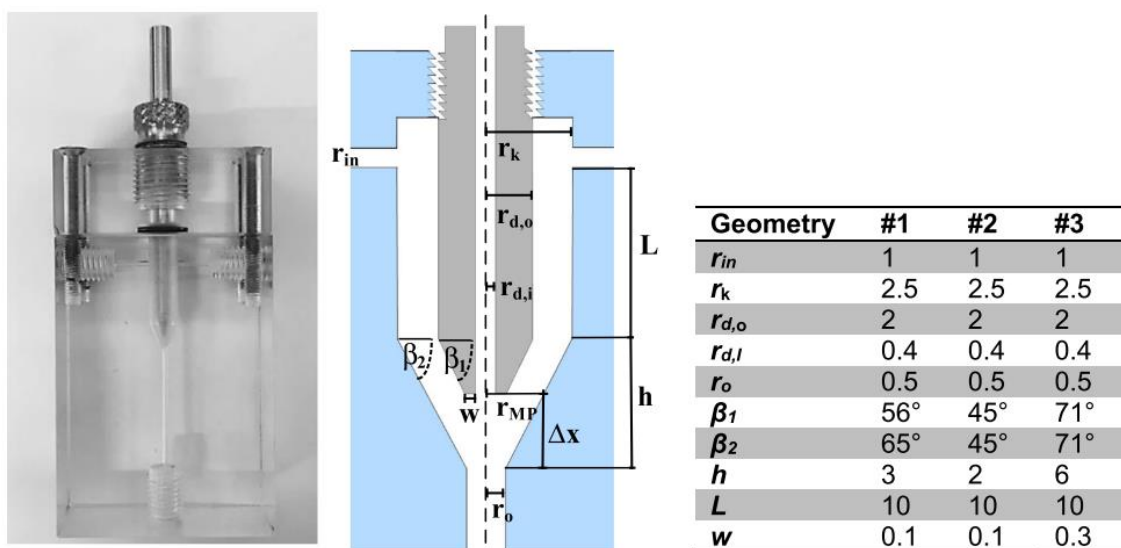


Fig. 1.15. Image and schematic of the generator and geometric parameters [60]

1. Introduction

In their another work [44], a solenoid valve was used to conduct immediate gas supply to liquid-liquid segmented flow, by managing the power source, it becomes possible to regulate the volume of feeding gas, effectively addressing any inaccuracies resulting from fluctuations in valve frequency. Consistent control of the gas feeding volume guarantees the production of uniform gas segments in terms of length.

1.3.4 Research gaps

Modulating fluid flow rates allows for precise control of segment length in both liquid-liquid and gas-liquid systems. When flow rates remain constant, it is possible to adjust segment length in liquid-liquid segmented flow. However, due to the compressibility of gas, achieving consistent control of gas-liquid segment length proves to be challenging. Present approaches do not effectively achieve this control without altering fluid flow rates, and the associated mass transfer phenomena in such systems have not been extensively studied. To tackle this challenge, it is imperative to dedicate focused efforts towards devising a novel strategy for generating gas-liquid segments without the need to alter fluid flow rates.

1.4 Fe₃O₄ nanoparticle

1.4.1 Background

Fe₃O₄ nanoparticles have been of great interest to scientists and engineers for several decades because of their unique magnetic properties. As a versatile and important material, they have been studied extensively for application in batteries, catalytic reactions, biomedicine, magnetic separation, and environmental remediation [85–94]. In particular, Fe₃O₄ nanoparticles exhibit superparamagnetic properties at particle sizes of < 30 nm but

1. Introduction

are ferrimagnetic at sizes ≥ 30 nm at room temperature [95]. Superparamagnetic Fe_3O_4 nanoparticles have proved to be suitable for biomedical imaging and labeling, inducing heating treatments and drug delivery systems.

1.4.2 Conventional synthesis methods

Traditional Fe_3O_4 nanoparticle synthesis technologies mainly use batch operation methods, among which chemical coprecipitation is mostly employed for sample procedures; however, this process is limited by its long operation time (≥ 2 h) [91,95,96].

The coprecipitation reaction for Fe_3O_4 nanoparticle formation is described by Eq. (1.1), and the nanoparticle size is determined by the combined effects of the nucleation and growth phases [97,98]. Nucleation occurs instantaneously to form nuclei, and crystals grow when the solute diffuses from the solution to their surface. Only when the mixing is sufficiently strong are the nuclei able to form simultaneously to consume most of the reactant and prevent crystal growth.

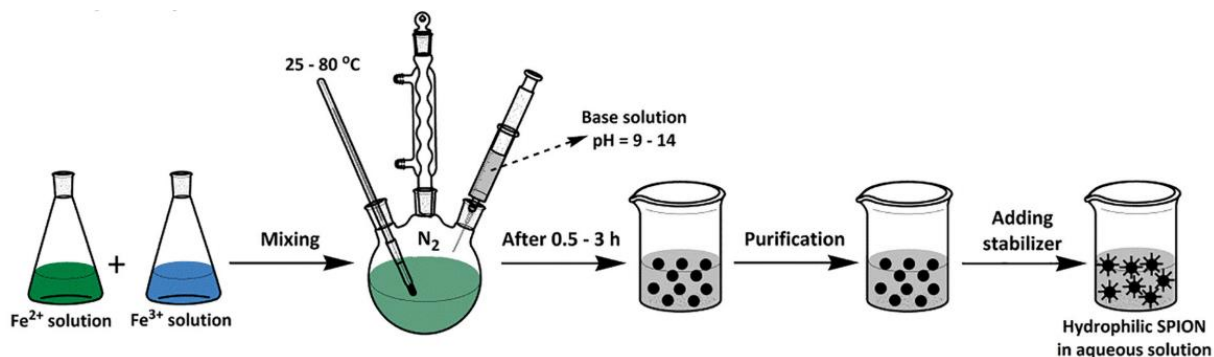
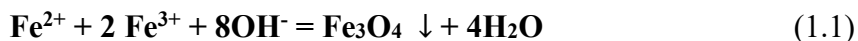


Fig. 1.16. Conventional batch process for Fe_3O_4 nanoparticle synthesis [99]

1. Introduction

However, in the conventional batch strategy, the coprecipitation reaction is implemented by dropping the base solution into a large amount of solution containing Fe^{2+} and Fe^{3+} ions, as shown in Fig. 1.16 [99], whereby insufficient mixing of a large volume of solution results in a wide size distribution of the Fe_3O_4 nanoparticles [96,100]. Meanwhile, to provide an oxygen-free atmosphere for the oxidation of Fe^{2+} to Fe^{3+} , a nitrogen gas flow must be supplied to the batch reactor during the coprecipitation process. Thus, a method to enhance the mixing efficiency of the process to improve product quality is urgently required.

1.4.3 Continuous synthesis methods

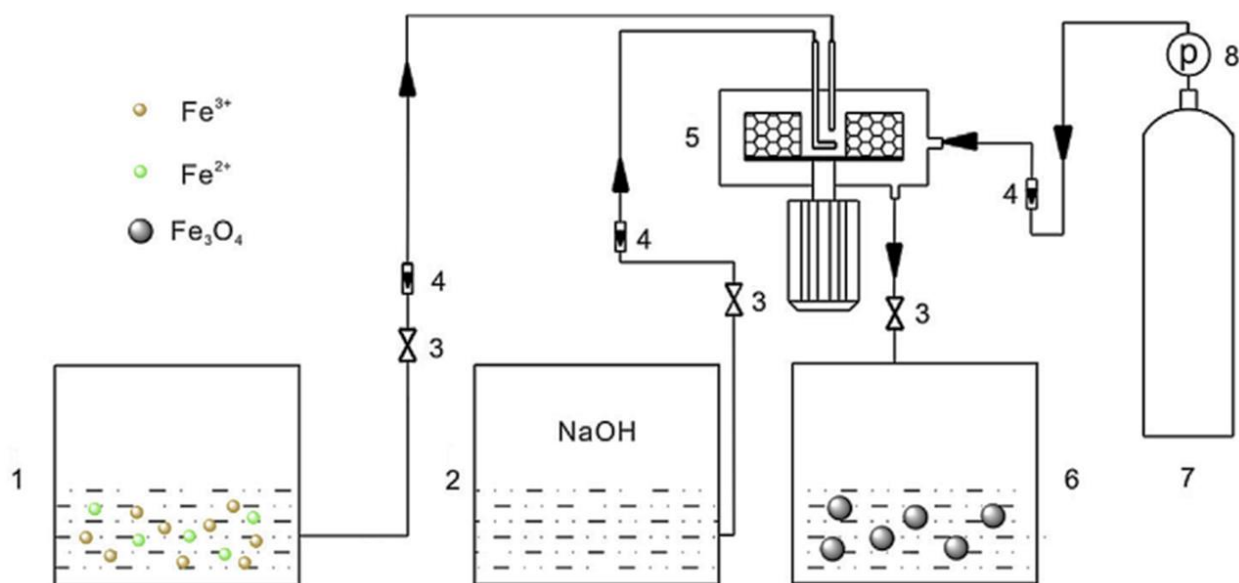


Fig. 1.17. Continuous synthesis of Fe_3O_4 nanoparticle in packed-bed reactor [102]

1: stirred tank A; 2: stirred tank B; 3: valve; 4: rotameter;

5: IS-RPB; 6: reservoir; 7: N_2 cylinder; 8: piezometer

In recent years, there have been several endeavors to advance the continuous

1. Introduction

synthesis of Fe_3O_4 nanoparticles through a variety of methods. Lin et al. [101] employed a rotating packed bed reactor to synthesize Fe_3O_4 nanoparticles, yielding particle sizes of approximately 7 nm at 60 °C. Fan et al. [102–104] used a comparable device with a shell diameter of 200 mm (Fig. 1.17) and obtained nanoparticles of 10 nm at 80 °C.

Despite achieving relatively small particles, these methods have their shortcomings. For instance, the devices used are inherently complex, considering their limited throughput (approximately 20 mL/min). Moreover, these devices occupy a significant amount of space and require substantial investment for operation and maintenance, inevitably inflating production costs.

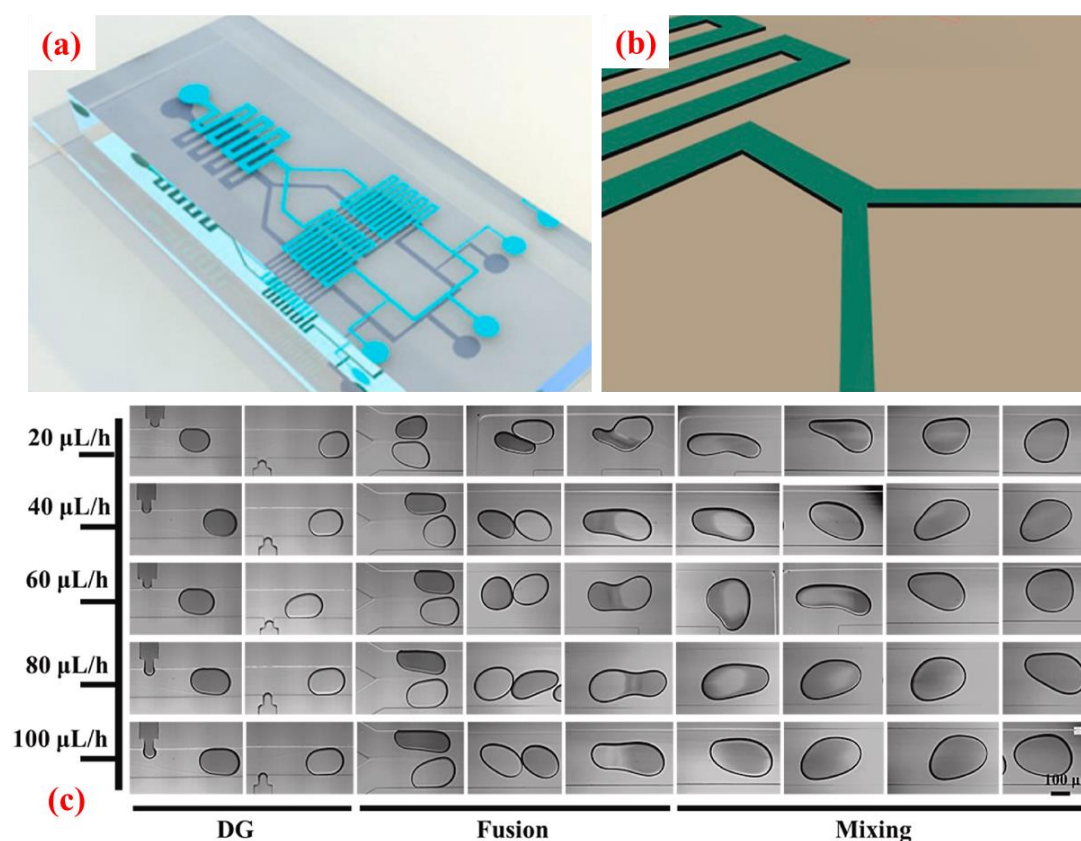


Fig. 1.18. Continuous synthesis of Fe_3O_4 nanoparticle in microfluidic chip [105]

- (a): microfluidic chip; (b): Y-junction for droplet generation
(c): droplet fusion at different flow rates

1. Introduction

In recent times, microfluidic technology has attracted increasing attention across various fields due to its precise control and high operational efficiency. Enhanced mass transfer within the microchannel enables the continuous execution of certain synthetic processes, thus ameliorating the productivity of products traditionally inefficient in complex batch operations [26–33].

Zou et al. [105] produced a microfluidic chip (Fig. 1.18) for synthesizing Fe₃O₄ nanoparticles in droplet flow, manipulating the flow rate ratio and reaction temperature. The resultant Fe₃O₄ nanoparticles ranged in size from 17±5 to 29±4 nm. However, their method demonstrated relatively low productivity due to the maximum flow rate of only 0.5 mL/h.

1.4.4 Research gaps

Among the continuous synthesis methods of Fe₃O₄ nanoparticles, the success of the rotating packed bed reactor may derive from the intensive mixing of reactants at a packing surface facilitated by liquid film formation driven by centrifugal acceleration. Conversely, the advantage of the microfluidic chip lies in the microscale size of the droplet. Reactions in microfluidic systems occur at the nanoliter volume scale of the droplet, allowing rapid and efficient reagent mixing.

However, the complexity of the rotating packed bed reactor and the low capacity of the microfluidic chip hinder their application for Fe₃O₄ nanoparticles fabrication. Therefore, a simple, convenient, and high throughput device is urgently required for synthesizing size-controlled Fe₃O₄ nanoparticles.

1.5 Research plan

1.5.1 Objectives

In order to fill the aforementioned research gaps, the objectives of this study are to:

1. Achieve regularly control of the gas–liquid segment length without changing the residence time of fluids, followed by an evaluation of the associated mass transfer processes.
2. Leverage the benefits of segmented flow for continuous synthesis of Fe₃O₄ nanoparticles in a gas-liquid segmented flow, and achieve nanoparticle size regulation by altering segment length using a high-speed valve without changing the residence time of fluids.

1.5.2 Strategies and outlines of the thesis

In pursuit of these objectives, the thesis outlines the following strategies:

Chapter 2: This chapter thoroughly outlines the methodology employed, encompassing the selection of instruments and chemicals, establishment of fundamental correlations, design of the segmented flow generation system, as well as the approach for measuring segment length and nanoparticle size.

Chapter 3: A pneumatically actuated high-speed valve is introduced into the segmented flow generation system. By installing the high-speed valve at the gas inlet tube and regulating its action frequency, the gas injection frequency can be varied, consequently adjust the segment length without changing the residence time of the fluids. Additionally, the influence of the fluid flow rate on the segment length is investigated. Finally, a correlation is proposed to predict the segment length based on relevant parameters.

Chapter 4: In this chapter, a set of experiments is carried out to uncover the impact

1. Introduction

of segment length on mass transfer performance. Through adjustments to the apparatus, the instinct mass transfer rate within the segmented flow is determined. Subsequently, correlations were proposed based on the experiment results to predict both the specific area and volumetric mass transfer coefficient within the segmented flow, which reveals that the mass transfer rate in valve-controlled segmented flow can be manipulate by varying the valve frequency.

Chapter 5: Expanding upon the prior findings, this chapter refines the apparatus to enable the continuous synthesis of Fe_3O_4 nanoparticles by coprecipitation of Fe^{2+} and Fe^{3+} ions. Optimization is carried out for parameters including feed concentration, $\text{Fe}^{2+}:\text{Fe}^{3+}$ ratio, and reaction temperature. Additionally, employing a high-speed valve rather than adjusting the flow rate results in achieving a more consistent size for the Fe_3O_4 nanoparticles size as the segment length decreases.

Chapter 6: In this chapter, the gas–liquid segment flow system is further fine-tuned to enable the continuous preparation of Fe_3O_4 nanoparticles by partial oxidation precipitation of Fe^{2+} . This system is divided into an oxidation section and a coprecipitation section. Utilizing X-ray diffraction (XRD) and transmission electron microscopy (TEM), the optimal oxidation time is determined by adjusting the tube length (residence time). The precipitation reaction method is adapted to this continuous strategy bases on parameters derived from batch operation. Subsequently, through the optimization of the addition sequence of the nucleating agent, the choice of acid additive, and the $\text{H}^+:\text{Fe}^{2+}$ and $\text{OH}^+:\text{Fe}^{2+}$ ratios, optimal conditions for synthesizing Fe_3O_4 nanoparticles with a narrow size distribution are confirmed.

Chapter 7: In this chapter, the study reaches its culmination by summarizing the research findings and highlighting their significance. It also underscores the impact of this research and outlines potential avenues for future studies in this field.

Part I

Strategy of Segment Length Control and Mass Transfer Measurement

2

Methodology

2.1 Experimental set-up

2.1.1 Apparatus and instruments

To build up the experimental systems for this study, plenty of apparatus and instruments were employed. The major information of them are listed in Table 2.1 as follow:

Table 2.1 Apparatus and instruments used in this study

Directories	Brand	Model	Description
Raspberry Pi 4	OKdo technology Ltd.	B	4GB RAM
Diaphragm pump	Tacmina	QI-100-VF-P-S	0.01-100 mL/min
Mass flow controller	Fujikin	FCST1005LC-4F2	0.01-10 sccm
High-speed valve	Swagelok	6LVV-ALD3FR4-P-CV	See 2.1.2
Compressor	Ryobi	ACP-50	Max. 0.78 MPa
Microscope	SHIMAZU	STZ-161-TLED	--
Lens	Kowa	LM6JC	6mm/F1.4

2. Methodology

Directories	Brand	Model	Description
Water bath	THOMAS	T-22LA	0-50 °C
DO meter	Iijima	B-506S	0.00-20.0 mg/L
Analytical balance	Sartorius	CP324S	d = 0.1mg
Drying oven	Sansyo	SDN/W-70P	1200 W
T-junction	ISIS	T-410-6005	$d_i = 1.5$ mm
Magnetic stirrer	Asona	CS-4	--

2.1.2 High-speed valve

The high-speed valve employed in this research is a product of *Swagelok* (model: 6LVV-ALD3FR4-P-CV), its full name is Atomic Layer Deposition (ALD) Valve [106]. The body of the ALD valve is made of 316L stainless steel, the temperature capability is up to 200 °C. And the cobalt-based superalloy material improves the strength and corrosion resistance of the valve significantly.

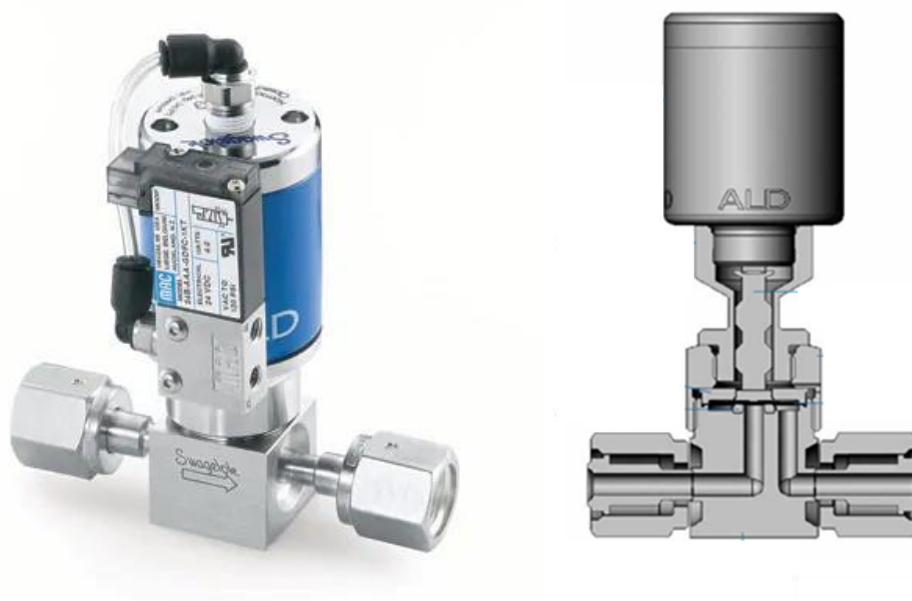


Fig. 2.1 Image and structure of the ALD valve [106]

2. Methodology

The main features of the ALD valve are as follows:

- 1) Capable to open or close the valve within 5 ms
- 2) High-speed and repeatable actuation
- 3) Pneumatic actuator
- 4) Solenoid pilot valve for electronic control of high-speed actuation

These features enable the ALD valve action as much as 100 times per second, providing a wide range of f (operation frequency of the ALD valve) that can be manipulated. The intricate operational logic of the ALD valve is elucidated in supplementary materials A.

To verify the efficacy of the high-speed valve, it was employed at both the liquid and the gas tubes. However, it only produced a uniform segmented flow in the latter case. This phenomenon may be attributed to the relatively high fluids flow rate, larger tube diameter, and the incompressibility of the liquid phase. consequently, for this research, the high-speed valve is specifically installed at the gas tube.

2.1.3 Segmented flow generation system

A schematic of the segmented flow generating system is shown in Fig. 2.2(a). Water and nitrogen intersected in a T-junction (OD [outer diameter]: 1.60 mm, ID [inner diameter]: 1.10 mm, Fig. 2.3) to produce segmented flow in the PFA outlet channel (OD: 3.17 mm, ID: 1.59 mm), as shown in Fig. 2.2(b). The liquid flow rate was controlled using a diaphragm pump (QI-100-VF-P-S, Tacmina), and a mass flow controller (FCST1005LC-4F2-F10, Fujikin) was used to regulate the gas flow rate.

The high-speed valve was positioned at the outlet of the mass flow controller. The valve was driven by compressed air supplied by a compressor and connected to a Raspberry Pi micro single-board computer, which sent signals to open or close the valve. The high-speed valve could be opened (or closed) within 5 ms, allowing the flow to be

2. Methodology

switched at a high rate. After the output channel is full of segments and the segmented flow became stable, images of the segments formed in the tube were captured using a high-speed camera (BU602MCF, Toshiba) and a microscope (STZ-161-TLED-HZ, Shimadzu) installed on the outlet of the segment generation device.

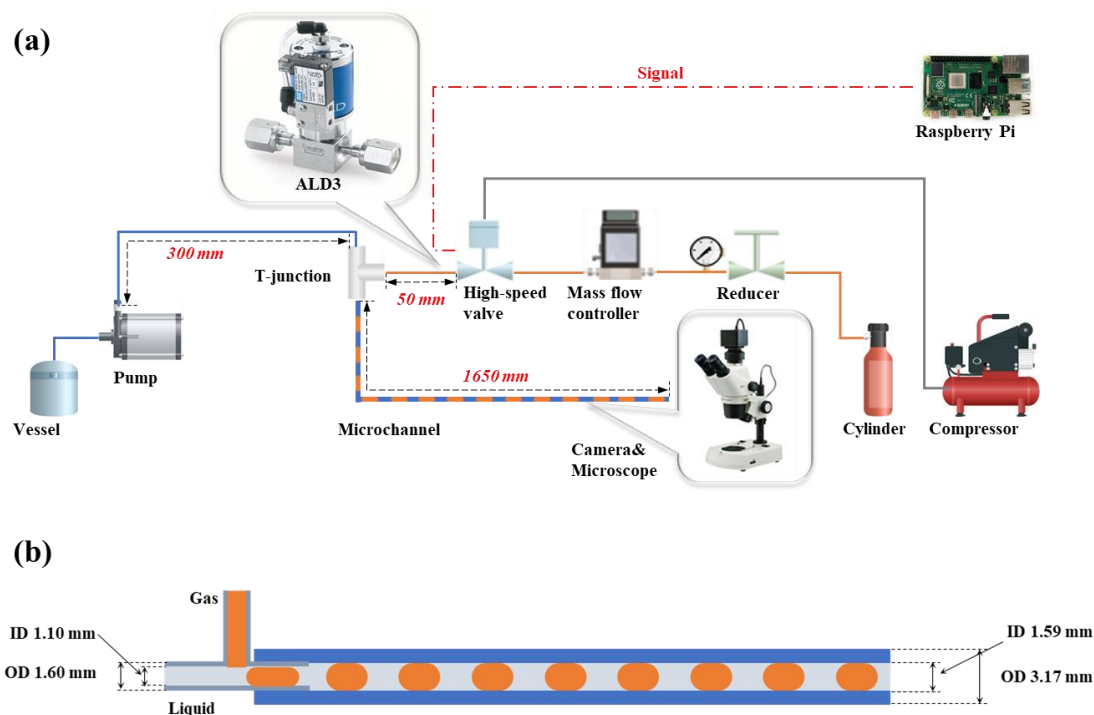


Fig. 2.2 (a) Schematic of segmented flow generating system;

(b) Configuration of T-junction and PFA tube



Fig. 2.3 Image of the T-junction

2. Methodology

2.2 Methods

2.2.1 Chemicals

The chemical agents utilized in this study are outlined in Table 2.2 below:

Table 2.2 Chemicals used in this study

Directories	Formula	Brand	Description
Ferrous chloride tetrahydrate	$\text{FeCl}_2 \cdot 4\text{H}_2\text{O}$	Sigma-Aldrich Co., Ltd	--
Ferric chloride hexahydrate	$\text{FeCl}_3 \cdot 6\text{H}_2\text{O}$	Fujifilm Wako Pure Chemical Co.	99.0 %
Sodium hydroxide	NaOH	Fujifilm Wako Pure Chemical Co.	98.0 %
Ethylene glycol	$(\text{CH}_2\text{OH})_2$	Fujifilm Wako Pure Chemical Co.	99.5 %
Ethanol	$\text{C}_2\text{H}_5\text{OH}$	Fujifilm Wako Pure Chemical Co.	99.5 %
Hydrochloric acid	HCl	Nacalai Tesque	35 wt%
Ammonium chloride	NH_4Cl	Fujifilm Wako Pure Chemical Co.	99.5 wt%

2.2.2 Measurement of segment length

The experimental segment length was determined from segment images using the outer diameter of the microchannel for calibration. Given the large tube diameter, the liquid film between the tube wall and the gas segment is neglected. A dynamic image of the segmented flow with liquid and gas flow rates of 2.0 mL/min and 2.0 mL/min, respectively, at a valve frequency of 7.0 s^{-1} is shown in Fig. 2.4 (a).

However, as shown in Table 2.3, the obtained segment length is unreasonable when compared to the theoretical mass balance calculation, with errors as large as 21.34%. This discrepancy was due to an overestimation of the gas segment volume resulting from taking consideration of the volume of water that filled the space between the non-

2. Methodology

cylindrical head of the gas segment and the tube wall.

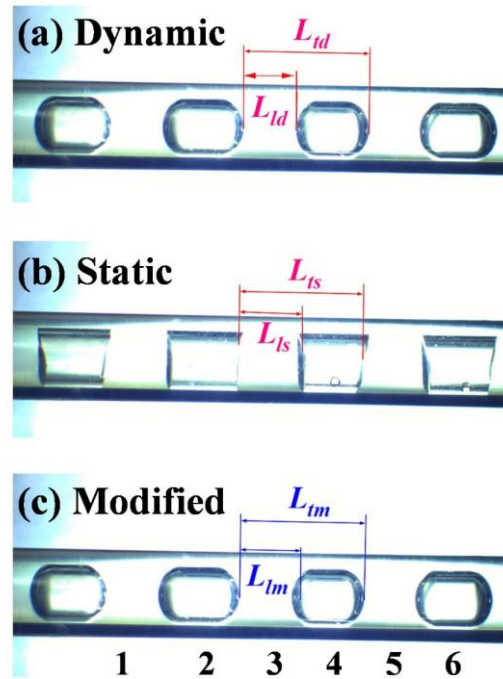


Fig. 2.4 Measurement methods for segmented flow

Table 2.3 Segment lengths obtained using different measurement methods

No.	Theoretically calculated length (mm)	Dynamic image measurement			Static image measurement			Modified dynamic image measurement		
		Length (mm)	G/L ratio ^{*1}	Error	Length (mm)	G/L ratio	Error	Length (mm)	G/L ratio	Error
1	2.39	2.18		-8.79%	2.28		-4.60%	2.26		-5.44%
2	2.39	2.60	1.19	8.79%	2.55	1.11	6.69%	2.54	1.12	6.28%
3	2.39	1.88		-21.34%	2.26		-5.44%	2.25		-5.86%
4	2.39	2.66	1.38	11.30%	2.26	1.00	-5.44%	2.26	1.00	-5.44%
5	2.39	1.89		-20.92%	2.24		6.28%	2.18		-8.79%
6	2.39	2.75	1.46	15.06%	2.43	1.08	1.67%	2.44	1.12	2.09%

Note 1: G/L ratio represents the ratio between gas and liquid segment length.

2. Methodology

To eliminate this error, a static image of the same segmented flow was obtained by disconnecting the microchannel from the T-junction outlet. After the pressure in the microchannel reached equilibrium with atmospheric pressure, the segment length measured in the captured image (Fig. 2.4[b]) was close to the theoretical value, with an error of less than 6.7%.

Because of the difficulties involved in static image measurement during a continuous segmented flow generation process, a modified dynamic image measurement method was developed, as shown in Fig. 2.4 (c). In this modified method, the liquid–gas boundary was expanded to the gas segment, with half of the volume of the gas segment elliptical head on one side considered to be occupied by the liquid. The obtained segment lengths for both phases agreed with those determined using static image measurements.

Therefore, in this study, the segment lengths were measured using the modified dynamic image measurement method, and the final segment lengths represented in the flowing tables and figures are the average data obtained from 10 segments.

2.2.3 Evaluation of mass transfer

The experimental device consists of two parts, namely, a segmented flow generation system and mass transfer measurement system, as shown in Fig. 2.5. The segmented flow generation system mirrors the configuration illustrated in Figure 2.2, with the only alteration being the substitution of the gas phase with air. The mass transfer measurement system has two configurations.

Configuration (a) was used to measure the overall mass transfer in the system. The oxygen concentration measurement was conducted in a three-necked flask; each neck of the flask was filled with a plug to isolate the air. A dissolved oxygen (DO) meter (B-506S, IJJIMA) was inserted into the flask from the left neck through a hole in the plug, and the water in the flask was pumped out (to generate a segmented flow) and recycled (as

2. Methodology

segmented flow) through two tubes from the right plug. Nitrogen gas was blown into the flask through a tube in the middle plug to exhaust the dissolved oxygen in the water before the experiment started; there was another tube in the middle plug as the gas vent.

Furthermore, the flask was settled in water bath to maintain the temperature at 30 °C during the experiment, and a magnetic rotor was settled in the flask to stir the water at high speed to ensure the homogeneity of water in the flask. Using this setup, the measured oxygen concentration in the flask was reflected by the mass transfer between the segmented flow in the microchannel and bubble surface in the flask.

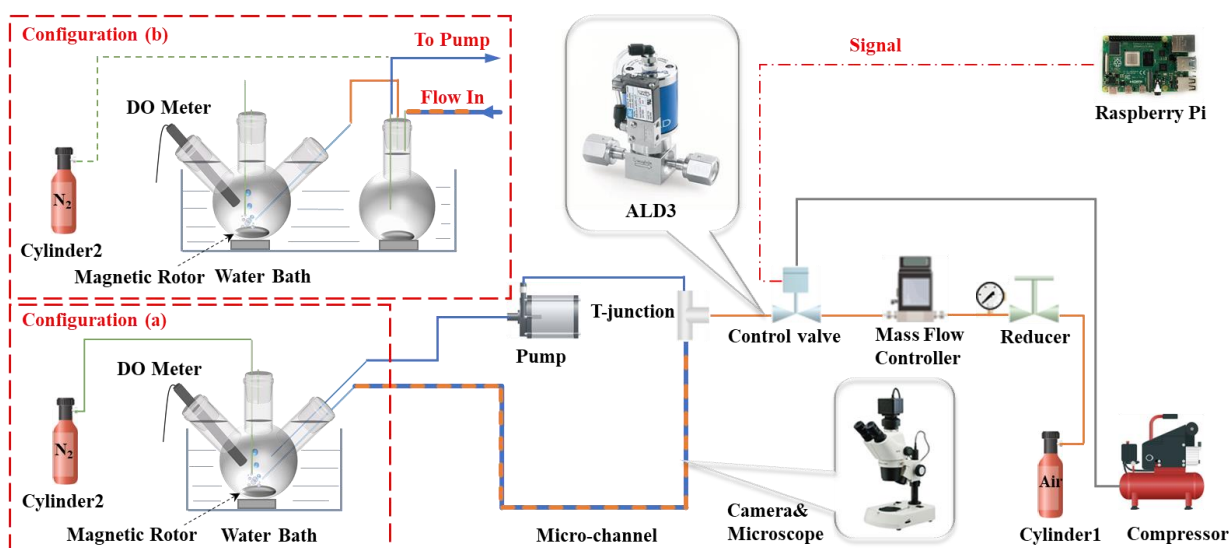


Fig. 2.5 Schematic of experimental setup for mass transfer measurement

In configuration (b), an extra flask was installed in front of the three-necked flask to modify the measurement method. In this further fine-tuned setup, water recycling and segmented flow separation occurred in the first flask, and the separated air from the segmented flow was then injected into the three-necked flask.

The DO meter was placed in the three-necked flask to measure the oxygen concentration in the water. Using the same volume of water (350 mL) and assuming that the air in the upper volume of the first flask had no mass transfer with the water below,

2. Methodology

the mass transfer in the three-necked flask could be considered as contributed by the bubbles only.

2.2.4 Fundamental correlations

(1) Segment length measurement

The segment length in the microchannel was primarily determined by the fluid flow rate and the channel geometry. Based on a mass balance calculation inside the microchannel, the multiphase segment velocity can be expressed as follows:

$$\mathbf{v}_t = \frac{(F_g + F_l)}{(\pi/4) d_i^2} \quad (2.1)$$

where \mathbf{v}_t is the total biphasic velocity (m/s), F_g is the gas flow rate (m³/s), F_l is the liquid flow rate (m³/s), and d_i is the inner diameter of the microchannel (m). Taking into consideration the high-speed valve frequency f , with s⁻¹ units, the theoretical segment length can be obtained using Eq. 2.2–2.4.

$$L_{gc} = \frac{1}{f} \frac{F_g}{(\pi/4) d_i^2} \quad (2.2)$$

$$L_{lc} = \frac{1}{f} \frac{F_l}{(\pi/4) d_i^2} \quad (2.3)$$

$$L_{tc} = \frac{1}{f} \mathbf{v}_t \quad (2.4)$$

where L_{gc} is the calculated gas segment length (m), L_{lc} is the calculated liquid segment length (m), and L_{tc} is the total gas and liquid segment length during each operation of the high-speed valve (m).

2. Methodology

(2) Mass transfer measurement

The rate of gas absorption per unit volume (N , mol/m²·s⁻¹) was expressed as follows.

$$N = k_L (C^* - C) \quad (2.5)$$

where k_L is the mass transfer coefficient; and C and C^* are the solute and saturation concentrations, respectively, for a given gas composition. In the current experimental setup with configuration (a) in Fig. 2.5, gas absorption occurred in two different sections: the flask and the microchannels. Assuming a uniform solute concentration and neglecting mass transfer between the liquid film and the gas segment, the variation in the species absorbed in water can be described by the following equation.

$$(V_b + V_s) \frac{dC}{dt} = V_b [k_L a]_b (C^* - C) + V_s [k_L a]_s (C^* - C) \quad (2.6)$$

where, subscripts b and s denote flask and microchannel, respectively. As the microchannel volume is much smaller than that of the flask, V_s on the left-hand side can be neglected. This leads to the following expression for the concentration change due to absorption:

$$\frac{dC}{dt} = [k_L a]_{overall} (C^* - C) \quad (2.7)$$

where

$$[k_L a]_{overall} = [k_L a]_b + \frac{V_s}{V_b} [k_L a]_s \quad (2.8)$$

Integration of Eq. 2.7 yields the following expression, which can be used to determine $[k_L a]_{overall}$ from the experimental data. Here, $[k_L a]_{overall}$ is considered to be constant over time.

2. Methodology

$$\ln \frac{C^* - C_0}{C^* - C} = [k_L a]_{overall} t \quad (2.9)$$

$[k_L a]_b$ can be directly measured in an absorption experiment using configuration (b) in Fig. 2.5, wherein the measured increase in the solute concentration is solely due to the absorption in the flask by bubbles.

2.3 Preparation and characterization

(1) X-ray diffraction (XRD)

Powder X-ray diffraction (XRD) is widely used to examine the crystal structure of nanoparticles. In this study, the crystal structure of the particles was studied at room temperature using Cu K α radiation, which is a common choice for XRD experiments. The X-ray diffractometer is from Rigaku (RINT2500).

(2) Scanning Electron Microscopy (SEM)

Scanning Electron Microscopy is a powerful imaging technique used to observe the surface morphology of various materials at high resolution. SEM can reveal valuable information on shape, size, surface texture and particle distribution, which can provide a comprehensive understanding of material properties. In this study, the morphology of the nanoparticle was firstly examined using a SEM instrument, specifically the JEOL JSM-6700F.

(3) Transmission Electron Microscopy (TEM)

Transmission Electron Microscopy is a more powerful microscopy technique that allows for the observation of thin samples at extremely high resolution. A beam of electrons is accelerated and directed through the thin sample, and the transmitted electrons are then collected and used to form an image on a fluorescent screen or a digital detector.

2. Methodology

TEM is particularly useful for studying nanoscale materials and characterizing various types of particles, such as nanoparticles, nanowires, and nanocomposites. It provides valuable information about the internal structure and crystallinity of the particles, complementing the surface information obtained through SEM. In this study, the TEM instrument employed is from JEOL (JEM-1010).

(4) Nanoparticle Size Measurement

The nanoparticle size was measured from TEM images using the Nano Measure software (version 1.2.5), developed by Jie Xu from Fudan University, China [107]. For each sample, measurements were taken from over 60 nanoparticles, with the gathered data statistically analyzed using OriginPro 2023 (10.0.0.154 (Academic), OriginLab Corporation).

3

Segment Length Control by Using a High-speed Valve

3.1 Segment lengths at low frequencies

3.1.1 Influence of valve frequency on segment length

The investigation was first conducted without the high-speed valve, and this was done as contrastive experiment, the liquid and gas flow rates were set to 2.0 mL/min each. The segment lengths were obtained using the modified dynamic image measurement method, and an average value from ten segments from different images was used to represent the segment length, as shown in Table 3.1. Both the gas and liquid segment lengths trended to be constant, in agreement with other works in the literature.

Table 3.1 Segment lengths obtained without the high-speed valve

Phase	Average Length (mm)	Standard Deviation	Measured Length (mm)									
			NO.1	NO.2	NO.3	NO.4	NO.5	NO.6	NO.7	NO.8	NO.9	NO.10
Gas	1.27	2.8%	1.26	1.27	1.30	1.27	1.29	1.23	1.25	1.24	1.23	1.31
Liquid	1.23	3.9%	1.24	1.19	1.19	1.21	1.19	1.29	1.24	1.26	1.28	1.19

3. Segment Length Control by Using a High-speed Valve

After installing the high-speed valve on the gas tube, the operation of the high-speed valve at specific frequencies caused the segment lengths to change, as shown in Fig. 3.1. The segment lengths decreased gradually with an increase in valve frequency from 6 to 12 s^{-1} . However, segment generation became unstable at frequencies of 15 s^{-1} . The segment lengths at different frequencies are detailed in Fig. 3.2.

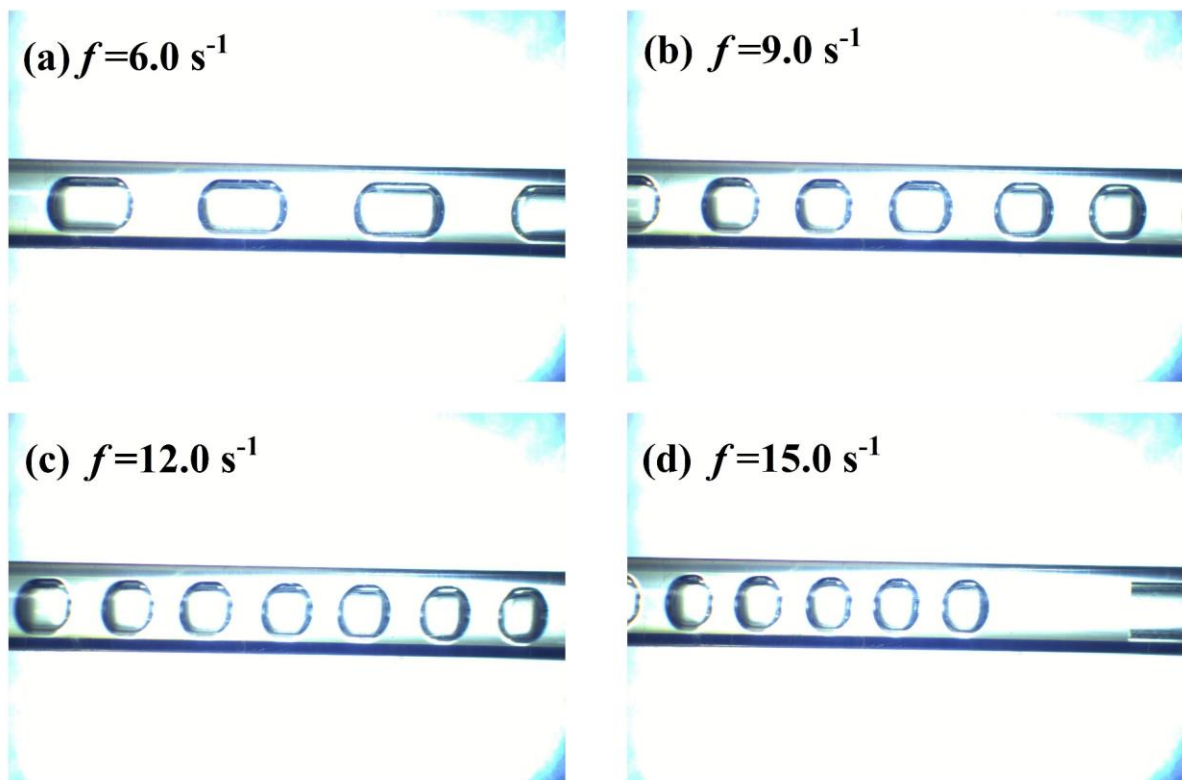


Fig. 3.1 Segment images obtained at various high-speed valve frequencies

As shown in Fig. 3.2, the segment lengths of both the liquid and gas phases were effectively changed by increasing the valve frequency from 6 to 14 s^{-1} . At a frequency of 15 s^{-1} , the segment length of both phases was nearly identical as that at 14 s^{-1} . Both the liquid and gas segment lengths were significantly different compared with the average value at the frequency range of 6–10 s^{-1} , and the difference became smaller when the frequency was higher than 10 s^{-1} . Further, the gas-to-liquid segment length ratio was

3. Segment Length Control by Using a High-speed Valve

maintained at approximately 1.10 rather than 1.00, as predicted by the mass balance. This difference might be due to the compressibility of the gas because the segment length measurement method was developed based on static images, in which the pressure of the system at equilibrium with the atmosphere and this could have allowed for expansion of the gas volume to some extent. The segment length obtained without the high-speed valve is shown on the right-hand side of Fig. 3.2, it can be seen that the operation of the high-speed valve achieved stable control of the segment length within a wide range.

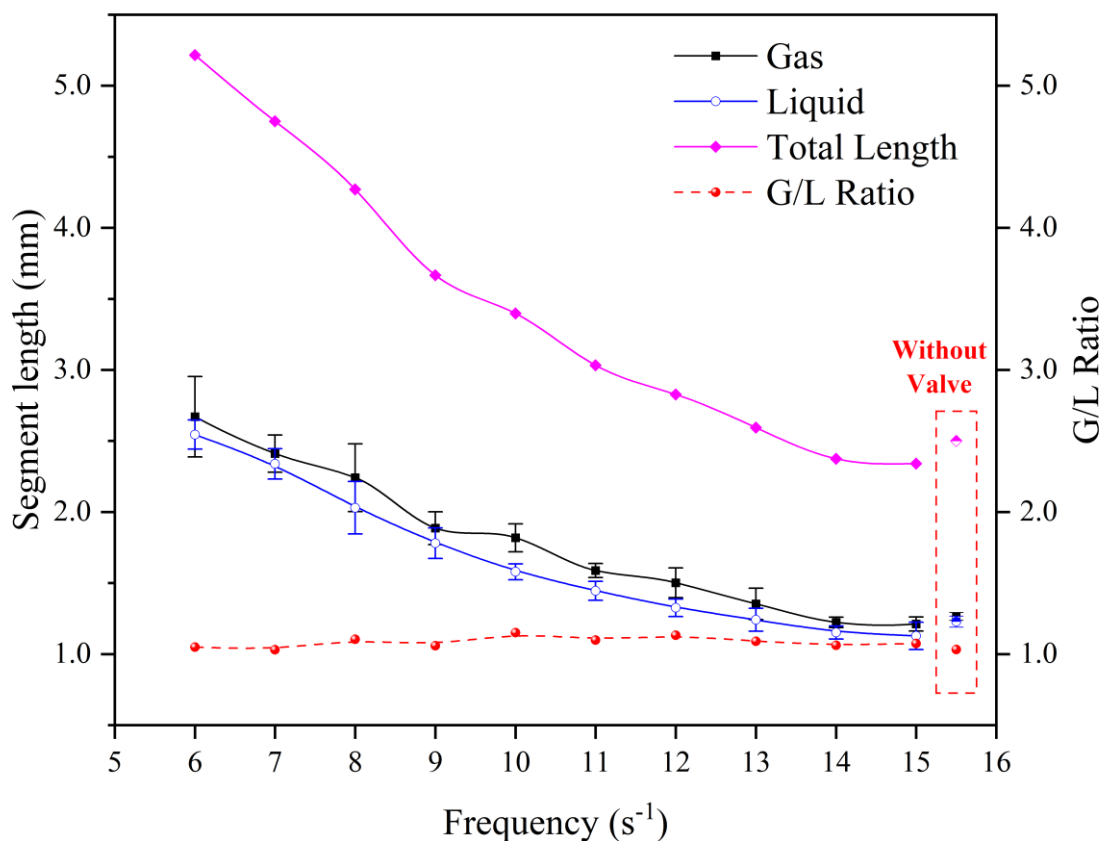


Fig. 3.2 Influence of valve frequency on segment length

3.1.2 Reproducibility

To validate the function of the high-speed valve, two reproducibility experiments

3. Segment Length Control by Using a High-speed Valve

were conducted at the same fluid flow rate and valve frequencies of 6–15 s^{-1} (Fig. 3.3). The results clearly indicate that the liquid segment generation was successfully reproduced at all frequencies. Thus, the high-speed valve is effective at manipulating the segment length at lower frequencies ($f \leq 15.0 \text{ s}^{-1}$).

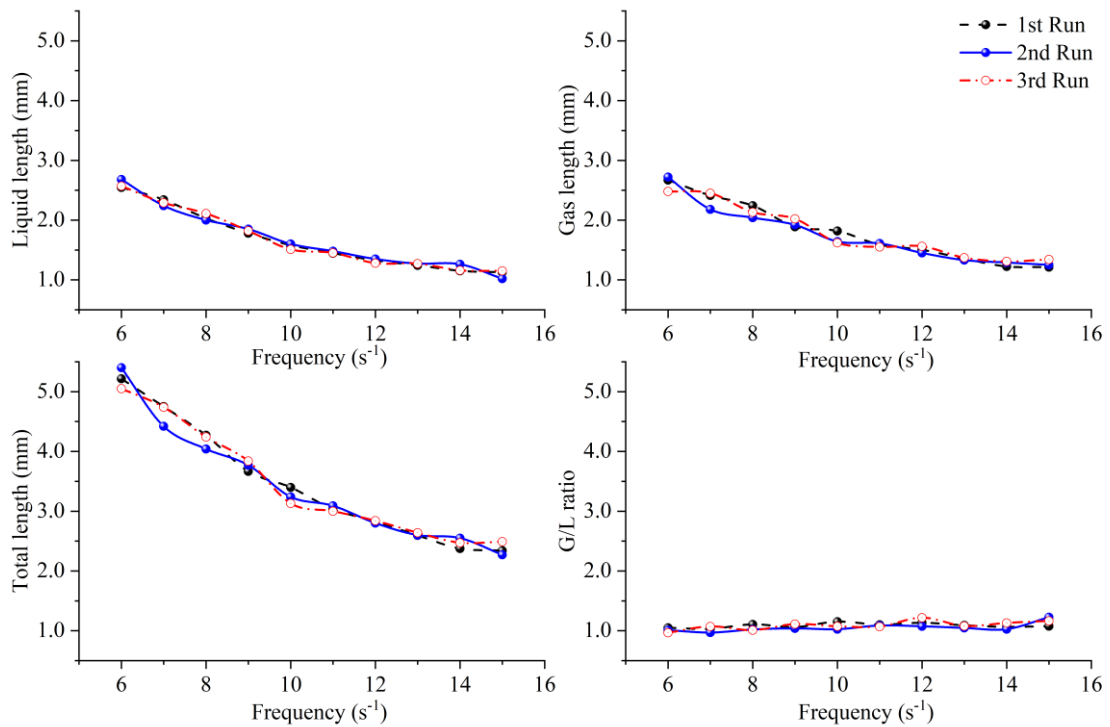


Fig. 3.3 Reproducibility of segment length control at various high-speed valve frequencies

This system shows a significant advantage over that developed by Zhang et al. [84], whom observed random segment lengths from approximately 5 to 13 mm at valve frequencies lower than 8 s^{-1} . In contrast, in the current system, the segment lengths can be regulated from 2.6 to 1.2 mm by increasing the high-speed valve frequency from 6 to 14 s^{-1} . This control over segment generation may be attributable to the high accuracy of the actuator, which enables the valve to complete 100 or more open–close cycles every second, as well as the low flow rates of the gas and liquid phases. Furthermore, the small

3. Segment Length Control by Using a High-speed Valve

inner diameter (1.1 mm) of the T-junction also facilitates the formation of fine segments.

3.2 Segment lengths at higher frequencies

3.2.1 Experimental results

To investigate the influence of higher valve frequencies on segment length, the upper limit of the valve frequency in the reproducibility experiment was extended to 40 s^{-1} . The segment lengths observed at various valve frequencies are detailed in Fig. 3.4 and a representative segment image is shown in Fig. 3.5. As seen in Fig. 3.4, an evident fluctuation occurred at frequencies of $15\text{--}22 \text{ s}^{-1}$, and then, the segment length tended to become stable at higher frequencies. Furthermore, the liquid segment length showed a larger deviation compared to the gas segment length.

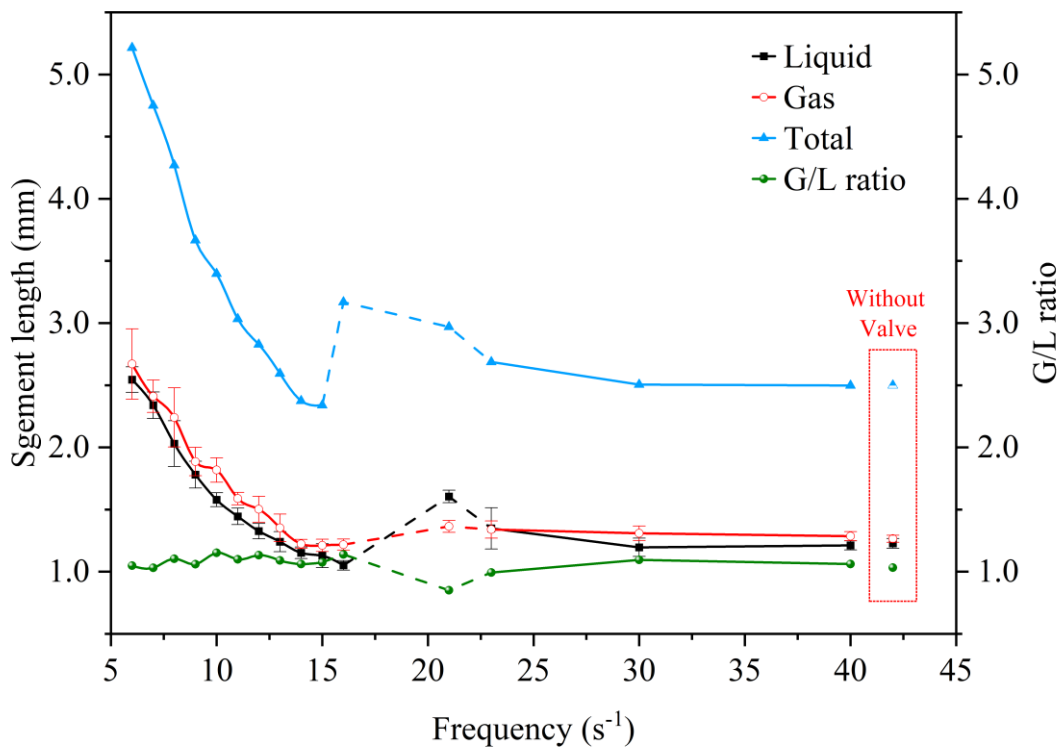


Fig. 3.4 Influence of higher valve frequencies on segment length

3. Segment Length Control by Using a High-speed Valve

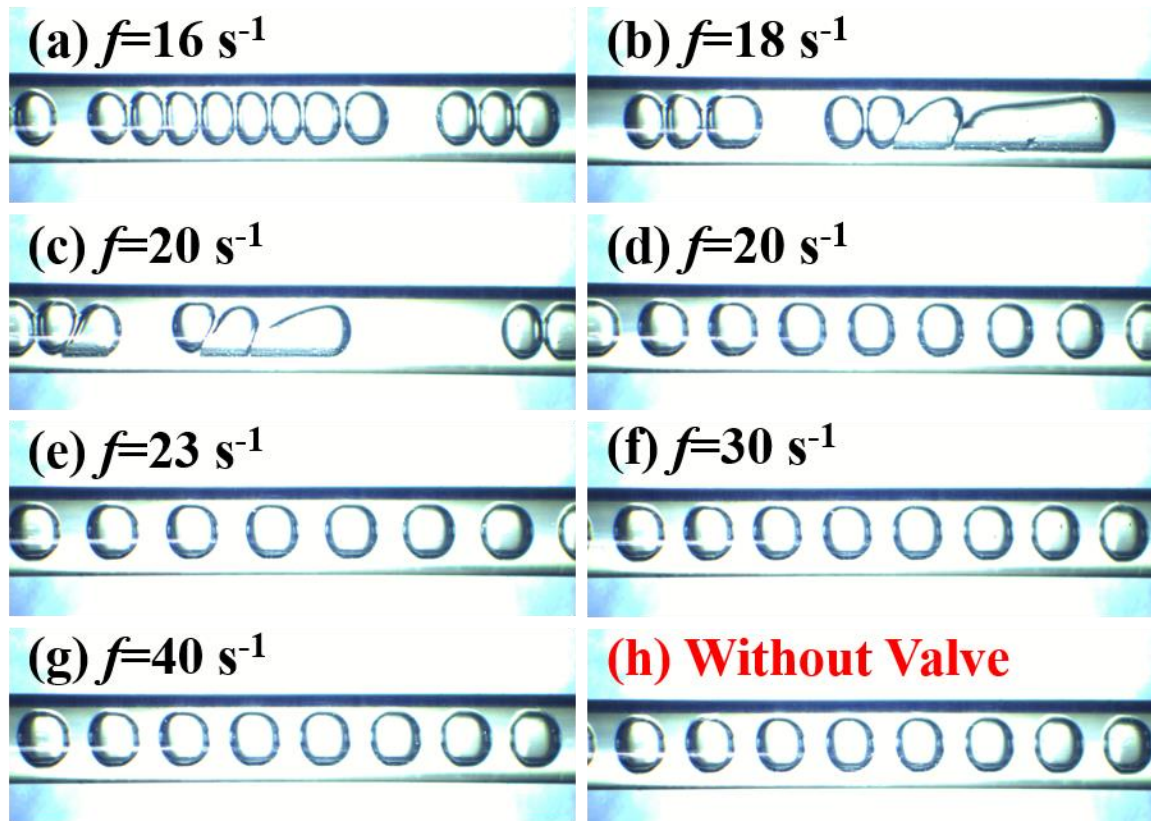


Fig. 3.5 Segment images at higher valve frequencies

The segment images in Fig. 3.5 can provide insights into the segment length fluctuation observed at frequencies of 15–22 s^{-1} . Fig. 3.5(a) shows that segments at frequency of 16 s^{-1} were still relatively short, but the small segments tend to merge and form longer segments. This behavior may be attributable to the surface tension of the segments and the vibration caused by the operation of the high-speed valve. When the valve frequency continued to increase, as shown in Fig. 3.5 (b) and (c), the segment generated in the T-junction was too small to maintain its initial shape in the microchannel and coalesced with the development of the segment flow. Interestingly, uniform segments were also observed at frequency of 20 s^{-1} (Fig. 3.5 ([e])), which indicates that the segmented flow was unstable in the microchannel. Upon increasing the operating

3. Segment Length Control by Using a High-speed Valve

frequency further, the segment length remained nearly unchanged, as shown in Fig. 3.5 (d)–(g), and the obtained segment lengths were nearly identical to the segments obtained without the high-speed valve, as seen in Fig. 3.5(h), but these segment images reveal no behavior that can explain the observed phenomenon.

3.2.2 Explanation based on segment formation mechanism

The formation of gas–liquid segments in T-junctions has been frequently discussed, and in the typical mechanism of segment generation, the process is divided into two periods: The gas filling period and the squeezing period [42,43]. According to this mechanism, the formation time of the gas segment (t_g) is the sum of the filling time (t_f) and the squeezing time (t_s), as expressed in Eq. 3.1.

$$t_g = t_f + t_{sq} \quad (3.1)$$

$$t_{sq} = \frac{21.88}{5.437(v_l/d_i)^{1.21}(v_g/d_i)^{0.54}} \quad (3.2)$$

Ahn et al. [42] revealed that t_s is a function of both the liquid and gas velocities calibrated by the width of the rectangular channel. By substituting the width of the rectangular channel with the diameter of the tube used in this study, Eq. 3.2 was used to calculate t_{sq} . As a note of caution, the gas velocity was constant in the conventional segment generating system, whereas the utilization of the high-speed valve introduced periodic pressure fluctuations in the gas inlet of the T-junction, resulting in corresponding variations in the gas velocity.

The following qualitative analysis may provide an intuitive understanding of the influence of the high-speed valve frequency on segment length. Fig. 3.6(a) shows the voltage input of the high-speed valve at a specific frequency and the corresponding variation in gas velocity at the T-junction gas inlet. When the high-speed valve is supplied

3. Segment Length Control by Using a High-speed Valve

with a voltage, it opens and allows the gas to flow into the volume existing between the valve and the T-junction; consequently, the gas velocity in this volume increases from a minimum value (v_{min}) until the voltage is removed at a maximum value (v_{max}). Subsequently, the voltage becomes zero and the valve closes, resulting in the gas velocity to decrease from v_{max} to v_{min} at the end of the cycle. The next cycle continues as the supplied voltage changes from v_{min} . When the gas velocity begins to increase, the squeezing period ends and the filling period begins. Hence, the gas velocities in both the filling and squeezing periods change continuously.

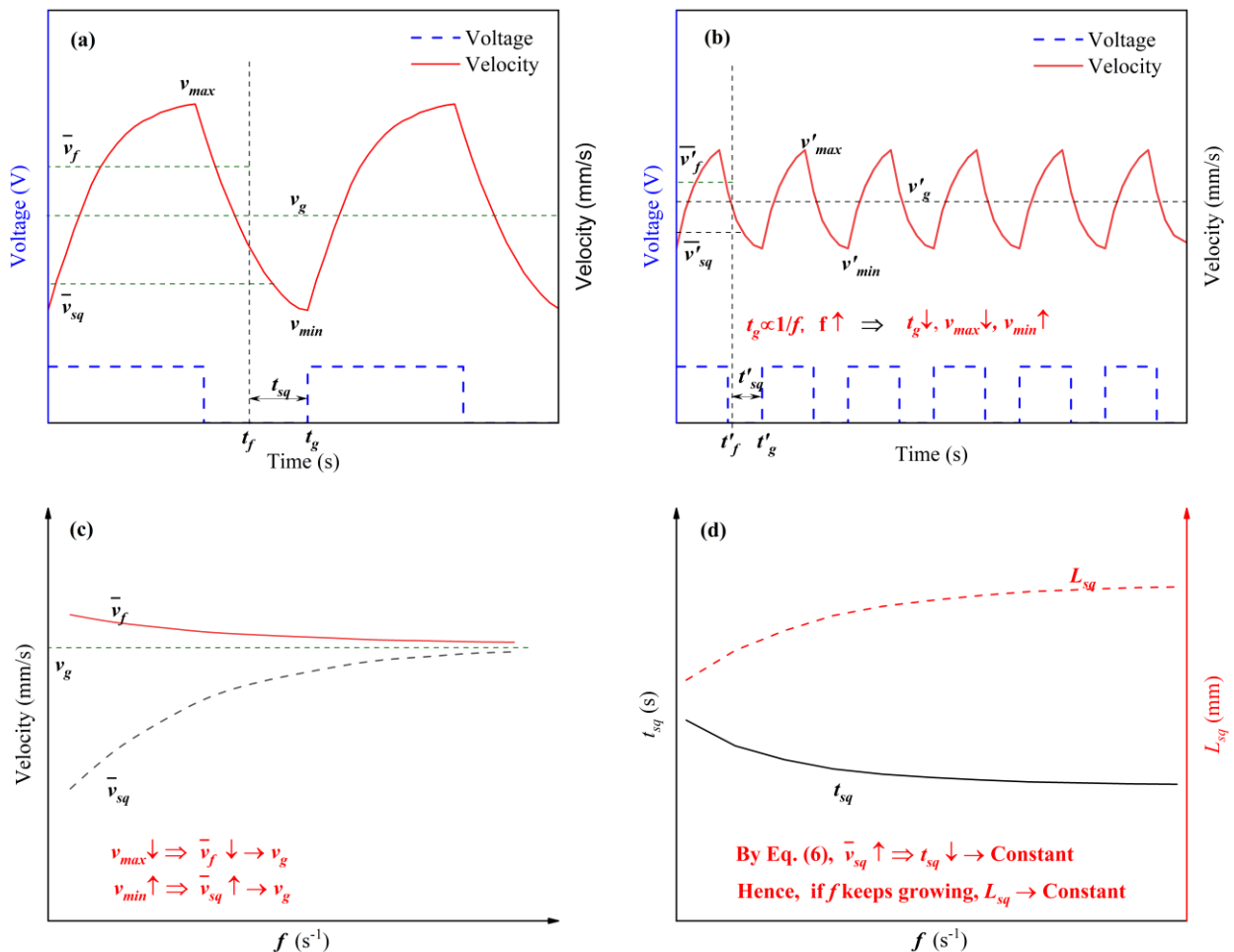


Fig. 3.6 Qualitative analysis of gas velocity variation at different valve frequencies

3. Segment Length Control by Using a High-speed Valve

This discussion is simplified by introducing the average gas velocities during the filling period (\bar{v}_f) and squeezing period (\bar{v}_{sq}), which must satisfy Eq. 3.3, where v_g is the gas velocity calculated using only the gas flow rate from Eq. 2.1. As the filling period covers most of the gas segment generation time, \bar{v}_f is larger than \bar{v}_{sq} and the following correlation is obeyed: $\bar{v}_{sq} < v_g < \bar{v}_f$.

When the frequency of the high-speed valve increases, the gas feed period becomes shorter and the minimum gas velocity (v'_{min}) and average gas velocity in the squeezing period (\bar{v}'_{sq}) increase, whereas the maximum gas velocity (v'_{max}) and average gas velocity in the filling period (\bar{v}'_f) decrease, as indicated in Fig. 3.6 (b). Based on the above discussion, Fig. 3.6(c) shows the influence of the valve frequency on \bar{v}_f and \bar{v}_{sq} , both of which approach the constant v_g value. Furthermore, both t_{sq} and the segment length formed during the squeezing period (L_{sq}), as determined by substituting v_g with \bar{v}_{sq} in Eq. 3.2 and using Eq. 3.4, are nearly constant at high valve frequencies (Fig. 3.6[d]). According to this analysis, \bar{v}_f also approaches v_g at high frequencies and the segment length formed during the filling period (L_f) can also be assumed to be approximately constant. Therefore, as the sum of L_{sq} and L_f , the total gas segment length becomes nearly constant at high valve frequencies.

$$v_g = \frac{\bar{v}_f t_f + \bar{v}_{sq} t_{sq}}{t_g} \quad (3.3)$$

$$L_{sq} = \bar{v}_{sq} t_{sq} \quad (3.4)$$

3. Segment Length Control by Using a High-speed Valve

3.3 Influence of flow rate on segment length

3.3.1 By changing flow rate ratio

The influence of the flow rate ratio on segment length was investigated at a high-speed valve frequency of 8 s^{-1} (Fig. 3.7). When the gas flow rate was constant (2.0 mL/min) and the liquid flow rate was varied ($1.00, 1.33, 1.67, 2.00, 2.33,$ and 2.67 mL/min) (Fig. 3.7[a]), the liquid segment length increased proportionately with liquid flow rate. The gas segment length did not change significant at liquid flow rates below 2.67 mL/min , but at higher liquid flow rates, the segment lengths of both phases deviated from the theoretical values.

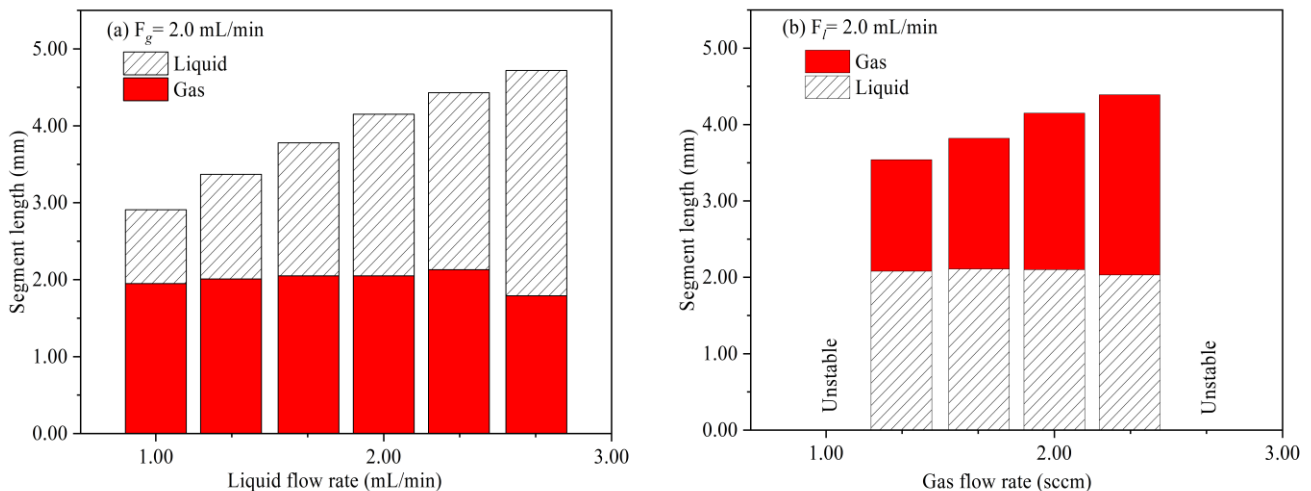


Fig. 3.7 Influence of flow rate on segment length at a high-speed valve frequency of 8 s^{-1}

When the liquid flow rate was constant and the gas flow rate was varied (Fig. 3.7[b]), the gas flow rate range that generated uniform segmented flow was much narrower. When the gas flow rate was under 1.33 mL/min or above 2.33 mL/min , the segment length could

3. Segment Length Control by Using a High-speed Valve

not be measured because of its random distribution caused by coalescence of tiny segments. Meanwhile, the coalescence of tiny segments also occurred when the liquid flow rate range was further extended. Therefore, the gas-to-liquid flow rate ratio should be in the range of 0.7–1.2 to generate a steady segmented flow.

3.3.2 By changing total flow rate

In the preceding sections, the flow rates of the liquid and gas phases were 2.0 mL/min when realizing the control of segment length with the high-speed valve. In this section, the flow rate of the two phases was increased to 4.0 mL/min, and the images of the segmented flow at different valve frequencies are shown in Fig. 3.8. The influence of valve frequency on the segment length is shown in Fig. 3.9.

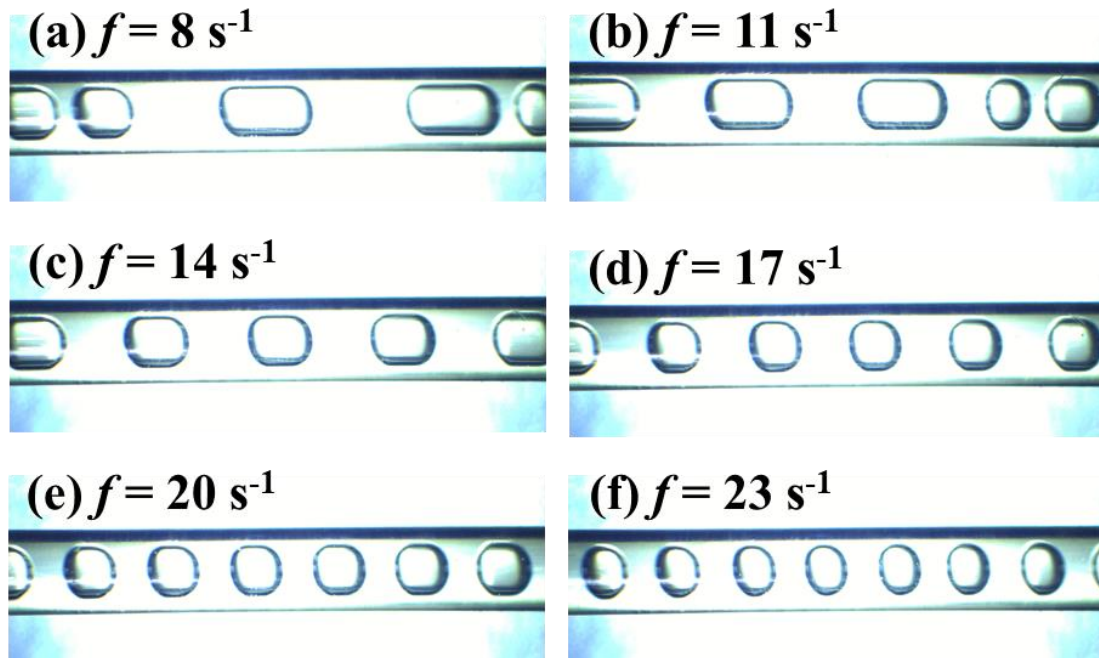


Fig. 3.8 Images of the segmented flow at different valve frequencies

3. Segment Length Control by Using a High-speed Valve

As shown in Figs. 3.8 and 3.9, the segment length decreased with increasing the valve frequency from 8 to 23 s^{-1} , when the flow rates of both phases were 4.0 mL/min. The segment length showed a higher deviation when $f \leq 11 s^{-1}$, which is in accordance with the trend at a flow rate of 2.0 mL/min.

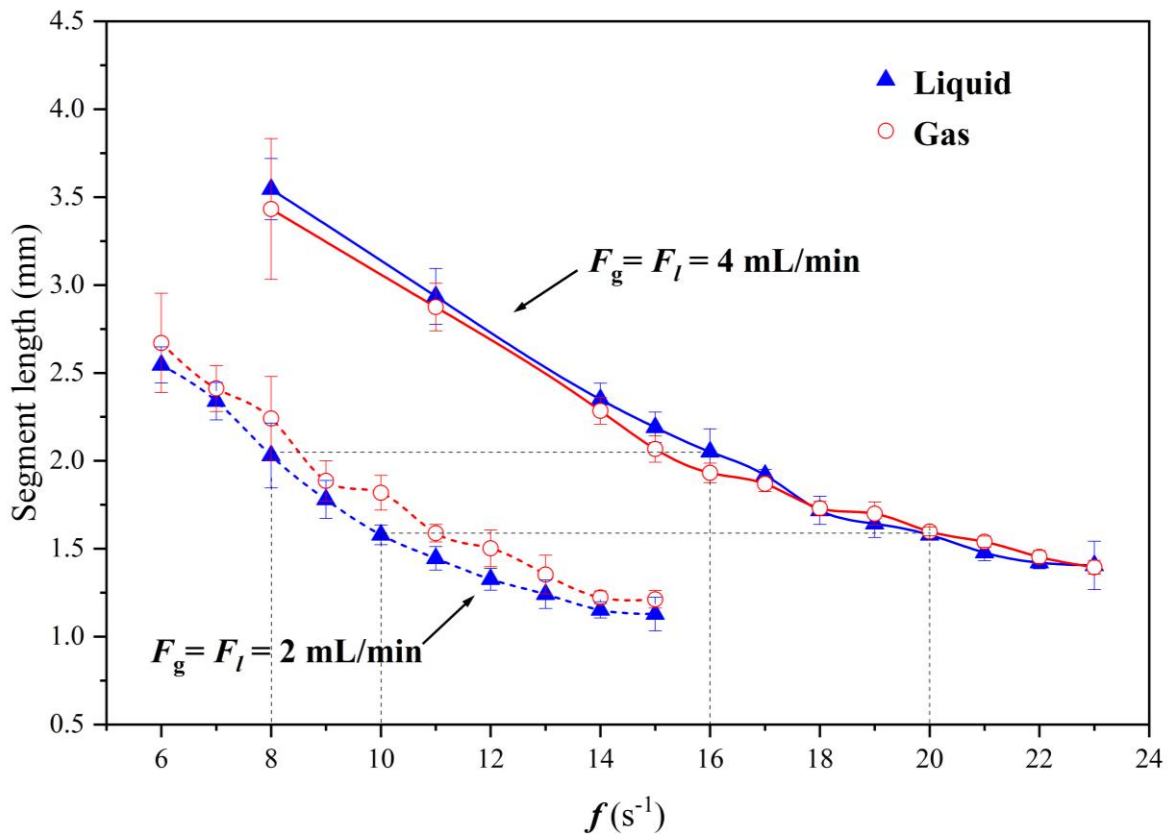


Fig. 3.9 Influence of valve frequency on the segment length

Essentially, the segment length was not uniform at lower frequencies, as shown in Figs. 3.8 (a) and (b). Meanwhile, when the flow rates of both phases doubled, the necessary valve frequency corresponding to the same liquid segment length also doubled, which is reasonable according to the mass balance. Compared with the liquid segment length, the gas segment length curve has a larger residual.

3. Segment Length Control by Using a High-speed Valve

3.4 Correlation for predicting segment length

The above findings indicate that the segment length controlled by the high-speed valve can be predicted using the biphasic flow rate, channel geometry, and operation parameters. As mentioned previously, the compressibility of the gas caused the segment length to vary with pressure. Therefore, the gas segment length (L_g) calculation should take the system pressure into consideration, as shown in Eq. 3.5.

$$L_g = \frac{p_d}{p_a} \frac{1}{f} \frac{F_g}{(\pi/4) d_i^2} \quad (3.5)$$

where p_d is the system pressure during dynamic operation (kPa) and p_a is the system pressure under static measurement conditions (kPa). However, despite the fact that the input pressure was released and the pressure of the system was allowed to balance with the atmosphere during static measurement conditions, the force between the segments and the channel caused p_a to be slightly higher than atmospheric pressure, making it difficult to determine an accurate value. Consequently, p_d/p_a in Eq. 3.5 was replaced with an empirical factor to give Eq. 3.6.

$$L_g = 1.04 \frac{1}{f} \frac{F_g}{(\pi/4) d_i^2} \quad (3.6)$$

In contrast, as the liquid volume was not affected by pressure, the liquid segment length (L_l) can be calculated using Eq. 2.3, and the biphasic segment length (L_t) during operation of the high-speed valve can be expressed by Eq. 3.7.

$$L_t = L_l + L_g \quad (3.7)$$

As shown in Fig. 3.10, when $F_g = F_l = 2.0$ mL/min, the experimentally measured segment lengths of both phases were in accordance with the predicted values at low frequencies ($f \leq 14$ s⁻¹), whereas substantial deviations were observed at higher

3. Segment Length Control by Using a High-speed Valve

frequencies. Therefore, the developed correlation is applicable in the frequency range of $8\text{--}14\text{ s}^{-1}$ when $F_g = F_l = 2.0\text{ mL/min}$

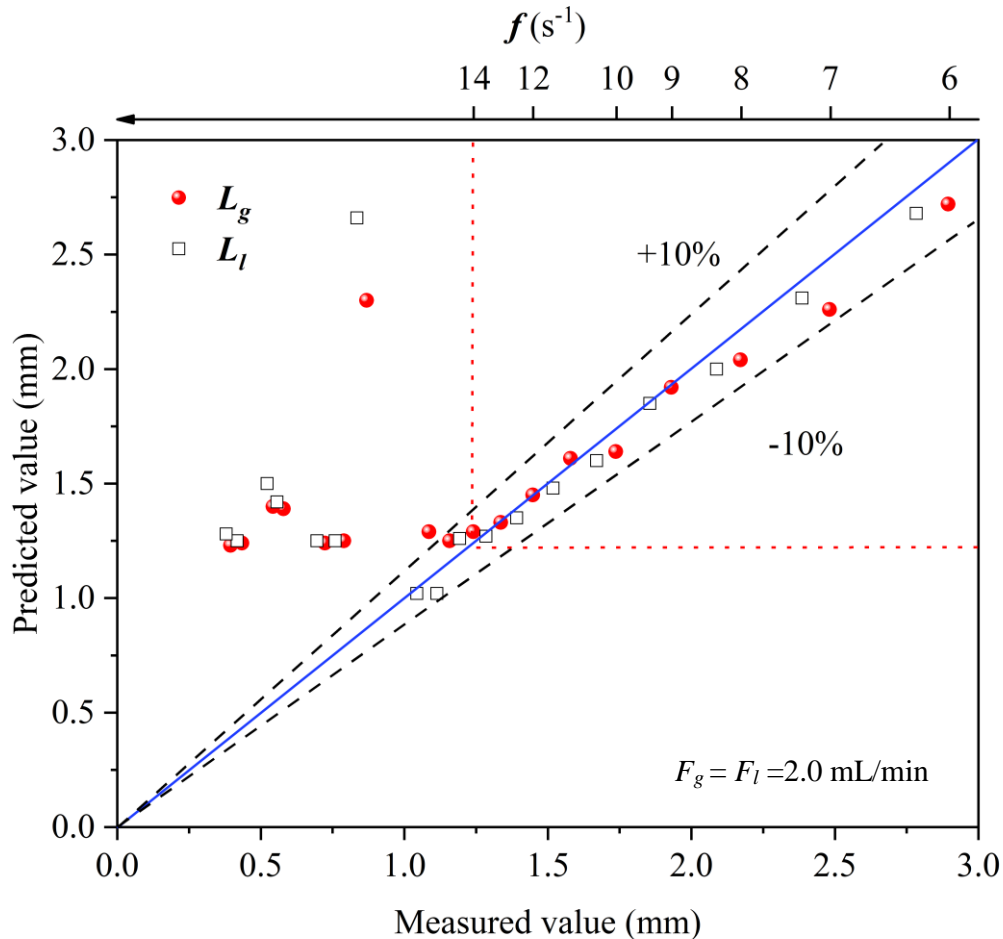


Fig. 3.10 Performance of the correlation for predicting segment length at low flow rate

Fig. 3.11 shows the comparison of the measured and predicted segment lengths using Eq. 2.3 and 3.6 when $F_g = F_l = 4.0\text{ mL/min}$. Evidently, the liquid segment length fit better with the correlation, whereas the gas segment length had a slightly larger error.

Overall, both the liquid and gas segment lengths agreed well with the correlation for $14\text{ s}^{-1} \leq f \leq 23\text{ s}^{-1}$. This suggests that a valve frequency within 23 s^{-1} is capable of regulating the segment length at a flow rate of 4.0 mL/min for each fluid.

3. Segment Length Control by Using a High-speed Valve

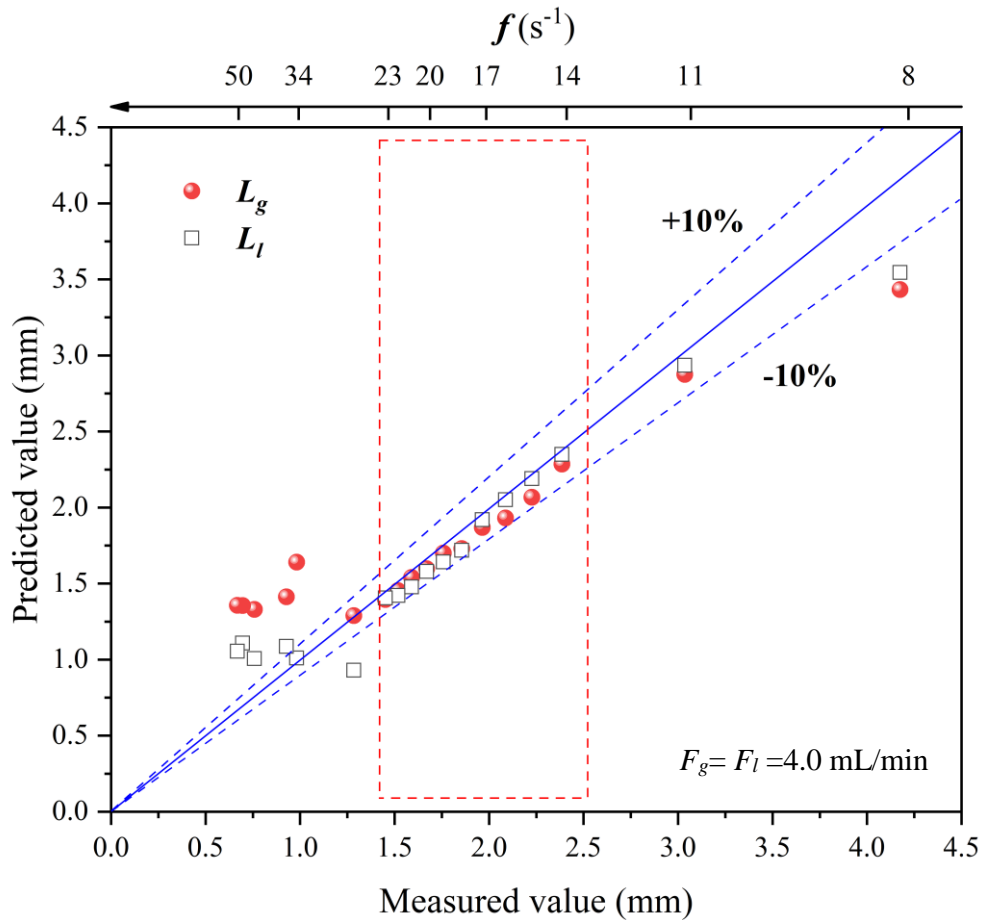


Fig. 3.11 Performance of the correlation for predicting the segment length at higher flow rate

3.5 Conclusions

The regularly control of the segment length in a gas–liquid microchannel system was achieved by employing a high-speed valve in a segmented flow generating device. The segment length generated in the microchannel without the high-speed valve was determined by the flow rate and channel size, which remained constant once flow began. Notably, by adjusting the operating frequency of the high-speed valve, the segment length was successfully manipulated within a wide frequency range. The high-speed valve was

3. Segment Length Control by Using a High-speed Valve

able to reproducibly control the segment length at frequencies below 15 s^{-1} .

However, the tiny generated segments could not be maintained in the microchannel when the frequency exceeded 15 s^{-1} , and segment length was not evidently influenced by value frequencies exceeding 22 s^{-1} . This behavior was explained by a qualitative analysis from the perspective of the segment formation mechanism.

In addition, a gas-to-liquid flow rate ratio in the range of 0.7–1.2 is deemed necessary for regular segmented flow. Based on a mass balance, a correlation between valve frequency, biphasic flow rate, and channel diameter was proposed to predict the segment length controlled by the high-speed valve, which agreed with the experimental results.

In summary, the results of this study offer a novel strategy for controlling segment length in microchannels, which will improve the performance of gas–liquid reactions in microreactors and aid in the design of microreactor systems.

4

Mass Transfer Measurement in Length-controlled Segmented Flow

The detailed exploration of manipulating segment length through adjustments in valve frequency has been extensively covered in Chapter 3. In this chapter, a set of experiments is carried out to elucidate how the length of segments affects mass transfer performance. Furthermore, correlations are put forward to forecast both the specific area and the rate of mass transfer in segmented flows. The findings of this research endeavor will contribute to an enhanced comprehension of mass transfer within segmented flows and foster the utilization of segmented flows in microreactors.

4.1 Influence of valve frequency on volumetric mass transfer coefficient

Mass transfer measurements were performed with a flow rate of 4.0 mL/min for both phases, and the microchannel length was 2,650 mm. $[kLa]_{overall}$ and $[kLa]_b$ at different valve frequencies were determined using configurations (a) and (b) in Fig. 2.5, respectively, and the coefficients were plotted against the valve frequency in Fig. 4.1. Next, $(V_s/V_b) [kLa]_s$ could be obtained by simple subtraction according to Eq. 2.8. Fig. 4.1 clearly shows the growth of $[kLa]_{overall}$ at the valve frequencies of 8 s^{-1} to 14 s^{-1} , which

4. Mass Transfer Measurement in Length-controlled Segmented Flow

tends to be steady when the valve frequency is higher than 14 s^{-1} . By contrast, the value of $[k_L a]_b$ exhibited no significant deviation over the entire valve frequency range.

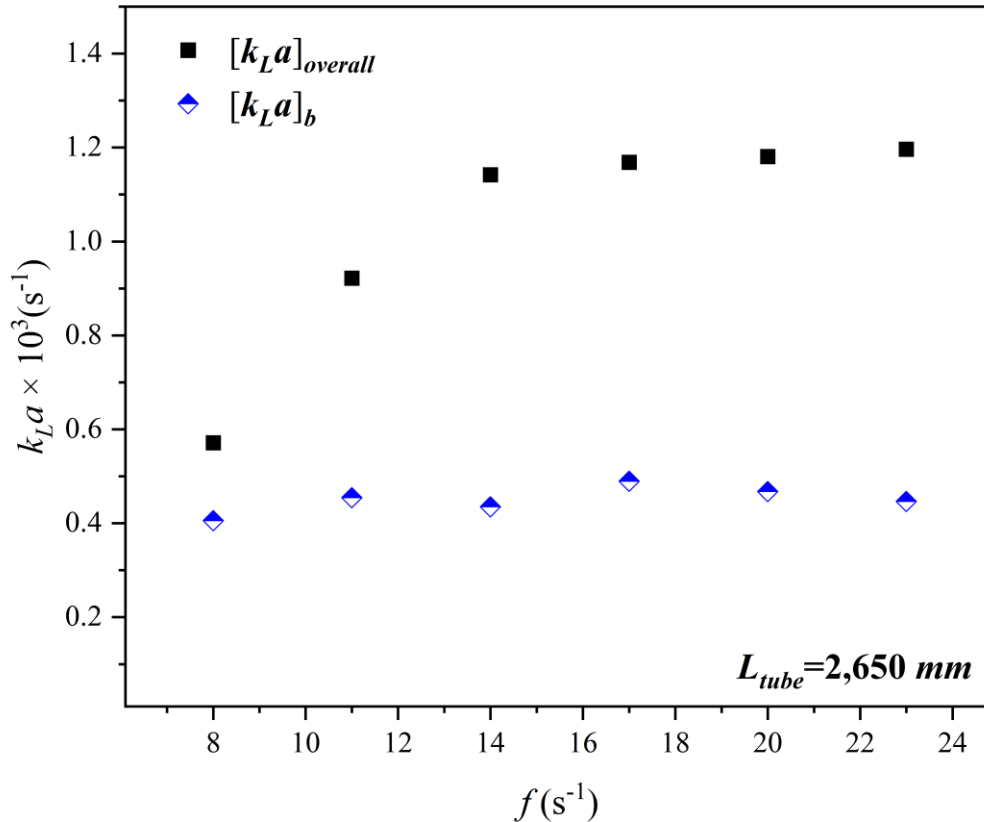


Fig. 4.1 Mass transfer performance at different valve frequencies

The majority of the increase in $[k_L a]_{overall}$ stemmed from the increase in the specific area at different valve frequencies, as indicated in Fig. 3.9. However, when $f \geq 14 \text{ s}^{-1}$ the specific area became sufficiently large such that the liquid segment was (or nearly) saturated with oxygen before leaving the tube. Thus, the contribution of the segmented flow to the increased oxygen concentration in the flask remained almost the same when $f \geq 14 \text{ s}^{-1}$. Meanwhile, oxygen occupied approximately 21% of the volume fraction in air for an equivalent volume of air and water; even when the water phase was saturated with

4. Mass Transfer Measurement in Length-controlled Segmented Flow

oxygen, less than 6% of the oxygen in the air was consumed, and the concentration of oxygen in the air separated from the segmented flow was still approximately 20%. Hence, the mass transfer process in the second flask of configuration (b) showed no significant differences at various valve frequencies, and the measured $[k_La]_b$ differed slightly, as shown in Fig. 4.1. Essentially, the contribution of the air bubbles to the increase in oxygen concentration in the flask always remained the same, despite the increase in the valve frequency. Therefore, $[k_La]_{overall}$ is nearly constant when $f \geq 14 \text{ s}^{-1}$.

4.2 Influence of tube length on volumetric mass transfer coefficient

To reveal the contribution of mass transfer in the segmented flow to $[k_La]_{overall}$, a series of experiments was performed by changing the tube length when $f = 17 \text{ s}^{-1}$. Fig. 4.2 shows the influence of tube length on $[k_La]_{overall}$. Evidently, when the tube length ranged from 1,400 to 2,650 mm at a valve frequency of 17 s^{-1} , $[k_La]_{overall}$ exhibited a remarkable linear correlation ($R^2 = 0.9999$) with the tube length and increased from 0.84×10^{-3} to $1.56 \times 10^{-3} \text{ s}^{-1}$; when the tube length exceeded 2,400 mm, $[k_La]_{overall}$ did not increase any further.

The change in the $[k_La]_{overall}$ within different microchannel lengths indicates that when the tube length exceeded 2,100 mm, the oxygen concentration in the liquid segment approached the equilibrium value in the microchannel. The increase in the oxygen concentration in the flask can be calculated using Eq. 2.7, where $[k_La]_s$ is the mass transfer coefficient in the segmented flow.

Herein, the valve frequency was fixed at 17 s^{-1} , thus resulting in a constant specific area of the segmented flow and maintaining $[k_La]_s$. Nevertheless, the residence time (or Δt) of the segmented flow increased with the tube length. Therefore, if the tube is sufficiently long, the liquid segment is (or is nearly) saturated with oxygen before leaving

4. Mass Transfer Measurement in Length-controlled Segmented Flow

the tube. Thus, the obtained $[k_L a]_{overall}$ had no distinct alteration when the tube length exceeded 2,100 mm.

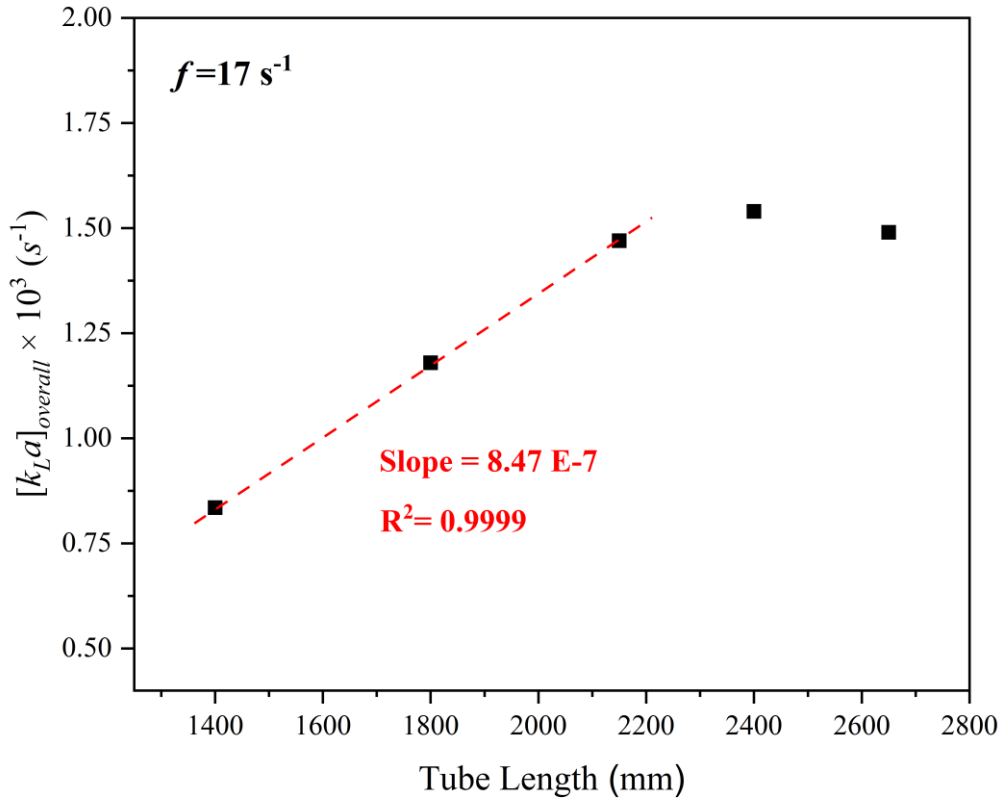


Fig. 4.2 Influence of tube length on $[k_L a]_{overall}$

Based on the data in Fig. 4.1, the $(V_s/V_b) [k_L a]_s$ determined using Eq. 2.8 is equivalent to the order of $[k_L a]_b$. However, the actual increase in oxygen concentration in the microchannel is larger than that in the flask, and $[k_L a]_s$ can be calculated using Eq. 4.1. Accordingly, after conducting mass transfer experiments with configuration (a) in Fig. 2.4, $[k_L a]_s$ can be determined from the recorded DO data, and the average $[k_L a]_b$ is determined in Section 4.1.

$$[k_L a]_s = \frac{V_b}{V_s} ([k_L a]_{overall} - [k_L a]_b) \quad (4.1)$$

4. Mass Transfer Measurement in Length-controlled Segmented Flow

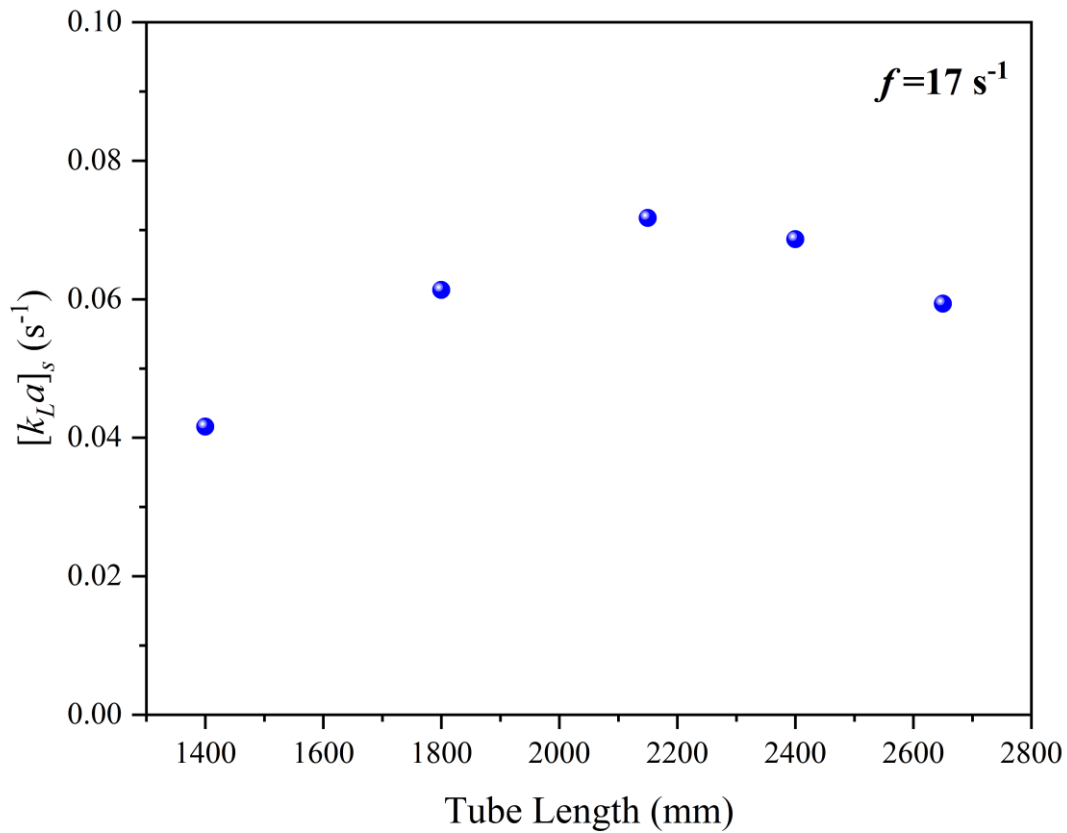


Fig. 4.3. Influence of the tube length on $[k_L a]_s$

Fig. 4.3 shows the $[k_L a]_s$ calculated using Eq. 4.1 with the same experimental parameters as those used in the experiments shown in Fig. 4.2. Evidently, the calculated $[k_L a]_s$ exhibited an abnormal trend: $[k_L a]_s$ should be constant when simply changing the tube length; however, it first increased and then decreased. This decrease can be explained by the saturation of water by oxygen when $L_{\text{tube}} > 2,000$ mm, and the mass transfer rate will be (or close to) zero after saturation. However, note that $[k_L a]_s$ is determined by the oxygen concentration difference between the inlet and outlet. Consequently, $[k_L a]_s$ decreased when the tube length continued to increase. This demonstrates that some deviation occurs when calculating $[k_L a]_s$ with Eq. 4.1. $[k_L a]_s$ can also be determined from Fig. 4.2. By substituting V_s into the expressions for d_i and L in Eq. 2.8, Eq. 4.2 can be

4. Mass Transfer Measurement in Length-controlled Segmented Flow

used to express the relationship between $[k_L a]_{overall}$ and L .

$$[k_L a]_{overall} = [k_L a]_b + \frac{(\pi/4) d_i^2}{V_b} [k_L a]_s L \quad (4.2)$$

As discussed in Section 4.1, $[k_L a]_b$ can be regarded as a constant ($4.48 \times 10^{-4} \text{ s}^{-1}$) in this study; thus, the gradient of the increase of $[k_L a]_{overall}$ in Fig. 4.2 equals $\frac{(\pi/4) d_i^2}{V_b} [k_L a]_s$. The determined $[k_L a]_s$ was 0.149 s^{-1} , which is 332.6 times larger than $[k_L a]_b$ and approximately twice as large as the data in Fig. 4.3; nonetheless, $[k_L a]_s$ in Fig. 4.3 and determined by Eq. 4.2 in Fig. 4.2 are both of the order of 10^{-1} s^{-1} . This calculation indicates that the mass-transfer rate in a segmented flow is over two orders of magnitude higher than that in a conventional bubble flow. Hence, to avoid underestimation of $[k_L a]_s$ when the tube was too long, the tube length was fixed at 1,400 mm in the following experiments.

4.3 Influence of segment length on instinct volumetric mass transfer coefficient

As discussed in Sections 4.1 and 4.2, $[k_L a]_{overall}$ increases with the valve frequency when $f \leq 14 \text{ s}^{-1}$, and this increase is attributed to the increase in $[k_L a]_s$. To reveal the influence of f on $[k_L a]_s$, a series of measurement experiments was conducted with $L_{tube} = 1,400 \text{ mm}$, and the results are shown in Fig. 4.4, which highlights the gradual growth of $[k_L a]_s$ against the increase in f from 11 to 17 s^{-1} . Evidently, after linear fitting, the correlation coefficient was as high as 0.9978. However, when $f \geq 20 \text{ s}^{-1}$, $[k_L a]_s$ became steady, thus indicating that the water segments in the microchannels were saturated with oxygen. This trend further supports the enhanced mass transfer within the segmented flow, and the high mass transfer coefficient between the gas and liquid segments enables the rapid mass transfer of the two phases.

4. Mass Transfer Measurement in Length-controlled Segmented Flow

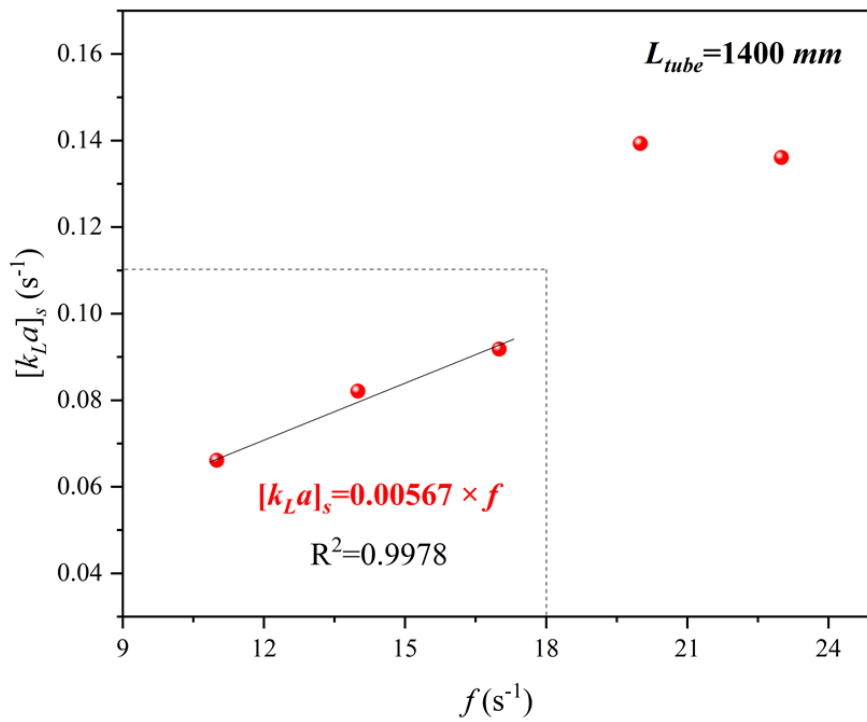


Fig. 4.4 Influence of valve frequency on $[k_L a]_s$

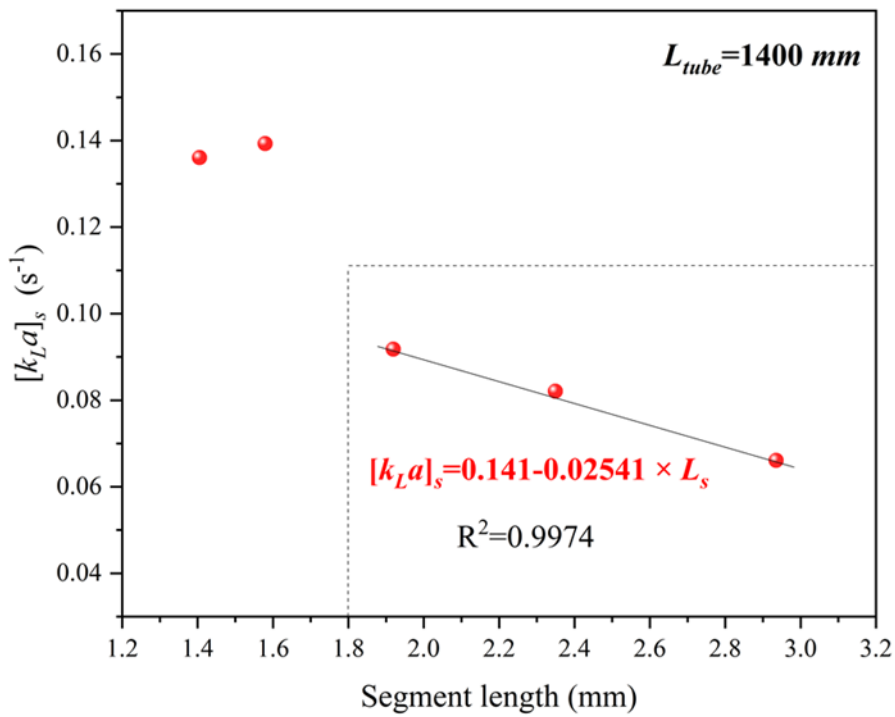


Fig. 4.5 Influence of segment length on $[k_L a]_s$

4. Mass Transfer Measurement in Length-controlled Segmented Flow

Meanwhile, $[k_L a]_s$ has a negative linear relationship with the segment length (Fig. 4.5), which is opposite to that of the valve frequency. This can be explained easily by the inverse proportion between f and the segment length.

4.4 Influence of valve frequency on the specific area

The specific surface area a can be calculated through the segment length using the equation proposed by Sobieszuk *et al.* [47]. Fig. 4.6 reveals a marked linear correlation ($R^2 = 0.9999$) between the specific surface area a , determined by the measured segment length, and the valve frequency.

As the segment length can be predicted using Eq. 2.5; by substituting Eq. 2.5 into the equation for calculating a , Eq. 4.3 is obtained to predict a with f , F_g , F_l , and d_i . Fig. 4.7 shows that the value predicted by Eq. 4.3 is in good agreement with the value calculated using the measured segment length, and the error between them is within 10%.

$$a = f \frac{\pi d_i^2}{F_g + F_l} \quad (4.3)$$

Define:

$$a_{Fu} = \frac{\pi d_i^2}{F_g + F_l} \quad (4.4)$$

Thus, Eq. 4.3 can be expressed as

$$a = f a_{Fu} \quad (4.5)$$

where a_{Fu} is the fundamental specific surface area between two adjacent segments, and it is determined by the total flow rate of the fluid and the microchannel diameter. The number of segments is proportional to the valve frequency, a , is therefore the product of f and a_{Fu} .

4. Mass Transfer Measurement in Length-controlled Segmented Flow

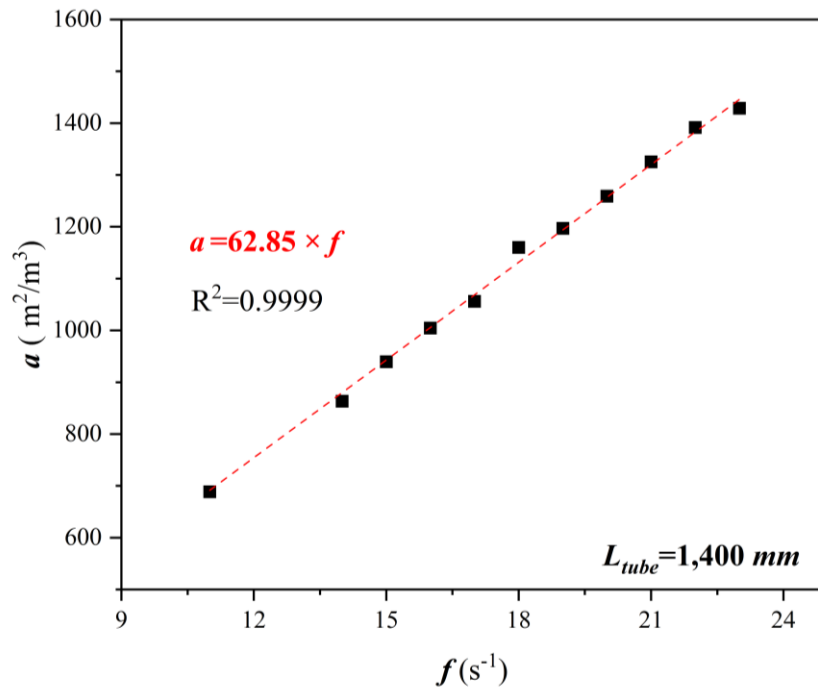


Fig. 4.6 Influence of valve frequency on a

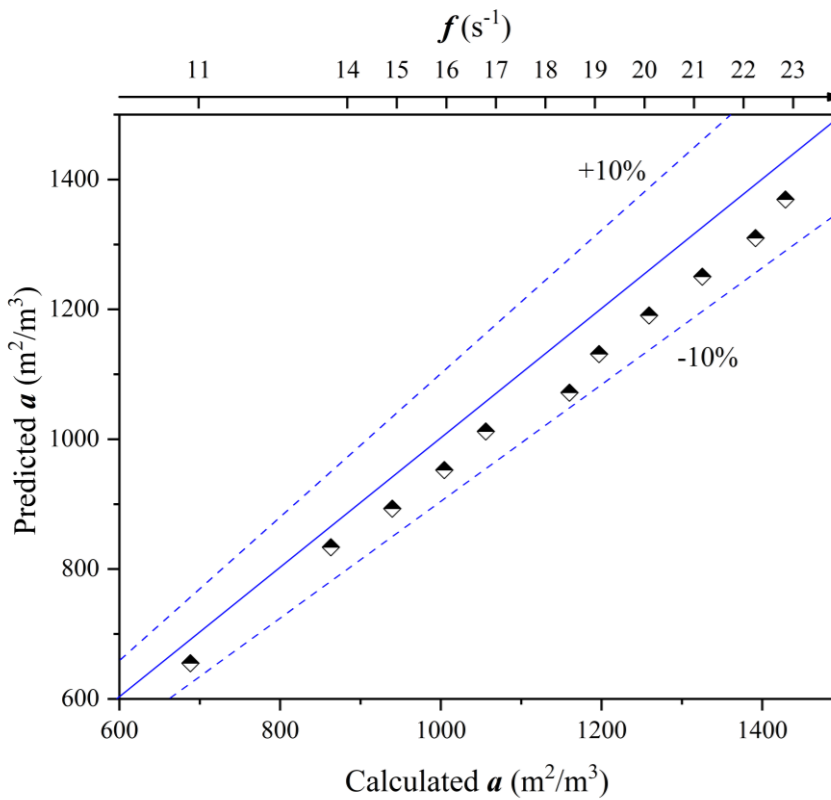


Fig. 4.7 Performance of the correlation for predicting a

4. Mass Transfer Measurement in Length-controlled Segmented Flow

After determining $[k_L a]_s$ and a at each valve frequency, the corresponding instinct liquid side mass transfer coefficient $[k_L]_s$ can be obtained. Fig. 4.8 depicts that $[k_L]_s$ can be viewed as a constant despite the increase in f . Therefore, a is the most significant contributing factor to the growth of $[k_L a]_s$.

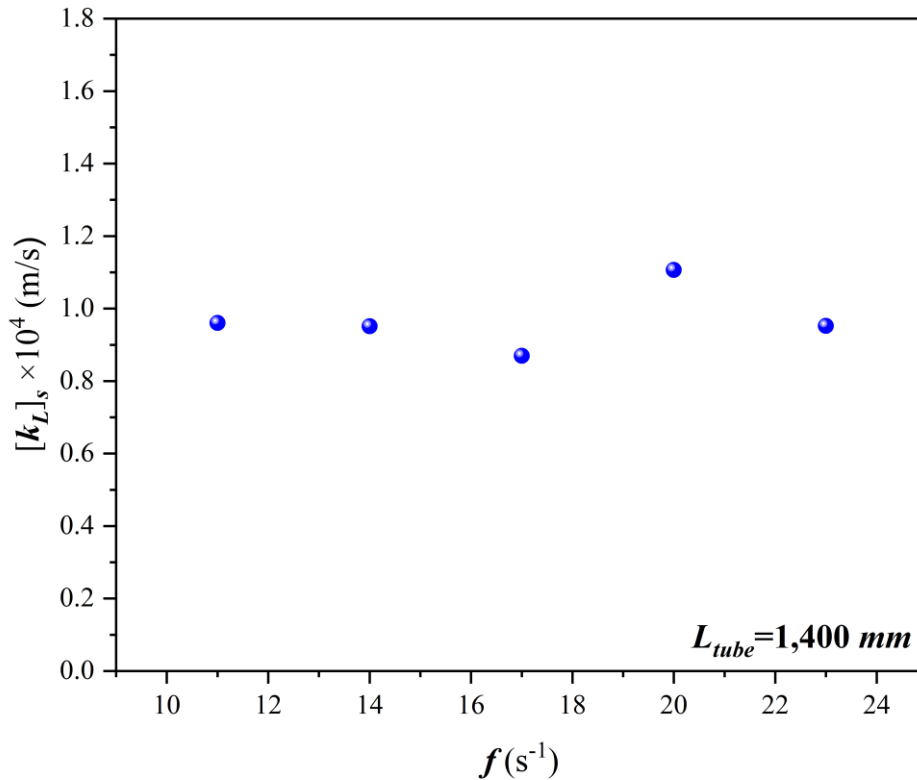


Fig. 4.8 Influence of valve frequency on $[k_L]_s$

Finally, $[k_L a]_s$ can be expressed by Eq. 4.6, the only variable in this equation is f for a specific system with a constant flow rate. Essentially, the volumetric mass transfer coefficient can be controlled intentionally by altering the valve frequency without changing the other parameters. By contrast, previous studies had to change the flow rate, pressure, or channel diameter to alter the mass transfer coefficient.

$$[k_L a]_s = f \frac{\pi a_i^2}{F_g + F_l} [k_L]_s \quad (4.6)$$

4. Mass Transfer Measurement in Length-controlled Segmented Flow

Table 4.1 presents a comparison of the k_{La} and k_L values in this study with data reported in the literature. Apparently, the k_{La} in microchannels is hundreds of times than that in batch operation; the k_{La} of this study is in the same order but smaller than that in some reports, which should be attributed to the scale effect of the channel geometry. Simultaneously, k_L in this study is in good agreement with the literature that uses the same fluids.

Table 4.1 Comparison of k_{La} and k_L with literature

Phases	Channel size (mm)	Flow rate (mL/min)	k_{La} (s ⁻¹)	k_L ($\times 10^{-4}$ m \cdot s ⁻¹)	Reference
Air–Water	$d_i = 1.59$	$F_g = F_l = 2.0$	0.07–0.15	0.86–1.1	This study
Air–Water	Batch Reactor	—	$(0.56–1.67) \times 10^{-4}$	—	[108]
Air–Glucose/KOH	0.50×0.50	$F_g = 0.6–1.2,$ $F_l = 2.4–4.0$	3.58–17.1	3.87–40.4	[109]
O ₃ /O ₂ –Water	0.40×0.50	$F_g = 0.1–2.1,$ $F_l = 0.02–0.1$	0.5–7.5	0.5–7.5	[57]
CO ₂ –NaOH	0.60×0.30	$F_g = 0.2–3.2,$ $F_l = 0.1–1.2$	0.06–0.2	0.2–0.8	[55]
CO ₂ –Water	0.60×0.30	$F_g = 2.5–4.5,$ $F_l = 1.0–1.25$	1.0–2.0	2.0–3.0	[110]
CO ₂ /N ₂ –NaOH	0.50×0.40	$F_g = 0.05–0.2,$ $F_l = 0.04–0.06$	—	1.0–6.0	[111]
CO ₂ –MEA/DEEA	0.40×0.40	$F_g = 0.16–10.83,$ $F_l = 0.33–1.67$	2.0–11.0	4.0–17.0	[112]

4.5 Conclusion

This chapter investigated the influence of segment length on mass transfer performance in gas–liquid segmented flows. By installing a high-speed valve in the gas tube, the air–water segment length was successfully manipulated by altering the valve frequency without changing the fluid flow rate. Mass transfer measurements were performed in a flask with a valve frequency of 8 to 23 s⁻¹, when the flow rate of both phases was 4.0 mL/min. $[k_{LA}]_{overall}$ and $[k_{LA}]_b$ was determined for the different configurations to calculate the $[k_{LA}]_s$ in segmented flow. These results revealed that $[k_{LA}]_s$ is proportional to f before the liquid phase becomes saturated with oxygen. Meanwhile, the specific areas a and $[k_{LA}]_s$ can be predicted accurately by using the correlations derived from the valve frequency, fluid flow rate, and microchannel diameter.

Part II

Continuous Synthesis of Size-controlled Fe₃O₄ Nanoparticles in Segmented Flow

5

Continuous Synthesis of Size-controlled NanoFe₃O₄ by Coprecipitation

This chapter endeavors to offer a practical solution to address the mentioned challenges in nanoFe₃O₄ synthesis by capitalizing on the benefits of segmented flow. We centered our research on the continuous synthesis of nanoFe₃O₄ in a gas-liquid segmented flow, focusing on nanoparticle size regulation by altering segment length using a high-speed valve without the need to change the residence time of fluids. It is expected to offer a high throughput approach for the continuous synthesis of nanoFe₃O₄ and serve as a noteworthy application of segmented flow for precise synthesis in microreactors.

5.1 Experimental

5.1.1 Experimental setup

The experimental setup is illustrated in Fig. 5.1(a). The experimental apparatus is divided into two primary sections: the segmented flow generation section before the polypropylene (PP) T-junction 2 (OD 1.6 mm, ID 1.1 mm) and the synthesis section downstream.

In the segmented flow generation section, ferro ion solvent and nitrogen intersect at T-junction 1 (OD 1.6 mm, ID 1.1 mm), forming a segmented flow in the outlet PFA

5. Continuous Synthesis of Size-controlled NanoFe₃O₄ by Coprecipitation

channel (OD 3.17 mm, ID 1.59 mm). The liquid flow rate was regulated by a diaphragm pump (QI-100-VF-P-S, Tacmina), while the gas flow rate was managed with a mass flow controller (FCST1005LC-4F2-F10, Fujikin). A high-speed valve (ALD3, Swagelok) was installed at the outlet of the mass flow controller, driven by compressed air supplied by a compressor. The valve, linked to a single-board computer (Raspberry Pi 4), received signals to open or close. With an open/close time of 5 ms, this valve enabled rapid switching of gas flow, consequently altering the segment length.

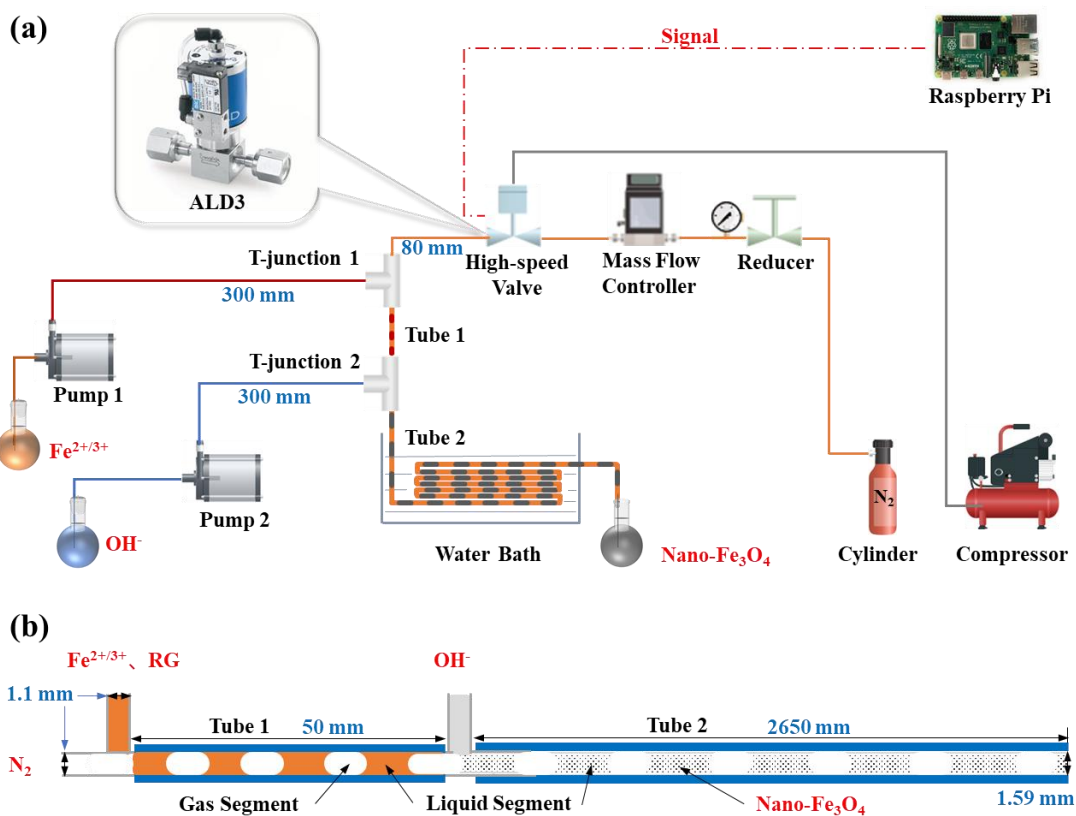


Fig. 5.1 Schematic of the experimental setup

At T-junction 2, the liquid segment generated at T-junction 1 is combined with an aqueous alkali and injected by another diaphragm pump (QI-100-VF-P-S, Tacmina). The target reaction occurs immediately within the extended liquid segment, as depicted in Fig. 5.1(b). The outlet PFA tube (2650 mm) ensures adequate residence time for the

5. Continuous Synthesis of Size-controlled NanoFe₃O₄ by Coprecipitation

coprecipitation process. Images of the final segments containing reaction products were captured using a high-speed camera (BU602MCF, Toshiba) and a microscope (STZ-161-TLED-HZ, Shimadzu) positioned at the outlet of the PFA tube. Moreover, a water bath (T-22LA, Thomas) was used to maintain the necessary reaction temperature. Placing the two T-junctions and their inlet tubes within the bath prevents temperature reduction in T-junction 2 when the two solvents mix.

5.1.2 Chemicals

Ferrous chloride tetrahydrate (FeCl₂·4H₂O) was purchased from Sigma-Aldrich Co., Ltd, ferric chloride hexahydrate (FeCl₃·6H₂O, 99.0 %), sodium hydroxide (NaOH, 98.0 %), ethylene glycol (EG, 99.5 %), and ethanol (99.5 %) were purchased from Fujifilm Wako Pure Chemical Corporation. The solutions used in this study were prepared with the corresponding components and distilled water.

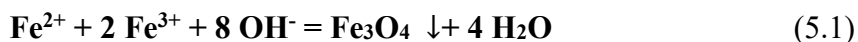
5.1.3 Strategy for continuous operation

Two solutions are required to implement the continuous synthesis of nanoFe₃O₄ using the microfluidic system shown in Fig. 5.1(a). The first solution contains Fe²⁺, Fe³⁺, and the nucleating agent ethylene glycol, which is in an equal volume of the solvent water, and the second solution contains OH⁻.

In an experiment in this study, the first solution is prepared by dissolving 0.49 g FeCl₂·4H₂O and 1.0 g FeCl₃·6H₂O into 30 mL of distilled water and 30 mL of ethylene glycol, forming a mixture with a Fe²⁺/ Fe³⁺ molar ratio of 1:1.5; the second solution is prepared by dissolving 0.836 g NaOH into 60 mL of distilled water. Afterward, the first solution is pumped into one of the inlets of T-junction 1; it encounters nitrogen in the center of T-junction 1 and forms a gas–liquid segmented flow in the outlet channel of T-

5. Continuous Synthesis of Size-controlled NanoFe₃O₄ by Coprecipitation

junction 1. When the segmented flow enters T-junction 2, the liquid segments will mix with a drop of NaOH solution, which is pumped in from another inlet of T-junction 2. The reaction of two solutions (Eq. 5.1) takes place in the lengthened liquid segment, as illustrated in Fig. 5.1(b). The two solutions are pumped into T-junctions with the same flow rate to ensure that the molar ratio of Fe²⁺, Fe³⁺, and OH⁻ is 1:1.5:8.5. By optimizing the reaction parameters (temperature, Fe²⁺/Fe³⁺ ratio, valve frequency, etc.), magnetic nanoFe₃O₄ particles will be released in the liquid segments and can be separated easily from the reacted solution collected in the outlet of the microchannel. The obtained particles are washed and ultrasonically dispersed (15 min) with ethanol 3 times and then dried in an oven at 90 °C for 12 h.



5.2 Continuous synthesis of nanoFe₃O₄

In the standard batch synthesis of nanoFe₃O₄, the reaction temperature was 50 °C [91,113]. While the Fe²⁺:Fe³⁺ ratio in Eq. (5.1) is 1:2, considering the partial oxidation of Fe²⁺ to Fe³⁺ due to the solution's exposure to air during the batch method, the Fe²⁺:Fe³⁺ ratio was generally below 1:2 in batch methods. The coprecipitation synthesis parameters for nanoFe₃O₄ were confirmed with a batch reaction at 50 °C in a flask. This was achieved by adding a NaOH solution (0.1 mol/L) at a flow rate of 2.0 mL/min into 100.0 mL of an iron solution (0.05 mol/L, Fe²⁺:Fe³⁺ = 1:1.5) in a flask, stirring vigorously until the pH reached 11.0. This process, which lasted 2 h, resulted in the solution changing to a black color. As displayed in Fig. 5.2(a), the product showcased a distinct magnetic response. Fig. 5.2(b) (Batch) exhibits the XRD pattern of the powder. This pattern demonstrates that the product crystallized in a single phase, with noticeable peaks identified at 2θ values of 30.2°, 35.6°, 43.3°, 53.7°, 57.3°, and 62.9°. These findings align with the

5. Continuous Synthesis of Size-controlled NanoFe₃O₄ by Coprecipitation

standard card for Fe₃O₄.

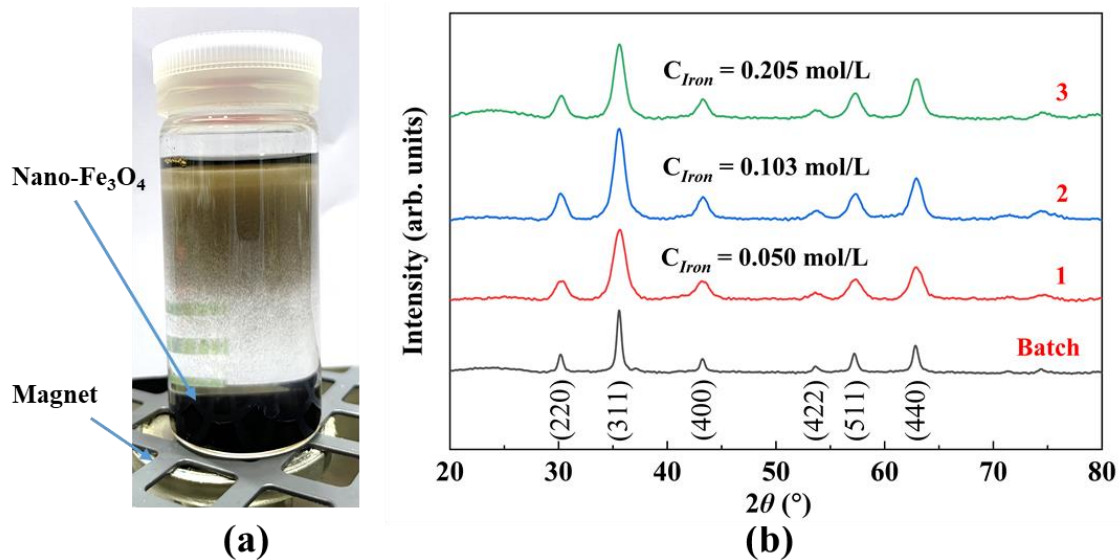


Fig. 5.2 (a) Image of nanoFe₃O₄; (b) XRD patterns of nanoFe₃O₄ synthesized by the batch method and segmented flow with conditions (1)-(3) in Table 5.1

To facilitate this coprecipitation reaction continuously in the microchannel utilizing the set-up illustrated in Fig. 5.1 (a), an iron solution (0.05 mol/L, Fe²⁺:Fe³⁺ = 1:1.5) was propelled by pump 1 at a flow rate of 3.0 mL/min. Concurrently, a NaOH solution was circulated by pump 2 at an equivalent flow rate. The NaOH concentration was maintained at 0.081 mol/L to ensure that the final pH of the mixed solution approached 11.0. The nitrogen was introduced at the inlet of T-junction 1 at a flow rate of 5.0 mL/min to ensure a similar segment length in the outlet channel of T-junction 2.

Based on the equations (Eq. 3.6 and Eq. 2.3) formulated (predicated on mass balance) in chapter 2 and 3 for predicting segment length, the nitrogen segment length approximated 3.22 mm, while the liquid segment lengths at the outlets of T-junction 1 and 2 were 1.89 mm and 3.78 mm, respectively. The product procured at the outlet of the microchannel resembled the product generated through the batch method. The XRD

5. Continuous Synthesis of Size-controlled NanoFe₃O₄ by Coprecipitation

pattern (Fig. 5.2(b), 1) showcased the same principal peaks as those observed in the batch product.

Table 5.1 Parameters of different experiments

NO.	Concentration, mol/L				Flow rate, mL/min			Fe ²⁺ :Fe ³⁺ :OH ⁻	Velocity, mm/s	
	Fe ²⁺	Fe ³⁺	Total	OH ⁻	Iron	NaOH	N ₂		Tube 1	Tube 2
1	0.020	0.030	0.050	0.017	3.0	3.0	5.0	1:1.5:8.5	67.2	92.4
2	0.041	0.062	0.103	0.349	3.0	3.0	5.0	1:1.5:8.5	67.2	92.4
3	0.082	0.123	0.205	0.697	3.0	3.0	5.0	1:1.5:8.5	67.2	92.4
4	0.041	0.045	0.086	0.33	3.0	3.17	5.0	1:1.1:8.5	67.2	93.8
5	0.041	0.053	0.094	0.33	3.0	3.17	5.0	1:1.3:8.5	67.2	93.8
6	0.041	0.062	0.103	0.33	3.0	3.17	5.0	1:1.5:8.5	67.2	93.8
7	0.041	0.070	0.111	0.33	3.0	3.17	5.0	1:1.7:8.5	67.2	93.8
8	0.041	0.078	0.119	0.33	3.0	3.17	5.0	1:1.9:8.5	67.2	93.8
9	0.082	0.139	0.221	0.697	3.0	3.0	5.0	1:1.7:8.5	67.2	92.4

Throughout the continuous synthesis process, we observed immediate particle generation within the liquid segments, starting from the outlet of T-junction 2. This suggests that the coprecipitation reaction commences instantly once the two solutions intersect in T-junction 2. Given the total flow rate and the segment length, the reaction time was less than 0.1 s. For 100 mL of iron solution, the overall operation duration amounted to 25 min. This is merely 20.8 % of the reaction time required by the batch method. However, the iron concentration was relatively low. The reaction efficiency could potentially be improved by increasing this concentration.

5.3 Influence of iron concentration on nanoFe₃O₄ synthesis

The experiments were conducted under conditions (1), (2), and (3), as outlined in Table 5.1, at 50 °C, to examine the effects of iron (Fe²⁺ and Fe³⁺) concentration on the continuous nanoFe₃O₄ synthesis. Fig. 5.3 illustrates the segmented flow state in the outlet microchannel at varying iron concentrations. Fig. 5.3 reveals that the formed nanoparticles remain suspended within the liquid segments, aided by the inner circulation of these segments. At an iron concentration of 0.050 mol/L, the nanoparticles occupied a fraction of the liquid segment. However, as the concentration doubled, nearly half of the liquid segment became populated with nanoparticles. Moreover, when the iron concentration escalated to 0.205 mol/L, the liquid segment was nearly saturated with nanoparticles. Given that the flow rate of the iron solution remains constant at 3.0 mL/min, a fourfold increase in the iron concentration results in an approximately fourfold productivity increase.

Figures 5.2(b), (1), (2), and (3) display the XRD patterns of the particles produced at varying iron concentrations. The diffraction patterns across all three products display peaks at $2\theta = 30.2^\circ, 35.6^\circ, 43.3^\circ, 53.7^\circ, 57.3^\circ,$ and 62.9° , indicating that the products are all Fe₃O₄. Furthermore, the negligible differences in peak intensity substantiate that the products remain identical. Eq.5.2 presents the well-known the famous Scherrer equation:

$$d = K \lambda / (\beta \cos\theta) \quad (5.2)$$

where the Scherrer constant $K=0.89$, the X-ray wavelength $\lambda=1.5406 \text{ \AA}$, β represents the full width at half maximum of the peak, and θ indicates the Bragg diffraction angle [114].

After applying the Scherrer equation to calculate the crystal diameter, as Table 5.2 illustrates, the average diameter of the crystals increases by approximately 1 nm while the iron concentration quadruples. Moreover, the diameter of the crystals synthesized in segmented flow is less than 50 % of those obtained via the batch method. Therefore, these findings suggest that increasing the iron concentration can enhance productivity without

5. Continuous Synthesis of Size-controlled NanoFe₃O₄ by Coprecipitation

compromising product quality.

Table 5.2 Crystal size of samples in Fig. 5.2(b) determined using the Scherrer equation

2θ (°)	BATCH		1		2		3	
	β	d_p (nm)	β	d_p (nm)	β	d_p (nm)	β	d_p (nm)
30.2	0.57	14.55	1.24	6.62	1.09	7.56	1.09	7.58
35.6	0.59	14.20	1.45	5.77	1.32	6.31	1.25	6.69
43.3	0.59	14.39	1.70	5.04	1.32	6.49	1.21	7.05
53.7	0.60	14.83	1.33	6.69	1.30	6.82	1.15	7.74
57.3	0.65	13.97	1.51	6.00	1.43	6.35	1.34	6.77
62.9	0.68	13.66	1.46	6.36	1.36	6.83	1.32	7.05
Average		14.27		6.08		6.73		7.15

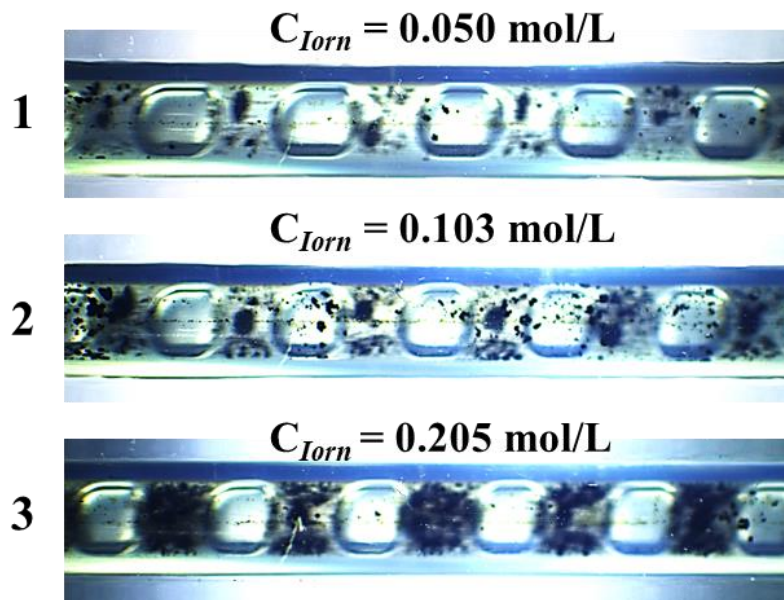


Fig. 5.3 NanoFe₃O₄ products in the microchannel at different iron concentrations

5. Continuous Synthesis of Size-controlled NanoFe₃O₄ by Coprecipitation

Nevertheless, over extended operational times, particles tend to accumulate on the tube wall, as depicted in the second image of Fig. 5.3 above the elliptical gas segments. This deposited sediment can be effectively eliminated by increasing the gas flow rate. However, the particles redeposit if their concentration remains substantially high, as demonstrated in the third image of Fig. 5.3. Possible strategies to mitigate this phenomenon involve increasing the segmented flow rate or employing a tube with a smoother surface.

5.4 Influence of temperature on nanoFe₃O₄ synthesis

The batch method of synthesizing nanoFe₃O₄ by coprecipitation typically employs temperatures within the range of 30–80 °C. As highlighted in Sections 5.2 and 5.3, this facilitates the continuous synthesis of nanoFe₃O₄ in the microchannel at 50 °C.

To examine the feasibility of producing nanoFe₃O₄ at lower temperatures, the continuous synthesis procedure was conducted at 20, 30, 40, and 50 °C, adhering to condition (4) in Table 5.1. At 20 °C, the procured product demonstrated no magnetic properties and took the form of hydroxide flocculents. In contrast, at temperatures of 30, 40, and 50 °C, the magnetic particles could be magnetically separated from the product. However, hydroxide flocculents remained in the solution for the products obtained at 30 and 40 °C. Moreover, the product derived at 50 °C showed no visible presence of hydroxide flocculents, and all the particles displayed magnetic characteristics.

5. Continuous Synthesis of Size-controlled NanoFe₃O₄ by Coprecipitation

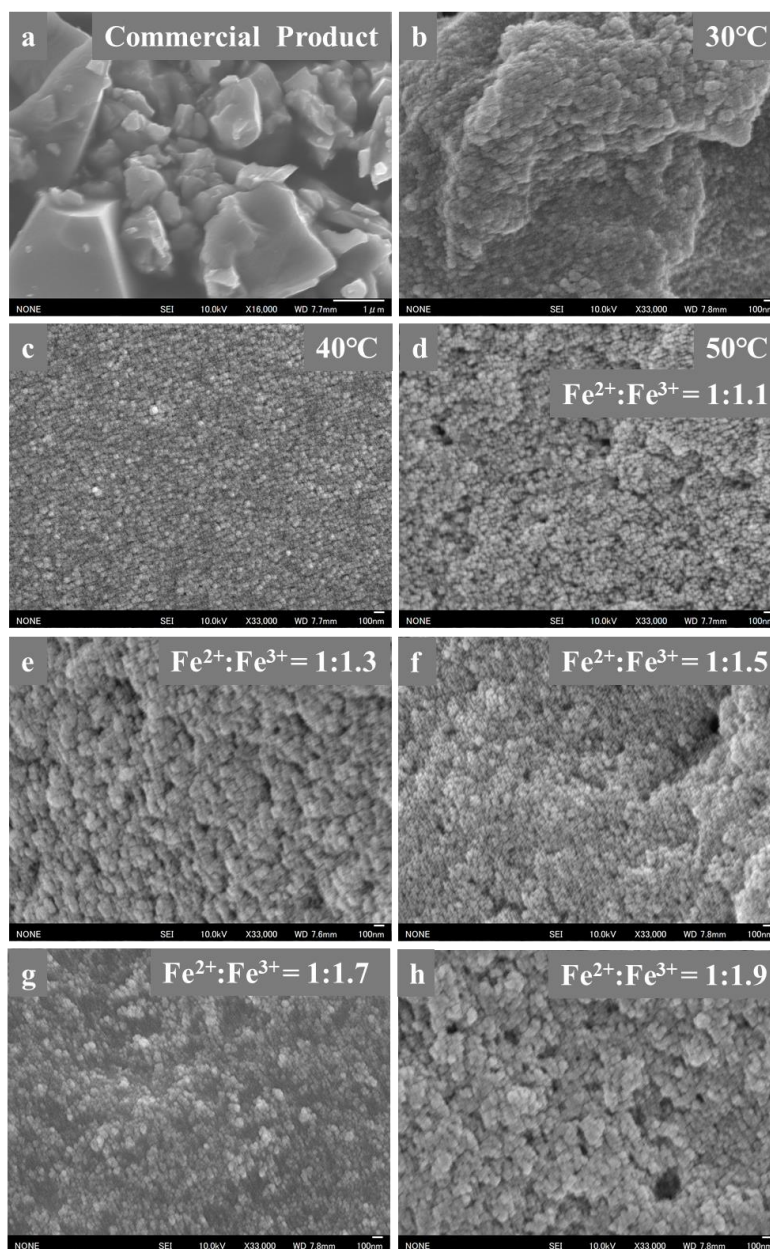


Fig. 5.4 SEM micrographs of Fe₃O₄

Figures 5.4(b)-(d) present the SEM images of the separated products obtained at temperatures of 30, 40, and 50 °C. In comparison to the commercial product (Fig. 5.4(a)), which is of microscale order, all three products exist on a nanoscale. The boundary of the product obtained at 30 °C appeared indistinct, suggesting an amorphous state. However, the products procured at 40 and 50 °C exhibit a uniformly spherical crystalline structure.

5. Continuous Synthesis of Size-controlled nanoFe₃O₄ by Coprecipitation

While the product generated at 50 °C showed a slight agglomeration, no byproducts were observed in the initially collected material. Therefore, 50 °C is deemed the optimal temperature for the continuous synthesis of nanoFe₃O₄ via coprecipitation in microchannels.

5.5 Influence of Fe²⁺:Fe³⁺ ratio on nanoFe₃O₄ synthesis

During the batch synthesis of nanoFe₃O₄, the solution was stirred for approximately 2 h, which caused a portion of Fe²⁺ to oxidize to Fe³⁺. However, in the continuous strategy, the coprecipitation reaction occurred in the liquid segment, with each liquid separated by a nitrogen segment. This creates a microreactor in the liquid segment, with both sides of nitrogen gas providing an inert environment. Therefore, after the segmentation flow was formed in the microchannel, no oxygen could transfer into the liquid segment. In this research, the Fe²⁺:Fe³⁺ ratio in the initial reactant should differ from that in the batch method, with it being closer to 1:2.

We conducted experiments altering the concentration of Fe³⁺ using the parameters outlined in conditions (4)-(8) in Table 5.1 to investigate the influence of Fe²⁺:Fe³⁺ ratio on nanoFe₃O₄ synthesis. The SEM images of the corresponding products are shown in Figs. 5.4(d)-(h). The results indicate that the particle boundaries first became distinct with an increase in the Fe²⁺:Fe³⁺ ratio from 1:1.1 to 1:1.7 and became indistinct as the ratio increased to 1:1.9. At a Fe²⁺:Fe³⁺ ratio of 1:1.7, the particles demonstrated high crystallinity and distinct spherical shape. Therefore, the optimal Fe²⁺:Fe³⁺ ratio for this continuous method was approximately 1:1.7. Additionally, approximately 10 % of Fe²⁺ oxidized to Fe³⁺ in the reactant solution. Given that no oxygen was introduced in the microchannel, this oxidation was primarily attributed to the air exposure of the reactant during the solution preparation process. This was further facilitated by the dissolved oxygen in the water used as a solvent. Solution preparation was performed at room

5. Continuous Synthesis of Size-controlled NanoFe₃O₄ by Coprecipitation

temperature (25 °C), where the saturated oxygen concentration in water was approximately 8.25 mg/L. According to Eq. (5.3), assuming a complete reaction of dissolved oxygen with Fe²⁺, this could reduce the concentration by 0.001031 mol/L, approximately 2.5 % of the initial Fe²⁺ concentration. This brief calculation supports our hypothesis.



5.6 Influence of valve frequency on nanoFe₃O₄ size

In chapter 3, we successfully manipulated the segment length by altering the frequency of the high-speed valve installed at the outlet tube of the gas phase. We observed that the segment length of the liquid and gas phases was inversely proportional to the valve frequency, modifying the volume of each segment. For this continuous synthesis reaction using segmented flow, a decrease in segment length results in fewer reactants in each liquid segment, promoting a more thorough mixture within the segment. This facilitates the mass transfer process of the coprecipitation reaction, potentially influencing the final nanoparticle size.

To validate this theory, we synthesized nanoFe₃O₄ using the parameters listed in condition 9 of Table 5.1, with valve frequencies of 8, 11, 14 and 17 s⁻¹ (corresponding to liquid segment lengths of 6.3 mm, 4.6 mm, 3.6 mm, and 3.0 mm, respectively, post-T-junction 2), while maintaining constant fluid flow rates. The operation of the high-speed valve facilitated the distribution of a volume of reactant (equivalent to the total flow rate of the liquid phases per second) into several microreactors, the number of which was determined by valve frequency. The TEM images and the corresponding average particle diameter of nanoFe₃O₄, obtained at different valve frequencies, are presented in Fig. 5.5.

5. Continuous Synthesis of Size-controlled $\text{NanoFe}_3\text{O}_4$ by Coprecipitation

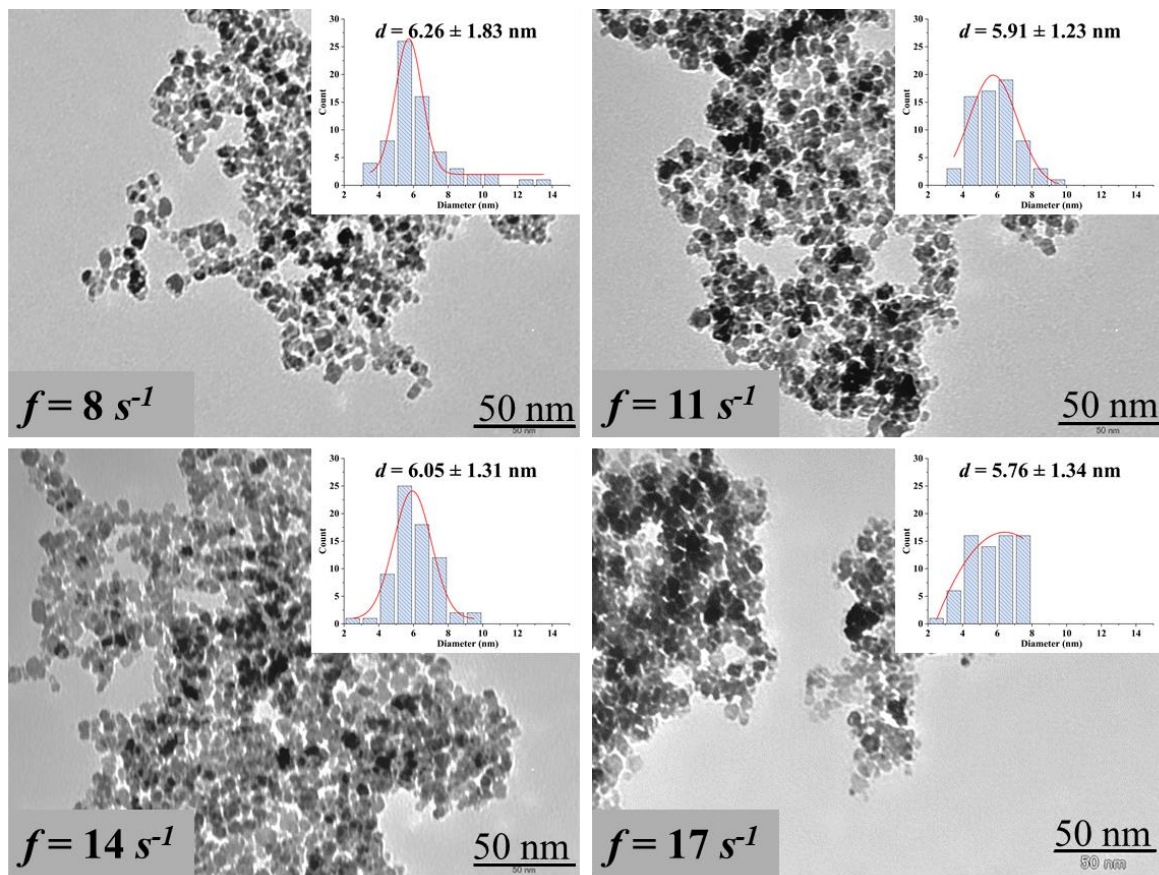


Fig. 5.5 TEM images and average diameters of nano Fe_3O_4 synthesis at different valve frequencies

Overall, the results showed that the average diameters of all the products were less than 10 nm. Moreover, the particles depicted in the TEM images were nearly identical. Statistical analysis indicated that the particle diameters are $<7 \text{ nm}$, which aligned well with the crystal diameter calculated using the Scherrer equation and confirms that the nanoparticles obtained are predominantly primary particles.

When the valve frequency was relatively low, specifically 8 s^{-1} , the average diameter and deviation ($6.26 \pm 1.83 \text{ nm}$) were the highest. Conversely, the smallest average diameter of nano Fe_3O_4 ($5.76 \pm 1.34 \text{ nm}$) was achieved when the valve frequency was 17 s^{-1} . As the valve frequency increased from 8 to 17 s^{-1} , the maximum particle size recorded

5. Continuous Synthesis of Size-controlled NanoFe₃O₄ by Coprecipitation

decreased from 13.5 to 7.5 nm, leading to a narrower particle size distribution. Additionally, a few nanoparticles of approximately 2 nm in size were produced.

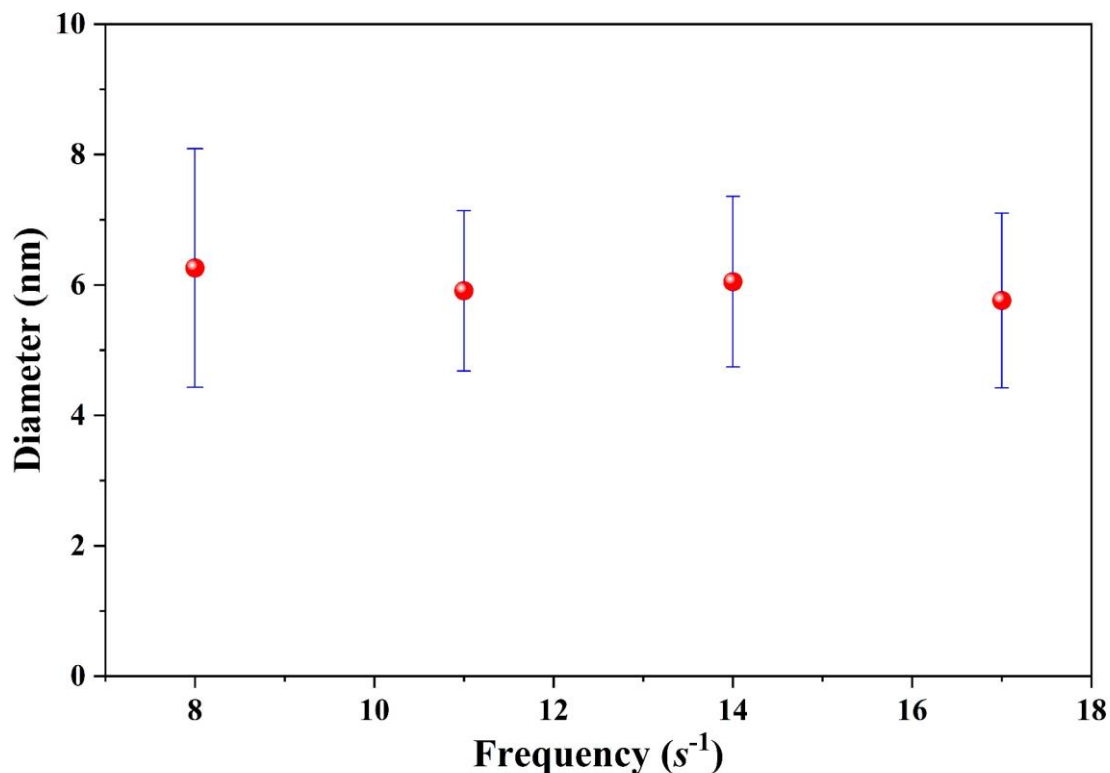


Fig. 5.6 Influence of valve frequency on nanoFe₃O₄ size

Upon plotting the average particle size and corresponding deviation against the valve frequency in Fig. 5.6, we observed that the smallest particle size was achieved at a valve frequency of 17 s^{-1} , but the length of the error bar increased with higher frequencies. These results suggested that a higher valve frequency or shorter segment length facilitated the consistent and precise synthesis of nanoFe₃O₄ particles, resulting in small and uniform sizes. To achieve a small nanoparticle size with a narrow distribution, a valve frequency higher than 11 s^{-1} is required.

5.7 Principle of coprecipitation in segmented flow

To better understand the advantages of this segmented flow synthesis strategy, Fig. 5.7 illustrates the principles of the coprecipitation reaction in the batch reactor and the segmented flow system.

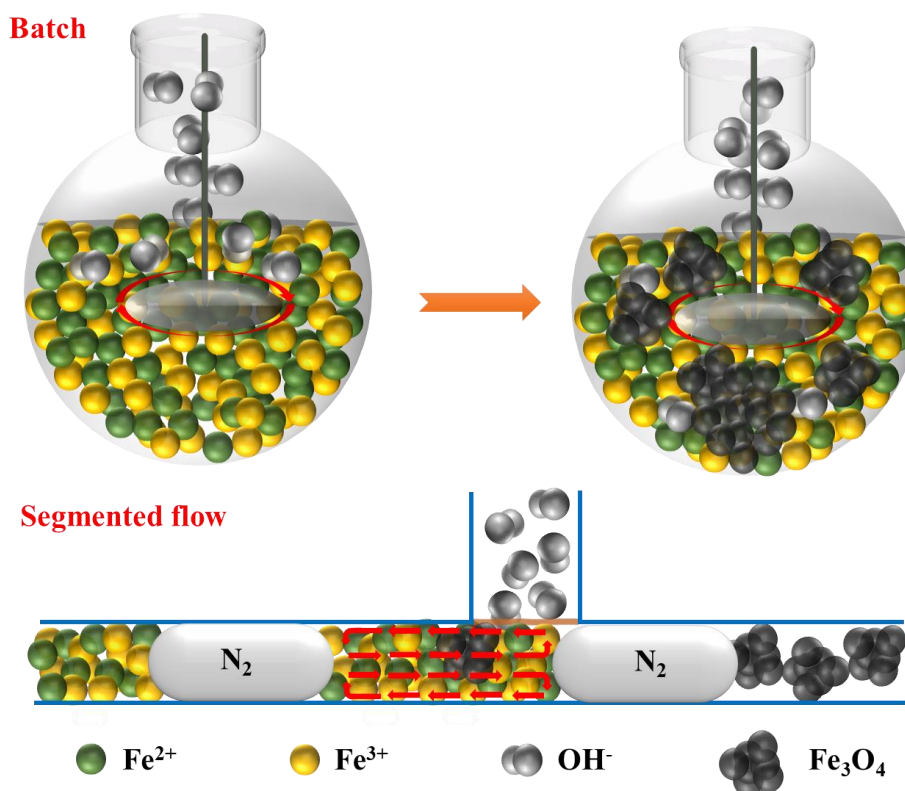


Fig. 5.7. Principles of coprecipitation in a batch reactor and segmented flow

In the batch reactor, the NaOH solution is gradually added to the iron solution (containing Fe²⁺ and Fe³⁺). The reaction is not complete until the pH of the mixture reaches 11.0. The mixture is stirred to promote ion dispersion. However, achieving perfect uniformity in such a large volume is challenging. When OH⁻ ions mix with Fe²⁺ and Fe³⁺, the reaction in Eq. 5.1 immediately commences, forming nanoFe₃O₄ crystal nuclei. Following this nucleation stage, further nanoFe₃O₄ growth occurs in the presence of

5. Continuous Synthesis of Size-controlled NanoFe₃O₄ by Coprecipitation

additional OH⁻ ions in proximity. Consequently, nanoparticles obtained in the batch reactor are relatively larger and exhibit a broad size distribution unless the NaOH feed amount is minimal.

When utilizing the segmented flow strategy, each liquid segment functions as a small reactor with a volume of approximately 0.01 mL. Before reaching T-junction 2, robust internal circulation within the liquid segment leads to the homogeneous dispersion of Fe²⁺, Fe³⁺, and EG. Once the liquid segment reaches the NaOH solution inlet at T-junction 2, the nucleation reaction occurs at the interface of the two solutions. Simultaneously, the internal circulation within the iron solution drives the newly-formed nanoFe₃O₄ away from the NaOH solution inlet. This countermovement reduces the likelihood of the nanoFe₃O₄ contacting additional NaOH solution, preventing the growth of nanoFe₃O₄. Meanwhile, this internal circulation delivers fresh Fe²⁺ and Fe³⁺ to the NaOH solution inlet, continually consuming the OH⁻ ions. Consequently, the produced nanoFe₃O₄ rarely grows beyond the nucleation stage. This aligns with the observation that the nanoparticle sizes calculated by the Scherrer equation are similar to those measured in TEM images.

5.8 Comparison with other synthesis methods

Various continuous strategies have been developed for fabricating nanoFe₃O₄ in the aforementioned studies [101–105]. Fig. 5.8 compares their key characteristics alongside the batch method and the segmented flow synthesis process examined in this research.

Figures. 5.8 (a)-(c) compare the parameters associated with different methods. Among the four methods, our approach employs the lowest reaction temperature (50 °C), which is 10 °C lower than the microdroplet method. Moreover, the feed flow rate of this segmented flow technique is 4615 times larger than that of the microdroplet method (≈ 0.0013 mL/min). The packed bed reactor boasts the largest feed flow rate due to its greater diameter and operates at the highest reaction temperature (80 °C).

5. Continuous Synthesis of Size-controlled NanoFe₃O₄ by Coprecipitation

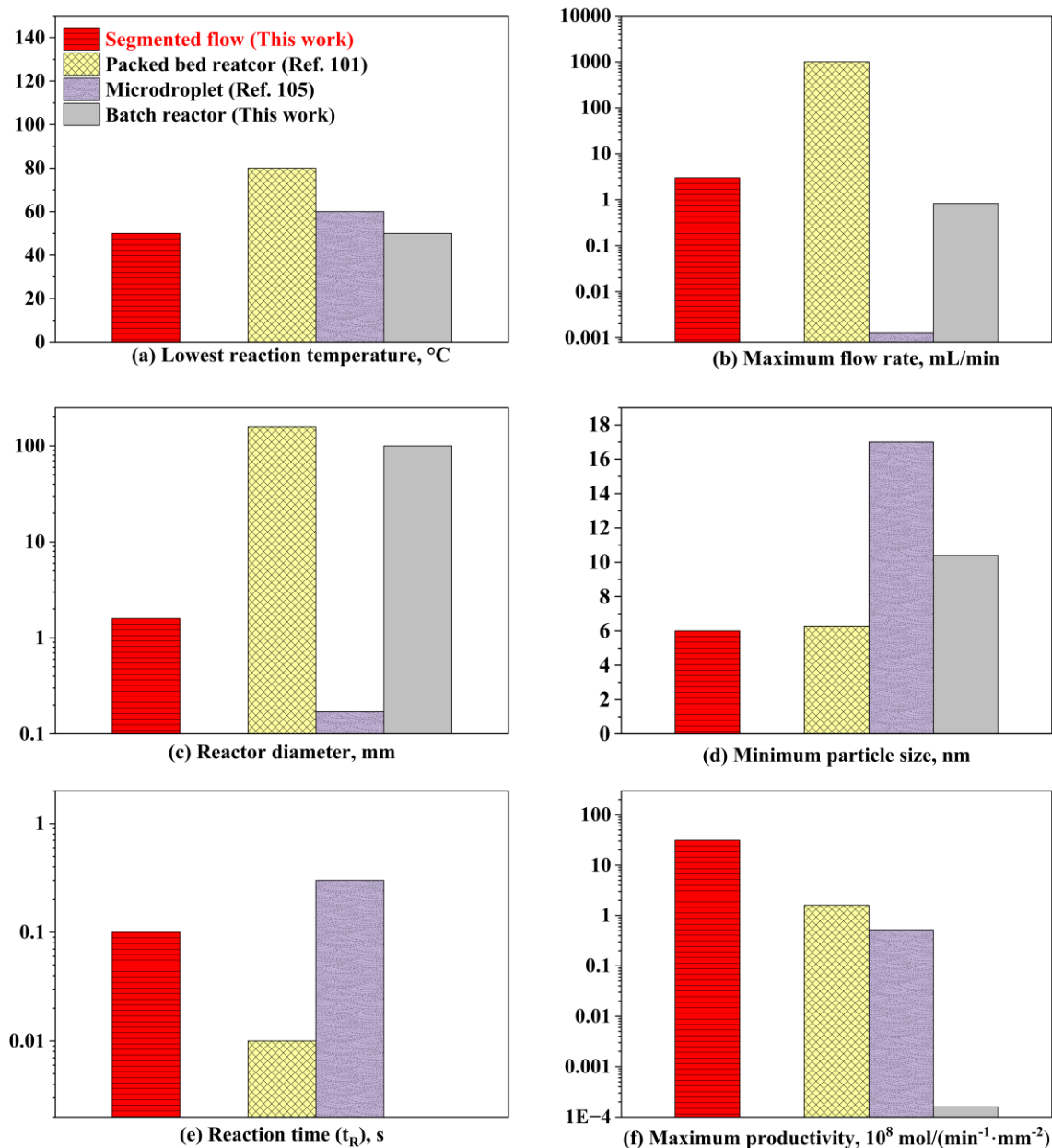


Fig. 5.8 Comparison of segmented flow synthesis with batch and other continuous methods

Figures 5.8 (d)-(f) compare the performance of the four methods. As demonstrated in Fig. 5.8(d), the segmented flow method produces the smallest nanoparticle size, slightly smaller than that of the packed bed reactor, while the microdroplet method yields

5. Continuous Synthesis of Size-controlled $\text{NanoFe}_3\text{O}_4$ by Coprecipitation

the largest. The packed bed reactor purports to complete the reaction within 0.01 s. The reaction time (t_R) of the segmented flow method is not straightforward to determine directly due to the minuscule channel size and the high fluid velocity. However, it can be approximated with a simple calculation. The inner diameter of the T-junction is 1.1 mm, and the segment velocity at the inlet of T-junction 2 is 67.2 mm/s (Table 1), meaning it takes 0.016 s for the liquid segment to traverse the inlet of the NaOH solution. As explored in Section 3.6, the coprecipitation occurs instantly when the two solutions mix. The deposition of nanoparticles at the outlet and on the outlet tube of T-junction 2 indicates a significant presence of nanoparticles in the liquid segment. Thus, we conservatively estimated that the t_R in the segmented flow method was less than 0.1 s. Given the varying reactor diameters in each method, we calculated their productivity based on the unit reactor diameter, as outlined in Table 5.3. As evident in the last column of Table 5.3, the productivity of continuous processes significantly surpasses that of the batch method. Particularly, the productivity of the segmented flow and packed bed reactor is over 10^3 times greater than that of the batch method.

In summary, the segmented flow synthesis strategy produces the smallest $\text{nanoFe}_3\text{O}_4$ particles with the highest unit productivity and the lowest temperature compared to other continuous strategies. Although the feed flow rate (based on iron solution) of the packed bed reactor is considerably higher than that of our study, its reactor diameter is a hundred times larger than the tube used in our system. Consequently, its unit productivity does not surpass ours. Moreover, the advantages of our system can be amplified by increasing the concentration of the reactants. A significant drawback of conventional systems is that the packed bed reactor needs to be rotated during the reaction to enhance the mass transfer process, an energy-consuming step. Conversely, our strategy effortlessly enhances the mass transfer process in the gas-liquid segmented flow formed by nitrogen and the reactant solution, using a simple assembly of tubes and T-junctions. The synthesis of $\text{nanoFe}_3\text{O}_4$ by the microdroplet mechanism occurs on a precisely fabricated microchip, and it can produce $\text{nanoFe}_3\text{O}_4$ of 17 nm at 60 °C. However, the microscale of the channel

5. Continuous Synthesis of Size-controlled NanoFe₃O₄ by Coprecipitation

constrains the device's throughput and results in relatively low productivity. Additionally, the cost will linearly increase for scale-up. The segmented flow device in this research employs just two PP T-junctions and less than 5 m of PFA tube, resulting in a minimal cost and straightforward operation. Therefore, the segmented flow synthesis strategy emerges as the most competitive technology for continuously synthesizing nanoFe₃O₄ and is easily scalable for industrial production.

Table 5.3 Calculation of productivity in different processes

Process	Flow rate, mL/min	C_{iron} , mol/L	n_{iron} , 10 ⁶ mol/min	Diameter, mm	Unit volume (mm ³ /mm)	Productivity, 10 ⁸ mol/(min ⁻¹ mm ⁻²)
Segmented flow	3.0	0.205	0.615	1.59	1.985	31.0
Packed bed reactor [101]	1000	0.321	321	160	20096	1.60
Microdroplet [105]	0.0013	0.09	0.000117	0.17	0.0227	0.52
Batch reactor	-	-	0.012495	100	7850	0.00016

5.9 Conclusions

In this chapter, uniform nanoFe₃O₄ particles were synthesized continuously using the coprecipitation method in a microchannel with Fe²⁺, Fe³⁺, and OH⁻. The process leveraged the enhanced mass transfer in segmented flow. By optimizing the iron concentration, reaction temperature, and Fe²⁺:Fe³⁺ ratio, this in situ strategy achieved the precise synthesis of nanoFe₃O₄ within 0.1 s at 50 °C, a process that requires hours in batch reactions. Moreover, the operation of the ALD valve can regulate the segment length, thus adjusting the mass transfer rate within the liquid segment. Consequently, the nanoparticle size can be controlled at approximately 6 nm, ensuring a narrow size distribution. The simple and practicable construction of the system presents an advantage over other continuous methods for nanoFe₃O₄ synthesis. Therefore, this segmented flow synthesis

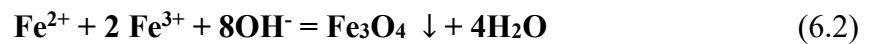
5. Continuous Synthesis of Size-controlled NanoFe₃O₄ by Coprecipitation

strategy could offer an innovative solution for the continuous industrial production of nano-Fe₃O₄. After appropriate scale-up and risk reduction of blockage, this method could revolutionize the nanoFe₃O₄ synthesis process on a large scale.

6

Continuous Synthesis of NanoFe₃O₄ by Partial Oxidation Coprecipitation

In chapter 5, we successfully achieved the continuous synthesis of Fe₃O₄ nanoparticles within a gas-liquid segmented flow system. However, it's important to note that the reaction primarily takes place in the liquid phase, and the nitrogen gas does not directly contribute to the reaction. In contrast, in the batch method, the function of the nitrogen gas is to prevent the oxidation of Fe²⁺ by the oxygen in the air, as depicted in Equation 6.1. Given that the oxidation product also serves as a reactant in the coprecipitation reaction (as indicated in Equation 6.2), we are left to contemplate the feasibility of synthesizing Fe₃O₄ nanoparticles from Fe²⁺ through a partially oxidation coprecipitation process.



In this chapter, we implemented a partial oxidation strategy utilizing air as the gas phase and Fe²⁺ as the source of iron. Through the meticulous optimization of reaction parameters, we successfully attained the continuous synthesis of Fe₃O₄ nanoparticles within an air-liquid segmented system. The liquid segment behaves as a small reactor where coprecipitation occurs, and strong recirculation inside the segment was expected

6. Continuous Synthesis of NanoFe₃O₄ by Partial Oxidation Coprecipitation

to facilitate the formation of smaller nanoparticles and reduce the risk of clogging in the microchannel. Moreover, the Fe³⁺ necessary for the coprecipitation reaction was derived from the partial oxidation of Fe²⁺ with oxygen provided by air, which was used to generate the gas segment. Notably, in this continuous strategy, oxygen is no longer a limitation that should be avoided as it participates in the process as a reactant.

6.1 Experimental

6.1.1 Experimental setup

Figure 6.1(a) shows a schematic of the experimental setup, which includes two sections: a segmented flow generation and partial oxidation section before T-junction 2 (OD = 1.6 mm, ID = 1.1 mm) and a reaction section after this junction.

In the first section, the ferrous ion (Fe²⁺) solution and air intersect in T-junction 1 (OD 1.6 mm, ID 1.1 mm) and form the segmented flow in the outlet perfluoroalkoxy alkane (PFA) tube (OD 3.17 mm, ID 1.59 mm). A diaphragm pump (QI-100-VF-P-S, Tacmina) and mass flow controller (FCST1005LC-4F2-F10, Fujikin) control the liquid and gas flow rates, respectively.

In T-junction 2, the liquid segment generated at the outlet of T-junction 1 is mixed with aqueous alkali injected by another diaphragm pump (QI-100-VF-P-S, Tacmina). Notably, the Fe²⁺ ions in the initial liquid feed are partially oxidized into Fe³⁺ ions by the oxygen in the segmented flow between the two junctions. Thus, the liquid segment contains both Fe²⁺ and Fe³⁺ ions before entering T-junction 2, where the coprecipitation reaction of Fe²⁺, Fe³⁺, and OH⁻ takes place in the lengthened liquid segment to form Fe₃O₄ (Fig. 6.1(b)). Meanwhile, the outlet PFA (210 cm) tube provides sufficient residence time for the coprecipitation process.

6. Continuous Synthesis of NanoFe₃O₄ by Partial Oxidation Coprecipitation

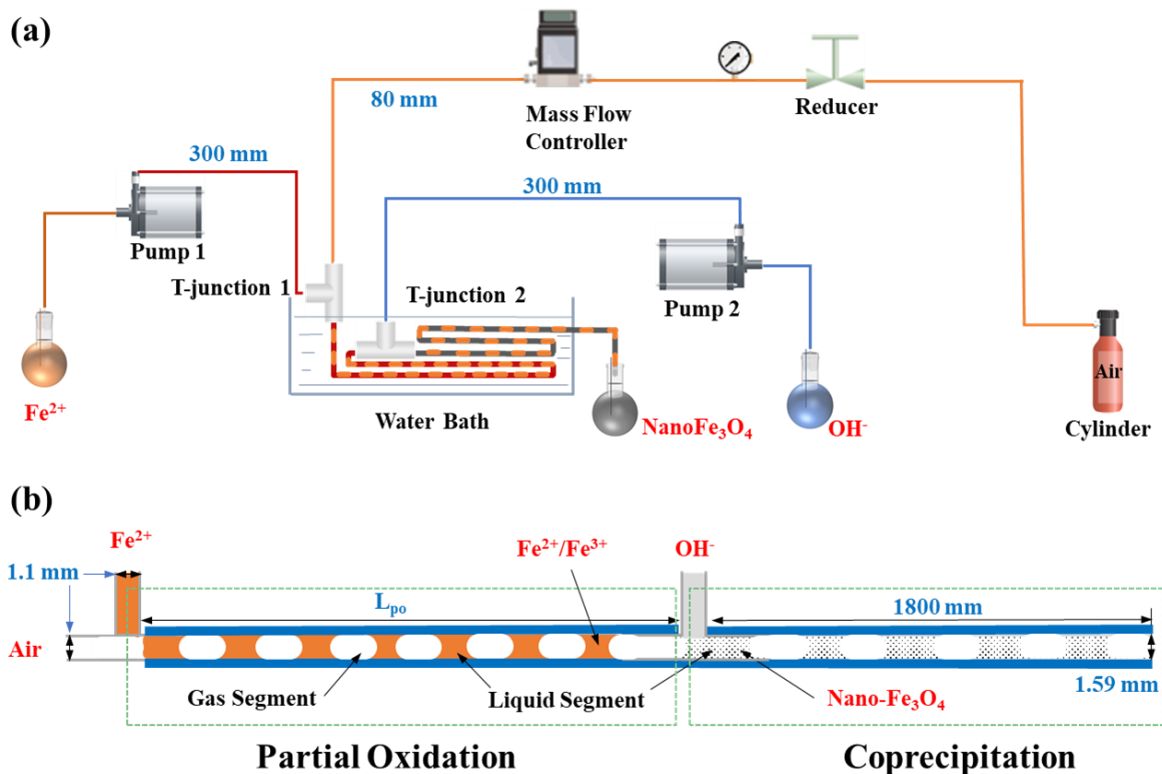


Fig. 6.1 Schematic of (a) the experimental setup. (b) partially oxidation coprecipitation of Fe^{2+} and OH^- to form nano- Fe_3O_4 in liquid segment

Images of the final segments containing the reaction product were captured using a high-speed camera (BU602MCF, Toshiba) and a microscope (STZ-161-TLED-HZ, Shimadzu) installed at the outlet of the PFA tube. A water bath was used to provide the temperature required for the reaction. It is recommended that the two T-junctions as well as their inlet tubes are immersed in the water bath to ensure that the temperature in T-junction 2 does not decrease when the two solvents are mixed.

6.1.2 Chemicals

Ferrous chloride tetrahydrate ($\text{FeCl}_2 \cdot 4\text{H}_2\text{O}$) was purchased from Sigma-Aldrich. Hydrochloric acid (HCl, 35 wt%) was purchased from Nacalai Tesque and sodium

6. Continuous Synthesis of NanoFe₃O₄ by Partial Oxidation Coprecipitation

hydroxide (NaOH, 98.0 wt%), ethylene glycol (EG, 99.5 wt%), ethanol (99.5 wt%), and ammonium chloride (NH₄Cl, 99.5 wt%) were purchased from Fujifilm Wako Pure Chemical Corporation. The solutions used in this study were prepared from the corresponding components and distilled water.

6.1.3 Strategy of partial oxidation and continuous coprecipitation in the microchannel

To prepare Fe₃O₄ nanoparticles using an Fe²⁺ solution, it is necessary to partially oxidize Fe²⁺ to Fe³⁺, to convert the solution to a mixture comprising an Fe²⁺:Fe³⁺ ratio of 1:2. In the microfluidic system (Fig. 6.1(a)), both the Fe²⁺ solution and air are flowed into T-junction 1, forming a segmented flow in the outlet tube. Fe²⁺ can be oxidized to Fe³⁺ by the dissolved oxygen inside the liquid segment, and the mass transfer at the air–liquid interface can quickly replenish the dissolved oxygen concentration in the liquid segment. The oxidation time can be changed by adjusting the tube length between the two T-junctions, thereby influencing the Fe²⁺:Fe³⁺ ratio. When the liquid segment containing Fe²⁺ and Fe³⁺ passes T-junction 2, it mixes with a drop of NaOH solution and the two solutions react (Eq. (1)) to form Fe₃O₄ in the lengthened liquid segment (Fig. 6.1(b)).

In this chapter, a typical synthetic method for the first solution was as follows: 2.6136 g (0.01313 mol) FeCl₂·4H₂O was first dissolved in 50 mL of distilled water after which 20 mL of EG (nucleating agent) was added to the solution. Finally, distilled water was added to form a total volume of 160 mL (0.082 mol/L). The second solution (also 160 mL) was prepared using 1.4885 g (0.03721 mol) NaOH and distilled water. To ensure solution uniformity, both solutions undergo comprehensive mixing followed by a 10 min ultrasonic treatment. The bath temperature was set to 50 °C, according to the typical reaction temperature used in the batch synthesis of Fe₃O₄ nanoparticles [91,113]. The two solutions were pumped into the T-junctions at the same flow rate (3.0 mL/min) to ensure

6. Continuous Synthesis of NanoFe₃O₄ by Partial Oxidation Coprecipitation

an Fe²⁺:OH⁻ molar ratio of 3.0:8.5, while the air flow rate was set to 6.0 mL/min to ensure steady segmented flow. By optimizing the reaction parameters, magnetic Fe₃O₄ nanoparticles were released into the liquid segments and could be separated easily from the reacted solution collected at the outlet of the tube using a magnet. The obtained particles were washed and ultrasonically dispersed (15 min) with ethanol thrice and subsequently dried in an oven at 90 °C for 12 h.

6.2 Influence of the nucleating agent addition method on Fe₃O₄ nanoparticle formation

The first step in the synthesis of Fe₃O₄ nanoparticles from Fe²⁺ ions is to oxidize some of the Fe²⁺ ions to achieve an Fe²⁺:Fe³⁺ ratio of 1:2 in the solution. As discussed in Section 6.1.3, the oxidation reaction takes place in the segmented flow between the two T-junctions, and the final Fe²⁺:Fe³⁺ ratio is determined by the oxidation time. According to Eq. (6.1) and (6.2), to reach an Fe²⁺:Fe³⁺ ratio of 1:2, two thirds of the Fe²⁺ ions must be oxidized by oxygen. Thus, for the 160 mL Fe²⁺ solution used in this study, 0.0022 mol of O₂ was necessary to complete the oxidation reaction. When the air flow rate was twice that of the Fe²⁺ solution, the amount of oxygen in 320 mL of air was approximately 0.003 mol, which was sufficient for the oxidation of Fe²⁺. Therefore, the determination of the oxidation time at which the Fe²⁺:Fe³⁺ ratio reaches 1:2 was key to our investigation.

In the initial step, the continuous synthesis of Fe₃O₄ nanoparticles was carried out through the partial oxidation and coprecipitation of Fe²⁺, with the incorporation of EG into the iron solution, as described in Section 6.1.3, wherein the tube length (L_{po}) between the two T-junctions was varied to change the oxidation time. Table 6.1 (entries a–c) shows images of the collected products at different oxidation times. To obtain a direct-view impression of the product properties, a magnet was placed on one side of the sample bottle. As shown in Table 6.1 (entry c), the particles obtained at $L_{po} = 130$ cm gathered toward

6. Continuous Synthesis of NanoFe₃O₄ by Partial Oxidation Coprecipitation

the magnet, indicating that the product was magnetic. In contrast, the products obtained at $L_{po} = 50$ and 90 cm were barely influenced by the magnet, and the solution was not limpid, indicating that the main products were non-magnetic.

Table 6.1 Reaction products obtained under the different experimental conditions

Method	L_{po}		
	50 cm	90 cm	130 cm
EG in Fe ²⁺ aq.			
EG in NaOH aq.			

Figure 6.2(a) shows the XRD patterns of the particles obtained at $L_{po} = 130$ cm, diffraction patterns were observed at $2\theta = 30.2^\circ, 35.5^\circ, 43.3^\circ, 53.7^\circ, 57.2^\circ,$ and 63.1° , indicating that the product was Fe₃O₄. After calculating the crystal diameter using the Scherrer equation (Table 6.2, entry a), the average crystal diameter was determined to be 10.28 nm. Considering the flowrate of the segmented flow, the oxidation times were approximately 6.6, 11.9, and 17.2 s for $L_{po} = 50, 90,$ and 130 cm, respectively. These results indicated that under these conditions, oxidation was not sufficiently fast in the

6. Continuous Synthesis of NanoFe₃O₄ by Partial Oxidation Coprecipitation

microchannel. Because the segment length was determined by the fluid flow rate and tube diameter, which were constant in this set of experiments, the mixing efficiency was near-identical. Therefore, we supposed that the oxidation efficiency was mainly influenced by the mass transfer of oxygen from the air segment to the liquid segment.

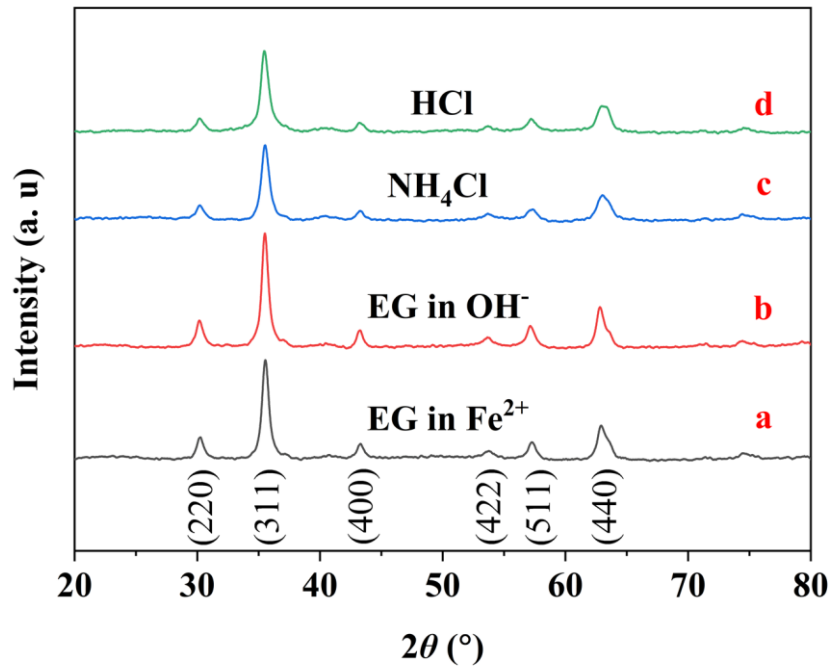


Fig. 6.2 XRD patterns of the Fe₃O₄ nanoparticles obtained in the different experiments

Considering that the inclusion of EG in the iron solution may affect the absorption of oxygen, leading to a subsequent decrease in oxidation efficiency during the partial oxidation process, the reaction strategy was adjusted. This was achieved by altering the addition of EG to the NaOH solution, resulting in the iron solution no longer containing EG. The EG did not influence the liquid phase in the partial oxidation section, but only participated in the coprecipitation process in the second section. Experiments were also conducted at $L_{po} = 50, 90,$ and 130 cm, and the images of the products are shown in Table 6.1 (entries d–f). After removing the EG from the Fe²⁺ solution, the following results were

6. Continuous Synthesis of NanoFe₃O₄ by Partial Oxidation Coprecipitation

observed: At $L_{po} = 50$ cm, the solution above the product was clear enough to see the boundary of the solid phase. At $L_{po} = 90$ cm, the particles gathered toward the magnet, indicating that there was sufficient Fe³⁺ generated in the partial oxidation section, and the coprecipitation reaction in Eq. (6.2) could occur easily in the second section.

Table 6.2 Crystal sizes calculated by the Scherrer equation in the different experiments

2θ (°)	(a) EG in Fe ²⁺		(b) EG in OH ⁻		(c) NH ₄ Cl		(d) HCl	
	FWHM	d_p (nm)	FWHM	d_p (nm)	FWHM	d_p (nm)	FWHM	d_p (nm)
30.2	0.71	11.65	0.75	11.03	0.87	9.42	0.83	9.97
35.5	0.75	11.14	0.74	11.23	0.85	9.79	0.93	9.01
43.3	0.75	11.40	0.56	15.22	0.69	12.44	0.72	11.91
53.7	1.23	7.22	1.15	7.74	1.31	6.78	0.97	9.19
57.2	0.78	11.57	0.83	10.86	0.93	9.74	1.09	8.27
63.1	1.07	8.70	0.97	9.61	1.24	7.54	1.23	7.56
Average		10.28		10.95		9.29		9.32

The XRD pattern of the product displayed in Table 6.1, entry f is shown in Fig. 6.2(b), and is the same as that of the standard card of Fe₃O₄. The calculated crystal size was 10.95 nm (Table 6.2, entry b), and there was no significant difference between the crystal sizes of the products obtained by this method and the non-modified method discussed above. Figure 6.3 (a) and (d) shows images of the corresponding products obtained by adding EG to the FeCl₂ and NaOH solutions, respectively. The two images clearly reveal that when pristine EG was added to the FeCl₂ solution, the particle sizes ranged from 6 to 30 nm and the average particle size was 13.90 nm, which is larger than the value calculated from the XRD pattern. When EG was added to the NaOH solution, the particle size ranged from 5 to 25 nm, and the average particle size was in good agreement with the calculated

6. Continuous Synthesis of NanoFe₃O₄ by Partial Oxidation Coprecipitation

value.

These results indicate that the addition of EG into the FeCl₂ solution not only suppresses the transfer of oxygen into the liquid phase, but also reduces the mixing performance of the liquid segment, thereby resulting in a wider particle size distribution and larger particle size. Accordingly, we deduced that the incorporation of EG into the NaOH solution yields superior results. This strategy has been employed in the subsequent experiments.

6.3 Influence of oxidation time on Fe₃O₄ nanoparticle formation

Fe₃O₄ nanoparticles were formed according to Eq. (6.2), wherein the appropriate Fe²⁺:Fe³⁺ ratio is 1:2. In this partial oxidation strategy, if the oxidation depth is too low or high, the Fe²⁺:Fe³⁺ ratio significantly deviates from the expected value, resulting in the formation of hydroxides (Fe(OH)₂ or Fe(OH)₃) in an alkaline environment. Side reactions waste raw materials and may influence the flow characteristics of the liquid segments, which will further impact the formation of Fe₃O₄ nanoparticles. Thus, using EG in NaOH solution as the nucleating agent, the synthesis process was next carried out at 50 °C with varied L_{po} values of 50, 90, 130, 150, 170, 190, and 210 cm.

The TEM images of the corresponding products are shown in Fig. 6.3 (b)–(h). At L_{po} = 50 cm, significant variations in particle size were observed, with the smallest particle size being <5 nm and the largest >30 nm. With the subsequent increase in L_{po} , the Fe²⁺:Fe³⁺ ratio gradually approached 1:2, and the nanoparticle size became more uniform; however, when L_{po} exceeded 150 cm, the variation in particle size increased again.

6. Continuous Synthesis of NanoFe₃O₄ by Partial Oxidation Coprecipitation

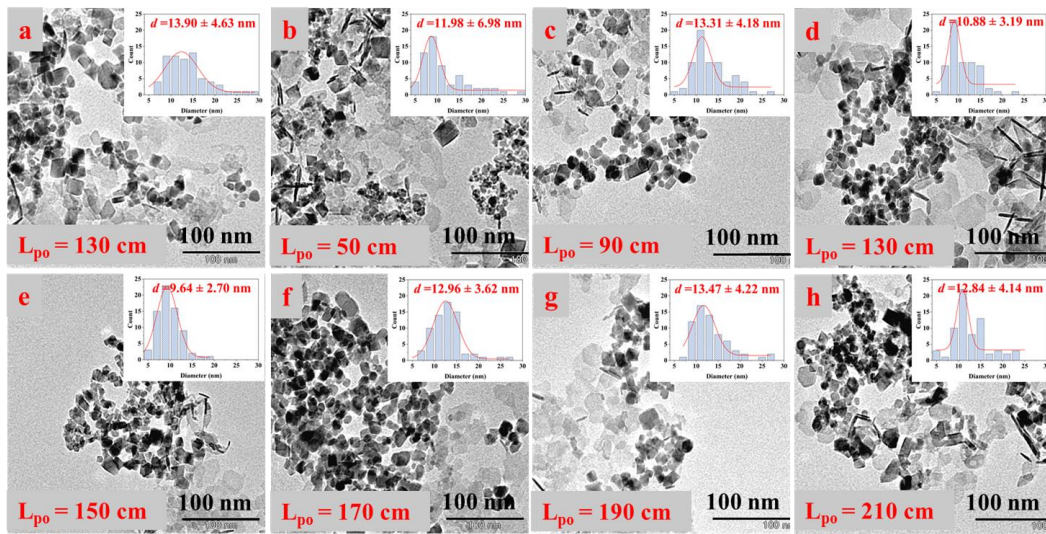


Fig. 6.3 TEM images of Fe₃O₄ nanoparticles obtained with (a) EG in FeCl₂ aq. and (b)–(h) EG in NaOH aq. at different oxidation times

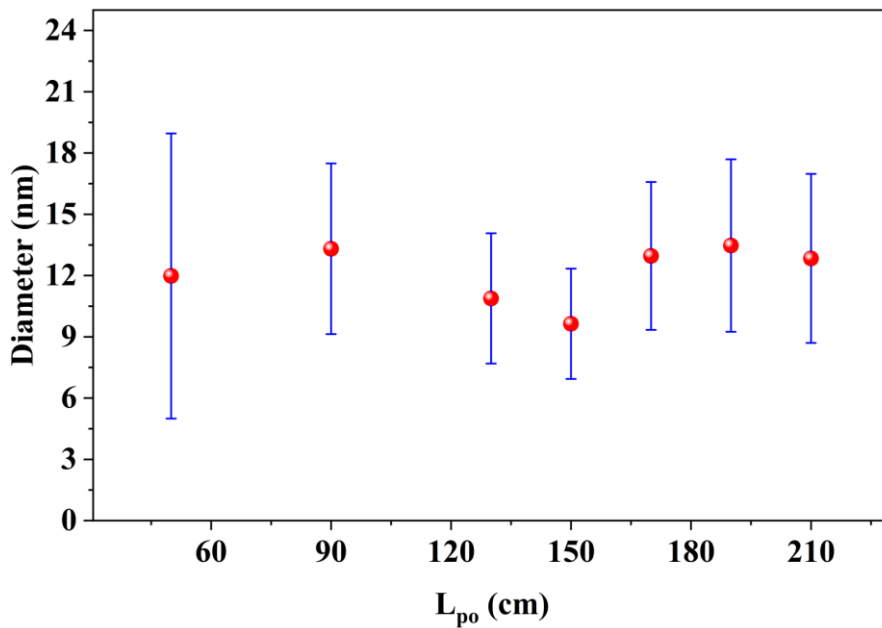


Fig. 6.4 Influence of oxidation time on the Fe₃O₄ nanoparticle size

A plot of the average particle size against L_{po} is shown in Fig. 6.4. The plot reveals that the average particle size varies around 12 nm as the L_{po} value ranges from 90 cm to

6. Continuous Synthesis of NanoFe₃O₄ by Partial Oxidation Coprecipitation

210 cm. Notably, the smallest particle size is observed at $L_{po} = 150$ cm, suggesting that the Fe²⁺:Fe³⁺ ratio is closest to the optimal 1:2 ratio at this specific length. Here, the coprecipitation reaction was dominant, and was negligibly influenced by the side products. The particle sizes obtained at $L_{po} = 130$ and 170 cm were also quite uniform, whereas the particle size at $L_{po} = 170$ cm was 19% larger than that attained at $L_{po} = 130$ cm. These results indicate that the existence of excess Fe³⁺ ions adversely affected the formation of smaller Fe₃O₄ nanoparticles. At $L_{po} = 150$ cm, the corresponding oxidation time was approximately 19.2 s. Therefore, we supposed that the most suitable partial oxidation time should be approximately 19.2 s and is attained when L_{po} is fixed at 150 cm.

6.4 Influence of acid additives on Fe₃O₄ nanoparticle formation

We expected the partial oxidation of Fe²⁺ to Fe³⁺ to proceed according to Eq. (6.1) and that at the appropriate oxidation time, the final product of the coprecipitation reaction in the second section would be Fe₃O₄. However, even at $L_{po} = 150$ cm, the initial collected products still contained some floccules suspended in the top solution during the magnetic separation process. Moreover, in the TEM images of the products after washing and ultrasonic dispersion, some Fe₃O₄ nanoparticles were surrounded by floccules. We supposed that the flocculant is a hydroxide formed by excess Fe²⁺ or Fe³⁺. The floccules observed in the TEM images were attributed to two possible reactions: formation during the partial oxidation period or as a side product in the coprecipitation section.



6. Continuous Synthesis of NanoFe₃O₄ by Partial Oxidation Coprecipitation

Equation (6.1) represents the ideal reaction necessary for partial oxidation. However, there are no free H⁺ ions in the neutral solution, the H⁺ ions in the neutral solution stem from the ionization of H₂O, whereby the consumption of H⁺ ions is accompanied by the release of an equal amount of OH⁻ ions into the solution. This results in the partial oxidation of Fe²⁺ in the neutral solution occurs as Eq. (6.3) essentially. Specifically, one-third of the reacted Fe²⁺ is transformed into Fe(OH)₃ in the partial oxidation section.

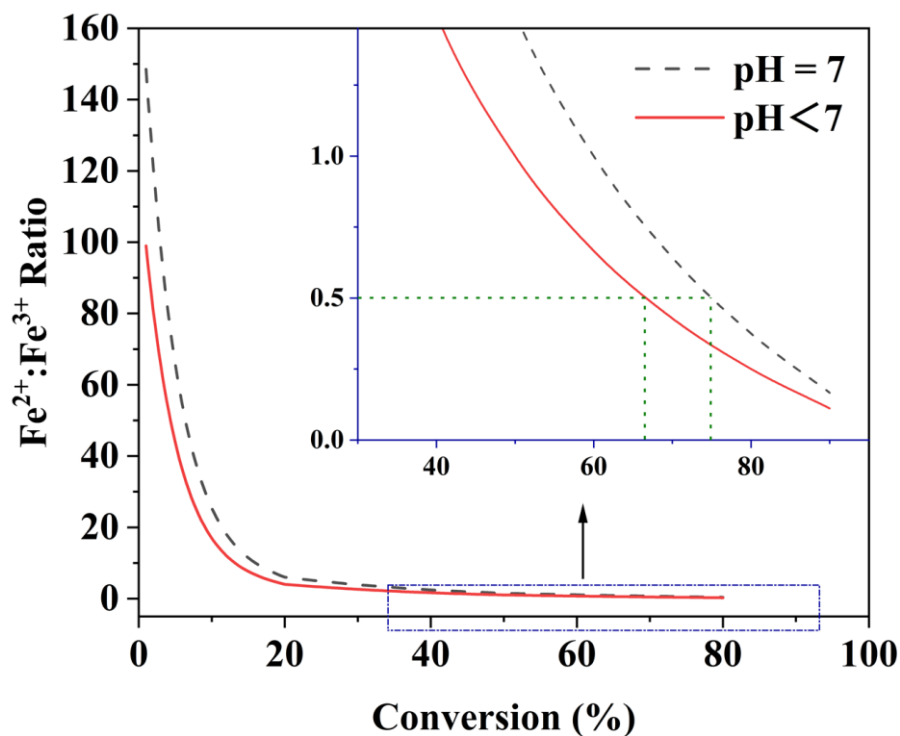


Fig. 6.5 Correlation between the Fe²⁺:Fe³⁺ ratio and conversion at pH = 7 and pH < 7

Fig. 6.5 shows the correlation between the Fe²⁺:Fe³⁺ ratio and Fe²⁺ conversion, corresponding to Eq. (6.1) and (6.3), respectively. At pH < 7, 66.7% of the Fe²⁺ ions must be oxidized to reach an Fe²⁺:Fe³⁺ ratio of 1:2, whereas at pH 7, for the same Fe²⁺:Fe³⁺ ratio, 75.0% of the Fe²⁺ ions must be oxidized. Thus, in neutral solution, 8.3% of the raw

6. Continuous Synthesis of NanoFe₃O₄ by Partial Oxidation Coprecipitation

material is wasted, and the formation of Fe(OH)₃ may subsequently affect the downstream coprecipitation reaction.

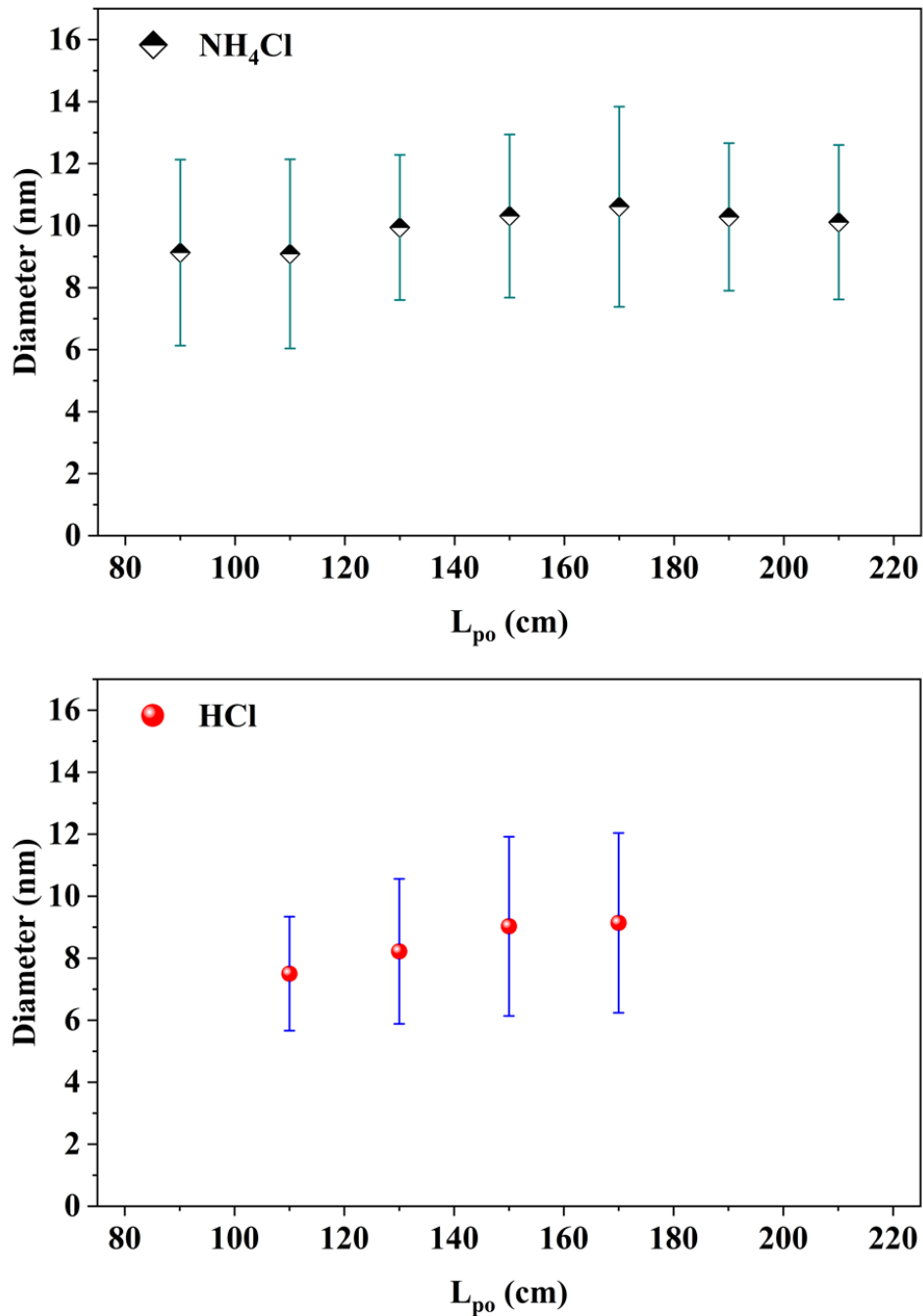


Fig. 6.6 Influence of the acid additive on the Fe₃O₄ nanoparticle size under different oxidation times.

6. Continuous Synthesis of NanoFe₃O₄ by Partial Oxidation Coprecipitation

To evaluate the influence of acid additives on the formation of Fe₃O₄ nanoparticles, NH₄Cl or HCl was added to the FeCl₂ solution at a molar ratio of 2:3 to create an acidic environment. The nanoparticle sizes obtained using the two additives at different oxidation times are shown in Fig. 6.6. With the addition of NH₄Cl to the FeCl₂ solution, a noticeable decrease in nanoparticle sizes to approximately 10 nm is observed.

The replacement of HCl with NH₄Cl led to an additional reduction in size, averaging around 8 nm. Interestingly, under these conditions, the particle sizes consistently remained smaller than those observed under previously mentioned conditions. In particular, at $L_{po} = 130$ cm, the particle size obtained without acid additives was 10.88 ± 3.19 nm, whereas in the presence of NH₄Cl and HCl additives, the particle size decreased to 9.94 ± 2.34 and 8.22 ± 2.33 nm, respectively.

It is thus clear that an acidic environment facilitates the formation of Fe₃O₄ nanoparticles, the nanoparticle size decreasing with increasing acid strength. When NH₄Cl is used as an additive, the H⁺ ions originate from the ionization of NH₄⁺, and the ionization balance described by Eq. (6.4) slows the release of H⁺ into the solution [115]—the final expression for the oxidation reaction is given by Eq. (6.5). Consequently, the particle size falls between those obtained in the neutral and HCl solutions. Meanwhile, the nanoparticle sizes obtained with NH₄Cl and HCl additives were in good agreement with the crystal diameters calculated using the Scherrer equation (Table 6.2, entries c and d), indicating that the nanoparticles were mainly primary particles and seldom grew in the growth section. These findings suggest that the addition of HCl to the FeCl₂ solution can suppress the formation of hydroxides in the partial oxidation section and subsequently improve the performance of the precipitation section to form smaller Fe₃O₄ nanoparticles.

6.5 Influence of H⁺:Fe²⁺ ratio on the Fe₃O₄ nanoparticle size

As described in Section 6.4, the amount of HCl added to the FeCl₂ solution was

6. Continuous Synthesis of NanoFe₃O₄ by Partial Oxidation Coprecipitation

sufficient for the oxidation reaction and significantly improved the product quality. We next investigated the influence of the H⁺:Fe²⁺ ratio on the nanoparticle size by increasing the amount of HCl added to the FeCl₂ solution. Based on the stoichiometric values in Eq. (6.1), the amount of HCl was increased by 1.33 and 1.67 times the amount used in the previous experiment (Section 6.4), thereby changing the H⁺:Fe²⁺ ratios to 0.67:1, 0.89:1, and 1.12:1 with respect to the initial mole amount of Fe²⁺.

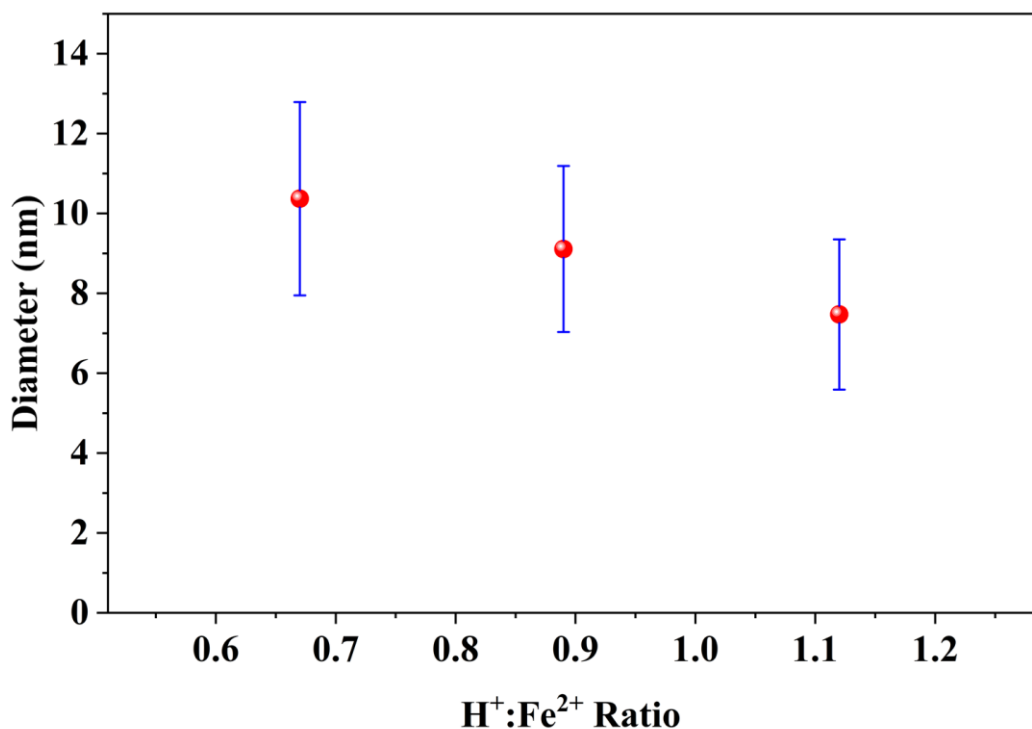


Fig. 6.7 Fe₃O₄ nanoparticle size obtained with different H⁺:Fe²⁺ ratios

Figure 6.7 shows that there was a decrease in the nanoparticle size with an increase in the H⁺:Fe²⁺ ratio at $L_{po} = 130$ cm. However, there was no significant difference between the particle size ranges, and the average particle sizes were all <10 nm. Although there was a slight decrease in particle size, the superfluous amount of HCl neutralized part of the NaOH solution, which was necessary for coprecipitation, thereby causing an increase in the consumption of NaOH. This additional material consumption is detrimental to the

6. Continuous Synthesis of NanoFe₃O₄ by Partial Oxidation Coprecipitation

productivity and poses an extra burden on waste treatment. Hence, a H⁺:Fe²⁺ ratio of 0.67:1 was established as the adequate ratio for the partial oxidation process.

6.6 Influence of OH⁻:Fe²⁺ ratio on the Fe₃O₄ nanoparticle size

As discussed in Section 6.5, the floccules present in both the initially collected and washed products were formed from the reaction of the metal cations with OH⁻ anions. An excess amount of NaOH was added to ensure that the coprecipitation reaction proceeded completely. The designed OH⁻:Fe²⁺ ratio at the inlet of the coprecipitation section was 8.5:1, which is slightly larger than the stoichiometric number ratio in Eq. (6.1). To explore the possibility of reducing the amount of NaOH, the influence of the OH⁻:Fe²⁺ ratio on the nanoparticle size was estimated at $L_{po} = 130$ cm.

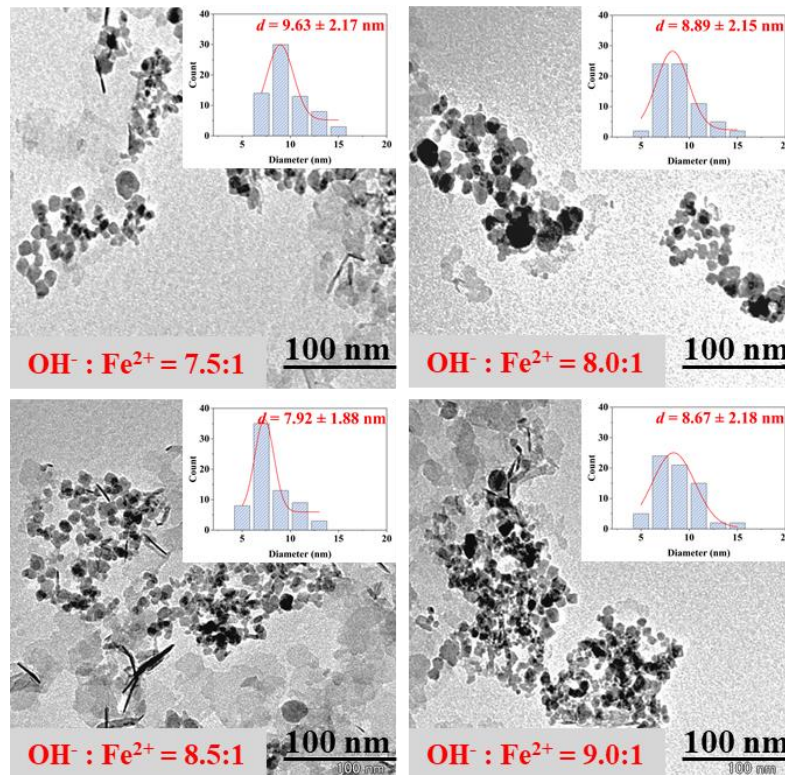


Fig. 6.8 Fe₃O₄ nanoparticle sizes obtained with different OH⁻:Fe²⁺ ratios

6. Continuous Synthesis of NanoFe₃O₄ by Partial Oxidation Coprecipitation

Figure 6.8 presents an overview of the TEM images of the nanoparticles synthesized with different OH⁻:Fe²⁺ ratios. At an OH⁻:Fe²⁺ ratio of 8.5:1, the nanoparticle size was in the range of 7.92±1.88 nm, and more than half of the nanoparticle sizes were concentrated in this range. However, at OH⁻:Fe²⁺ ratios of 7.5:1 and 8.0:1, the particle size distribution became wider and the particle size range larger. When the OH⁻:Fe²⁺ ratio was increased to 9.0:1, the same trend was observed.

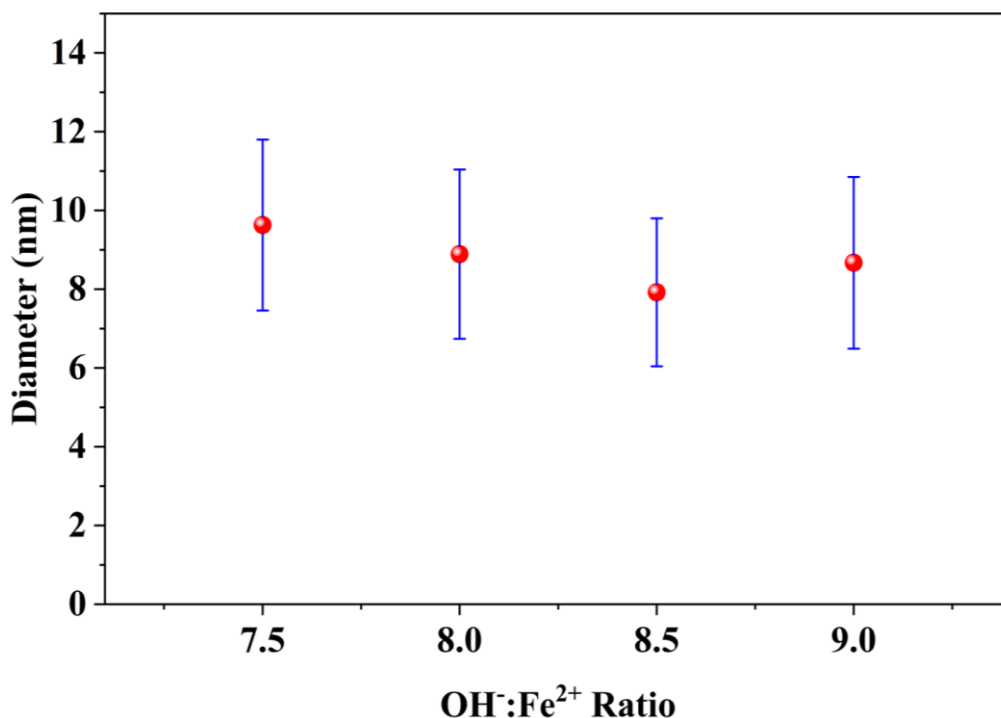


Fig. 6.9 Fe₃O₄ nanoparticle sizes obtained with different OH⁻:Fe²⁺ ratios

As illustrated in Fig. 6.9, when the OH⁻:Fe²⁺ ratio increased from 7.5:1 to 9.0:1, the average particle sizes stabilized at approximately 9 nm. The smallest recorded value was achieved at an OH⁻:Fe²⁺ ratio of 8.5:1. Thus, we concluded that 8.5:1 is a reasonable OH⁻:Fe²⁺ ratio under which small uniform Fe₃O₄ nanoparticles can be generated.

6. Continuous Synthesis of NanoFe₃O₄ by Partial Oxidation Coprecipitation

6.7 Comparison with directly coprecipitation strategy

In contrast to the coprecipitation method utilized in Chapter 5, this in situ oxidation approach offers several advantages. First, it employs Fe²⁺ as the initial reactant, eliminating concerns about Fe²⁺ oxidation, as oxidation is inherently part of the overall reaction. Second, the gas used to create the gas segment is ambient air, which serves as the oxidizing agent due to its oxygen content. This methodology is both economically efficient and readily available. Lastly, the average size of the resulting nanoparticles is approximately 9 nm, which closely aligns with the size of nanoparticles obtained through the direct use of a Fe²⁺ and Fe³⁺ mixture, which produces nanoparticles of approximately 6 nm.

One limitation of this approach is the necessity for an extra acid additive to ensure optimal oxidation efficiency. Moreover, the length of the oxidation section's tube must be adjusted in accordance with the flow rate and concentration of the feed.

6.8 Conclusions

Fe₃O₄ nanoparticles were continuously synthesized in a segmented flow via partial oxidation coprecipitation. The partial oxidation section generated Fe³⁺ ions by oxidizing Fe²⁺ with oxygen, obviating the need for nitrogen to establish an anoxic environment. The liquid segment serves as a microreactor, featuring strong internal mixing that ensures rapid nuclei generation in the coprecipitation section, resulting in smaller-sized particles. The methods for adding the nucleating agent, partial oxidation time, acid additive source, and H⁺:Fe²⁺ and OH⁻:Fe²⁺ ratios were scrutinized to ascertain the optimum operating conditions, and XRD and TEM techniques were employed to evaluate product quality. The results indicate that it is advantageous to introduce a nucleating agent into the NaOH solution, the incorporation of HCl into the FeCl₂ solution enhances oxidation efficiency,

6. Continuous Synthesis of NanoFe₃O₄ by Partial Oxidation Coprecipitation

the ideal oxidation time is 19.2 s, and at an H⁺:OH⁻:Fe²⁺ ratio of 0.67:8.5:1, the prepared Fe₃O₄ nanoparticles exhibit the smallest diameter (approximately 8 nm). The size distribution is confined between 5 and 13 nm, which is more restricted than previously reported data.

7

Conclusions

This study achieves the regularly control of the segment length in a gas–liquid microchannel system by employing a high-speed valve in a segmented flow generating device. The segment length generated in the microchannel without the high-speed valve was determined by the flow rate and channel size, which remained constant once flow began. Notably, by adjusting the operating frequency of the high-speed valve, the segment length was successfully manipulated within a wide frequency range, at a flow rate of 2 mL/min for both phases. The high-speed valve was able to reproducibly control the segment length at frequencies below 15 s⁻¹. However, the tiny generated segments could not be maintained in the microchannel when the frequency exceeded 15 s⁻¹, and segment length was not evidently influenced by valve frequencies exceeding 22 s⁻¹. This phenomenon occurs because the duration of squeezing remains relatively constant during the segment generation process as the valve frequency increases. In addition, a gas-to-liquid flow rate ratio in the range of 0.7–1.2 is deemed necessary for regular segmented flow. Based on a mass balance, a correlation between valve frequency, biphasic flow rate, and channel diameter was proposed to predict the segment length controlled by the high-speed valve, which agreed with the experimental results.

Following this, the influence of segment length on mass transfer performance in valve-controlled gas–liquid segmented flows was investigated. Mass transfer measurements were performed in a flask with a valve frequency of 8 to 23 s⁻¹, when the

7. Conclusions

flow rate of both phases was 4.0 mL/min. $[kLa]_{overall}$ and $[kLa]_b$ were determined for the different configurations to calculate the $[kLa]_s$ in segmented flow. These results revealed that $[kLa]_s$ is proportional to f before the liquid phase becomes saturated with oxygen. Meanwhile, the specific areas a and $[kLa]_s$ can be predicted accurately by using the correlations derived from the valve frequency, fluid flow rate, and microchannel diameter.

Subsequently, uniform Fe₃O₄ nanoparticles were synthesized continuously using the coprecipitation method in gas-liquid segmented flow with Fe²⁺, Fe³⁺, and OH⁻. The process leveraged the enhanced mass transfer in segmented flow. By optimizing the iron concentration, reaction temperature, and Fe²⁺:Fe³⁺ ratio, this in situ strategy achieved the precise synthesis of Fe₃O₄ nanoparticles within 0.1 s at 50 °C, a process that requires hours in batch reactions. Moreover, the operation of the ALD valve can regulate the segment length, thus adjusting the mass transfer rate within the liquid segment. Consequently, the nanoparticle size can be controlled at approximately 6 nm, ensuring a narrow size distribution. The simple and practicable construction of the system presents an advantage over other continuous methods for Fe₃O₄ nanoparticle synthesis.

The experimental setup was further fine-tuned to facilitate the synthesis of Fe₃O₄ nanoparticles through a process involving partial oxidation coprecipitation. The partial oxidation section generated Fe³⁺ ions by oxidizing Fe²⁺ with oxygen, obviating the need for nitrogen to establish an anoxic environment. The liquid segment serves as a microreactor, featuring strong internal mixing that ensures rapid nuclei generation in the coprecipitation section, resulting in smaller-sized particles. The methods for adding the nucleating agent, partial oxidation time, acid additive source, and H⁺:Fe²⁺ and OH⁻:Fe²⁺ ratios were scrutinized to ascertain the optimum operating conditions, and XRD and TEM techniques were employed to evaluate product quality. The results indicate that it is advantageous to introduce a nucleating agent into the NaOH solution, the incorporation of HCl into the FeCl₂ solution enhances oxidation efficiency, the ideal oxidation time is 19.2 s, and at an H⁺:OH⁻:Fe²⁺ ratio of 0.67:8.5:1, the prepared Fe₃O₄ nanoparticles exhibit the smallest diameter (approximately 8 nm). The size distribution is confined between 5

7. Conclusions

and 13 nm, which is more restricted than previously reported data.

In conclusion, this study presents a groundbreaking method for maintaining stable control over gas-liquid segment length in microchannels. It signifies the primary and thorough exploration of the impact of segment length on mass transfer performance in segmented flow, all without modifying fluid flow rates. Moreover, this segmented flow synthesis technique holds promise for revolutionizing the continuous industrial production of Fe₃O₄ nanoparticles. With proper scale-up and mitigation of potential blockage issues, this method has the potential to transform the synthesis process of Fe₃O₄ nanoparticles on a large scale. These findings not only enhance the efficacy of gas-liquid reactions in microreactors but also advance our understanding of mass transfer processes in segmented flows, setting the stage for future exploration of segmented flows in multiphase microreactor systems.

Recommendations for future studies

In the future, there are several potential extensions for the current study to facilitate the widespread application of this gas-liquid segmented flow-based microreactor.

The initial extension involves replacing the transparent tube and T-junction with metal counterparts, thereby enabling the expansion of the system to diverse conditions. While the current transparent system facilitates the visibility of segmented flow inside the tube and is easy to assemble, it is limited by its inability to withstand high temperature and pressure. Introducing a metal system would address this drawback, allowing for processes with more stringent parameters.

The second extension involves investigating strategies for segment length control in multiple channels. This exploration serves as the foundation for scaling up the system, a crucial step for its application in industrial-scale processes. Additionally, the long-term stability of the high-speed valve requires special attention, as it is essential for ensuring continuous operation.

7. Conclusions

The third extension involves attempting the nanoFe₃O₄ synthesis process at higher temperatures within a metal tube. Research suggests that temperature can impact the morphology and magnetic properties of nanoFe₃O₄, which holds significance for its application across various fields. Furthermore, establishing a continuous separation process for nanoFe₃O₄ will enhance the overall integrity of the process.

Lastly, exploring the in-situ synthesis of a nanoFe₃O₄-based catalyst emerges as an intriguing avenue. The nanoscale dimensions of the catalyst offer a substantial interface for reactions, mitigating mass transfer challenges within the catalyst and thereby enhancing reaction efficiency. Furthermore, the magnetic properties of the catalyst enable easy separation, opening up possibilities for developing a continuous process with catalyst recycling.

References

- [1] D.B. Tuckerman, R.F.W. Pease, High-Performance Heat Sinking for VLSI, IEEE Electron Device Lett. EDL-2 (1981) 126–129. <https://doi.org/10.1109/EDL.1981.25367>.
- [2] J.J. Lerou, K.M. Ng, Chemical reaction engineering: A multiscale approach to a multiobjective task, Chem. Eng. Sci. 51 (1996) 1595–1614. [https://doi.org/10.1016/0009-2509\(96\)00022-X](https://doi.org/10.1016/0009-2509(96)00022-X).
- [3] J. J. Lerou, Reactor System Synthesis and Design, AIChE Symp. Ser. 91 (1995) 39–40.
- [4] Y. Liu, Q. Zhao, J. Yue, C. Yao, G. Chen, Effect of mixing on mass transfer characterization in continuous slugs and dispersed droplets in biphasic slug flow microreactors, Chem. Eng. J. 406 (2021) 126885. <https://doi.org/10.1016/j.cej.2020.126885>.
- [5] Q. Wu, Y. Wang, D. Mei, S. Si, Development of methanol steam reforming microreactor based on stacked wave sheets and copper foam for hydrogen production, Int. J. Hydrogen Energy. 47 (2022) 6282–6294. <https://doi.org/10.1016/j.ijhydene.2021.11.221>.
- [6] G1 Reactor, (n.d.). <https://www.corning.com/jp/jp.html>.
- [7] The Modular MicroReaction System, (n.d.). <https://www.ehrfeld.com/en/mmrs>.
- [8] O. Wörz, K.P. Jäckel, T. Richter, A. Wolf, Microreactors, a new efficient tool for optimum reactor design, Chem. Eng. Sci. 56 (2001) 1029–1033. [https://doi.org/10.1016/S0009-2509\(00\)00318-3](https://doi.org/10.1016/S0009-2509(00)00318-3).
- [9] M. Mohadesi, A. Gouran, A. Dehghan Dehnavi, Biodiesel production using low cost material as high effective catalyst in a microreactor, Energy. 219 (2021) 119671. <https://doi.org/10.1016/j.energy.2020.119671>.
- [10] D. Zhang, F. He, Z. Miao, Y.D. Zhang, Intensified extraction and separation of zinc from cadmium and manganese by a slug flow capillary microreactor, Sep. Purif. Technol. 267 (2021) 118564. <https://doi.org/10.1016/j.seppur.2021.118564>.

- [11] L. Lu, T. Luo, Y. Zhao, C. Cai, Z. Fu, Y. Jin, Interaction between microplastics and microorganism as well as gut microbiota: A consideration on environmental animal and human health, *Sci. Total Environ.* 667 (2019) 94–100.
<https://doi.org/10.1016/j.scitotenv.2019.02.380>.
- [12] C. Du, P. Wang, Y. Hu, J. Zhang, G. Luo, Liquid-Liquid Mass Transfer Enhancement in Milliscale Packed Beds, *Ind. Eng. Chem. Res.* 59 (2020) 4048–4057.
<https://doi.org/10.1021/acs.iecr.9b04225>.
- [13] A.B. Hamzah, T. Fukuda, S. Ookawara, S. Yoshikawa, H. Matsumoto, Process intensification of dry reforming of methane by structured catalytic wall-plate microreactor, *Chem. Eng. J.* 412 (2021) 128636.
<https://doi.org/10.1016/j.cej.2021.128636>.
- [14] T. Fukuda, M.R. Harada, S. Ookawara, A.B. Hamzah, S. Yoshikawa, H. Matsumoto, Double-layered catalytic wall-plate microreactor for process intensification of dry reforming of methane: Reaction activity improvement and coking suppression, *Chem. Eng. Process. - Process Intensif.* 164 (2021) 108406.
<https://doi.org/10.1016/j.cep.2021.108406>.
- [15] Y. Wang, H. Liu, D. Mei, Q. Wu, H. Zhou, A novel thermally autonomous methanol steam reforming microreactor using SiC honeycomb ceramic as catalyst support for hydrogen production, *Int. J. Hydrogen Energy.* 46 (2021) 25878–25892.
<https://doi.org/10.1016/j.ijhydene.2021.05.103>.
- [16] S. Pandey, D. Mukherjee, P. Kshirsagar, C. Patra, D. Bodas, Multiplexed bio-imaging using cadmium telluride quantum dots synthesized by mathematically derived process parameters in a continuous flow active microreactor, *Mater. Today Bio.* 11 (2021) 100123. <https://doi.org/10.1016/j.mtbio.2021.100123>.
- [17] N.H. Margi, G.D. Yadav, Design of a novel dual function membrane microreactor for liquid-liquid-liquid phase transfer catalysed reaction: Selective synthesis of 1-naphthyl glycidyl ether, *React. Chem. Eng.* 6 (2021) 858–867.
<https://doi.org/10.1039/d1re00030f>.

- [18] L. Xiang, M. Qiu, M. Shang, Y. Su, Continuous synthesis of star polymers with RAFT polymerization in cascade microreactor systems, *Polymer (Guildf)*. 222 (2021) 123669. <https://doi.org/10.1016/j.polymer.2021.123669>.
- [19] Q. Xue, Z. Li, M. Chen, Y. Wang, B. Yan, G. Luo, Co-precipitation continuous synthesis of the Ni-Rh-Ce_{0.75}Zr_{0.25}O_{2-δ} catalyst in the membrane dispersion microreactor system for n-dodecane steam reforming to hydrogen, *Fuel*. 297 (2021) 120785. <https://doi.org/10.1016/j.fuel.2021.120785>.
- [20] J. Fan, J. Lu, Z. Sha, W. Zuo, X. Fei, M. Zhu, Conformally anchoring nanocatalyst onto quartz fibers enables versatile microreactor platforms for continuous-flow catalysis, *Sci. China Chem.* (2021). <https://doi.org/10.1007/s11426-021-1101-4>.
- [21] J.S.-I. Kwon, N. Sitapure, R.W. Epps, M. Abolhasani, Cfd-based computational studies of quantum dot size control in slug flow crystallizers: Handling slug-to-slug variation, *Ind. Eng. Chem. Res.* 60 (2021) 4930–4941. <https://doi.org/10.1021/acs.iecr.0c06323>.
- [22] J.S.-I. Kwon, M. Nayhouse, G. Orkoulas, P.D. Christofides, Crystal shape and size control using a plug flow crystallization configuration, *Chem. Eng. Sci.* 119 (2014) 30–39. <https://doi.org/10.1016/j.ces.2014.07.058>.
- [23] S. Bhattacharyya, P. Desir, S. Prodingler, R.F. Lobo, D.G. Vlachos, Improved slit-shaped microseparator and its integration with a microreactor for modular biomanufacturing, *Green Chem.* 23 (2021) 3700–3714. <https://doi.org/10.1039/d1gc00642h>.
- [24] G. Gaikwad, P. Bangde, K. Rane, J. Stenberg, L. Borde, S. Bhagwat, P. Dandekar, R. Jain, Continuous production and separation of new biocompatible palladium nanoparticles using a droplet microreactor, *Microfluid. Nanofluidics*. 25 (2021) 1–15. <https://doi.org/10.1007/s10404-020-02410-x>.
- [25] Bayer's continuous microreactor technology, n.d. <https://www.doc88.com/p-07139000274996.html>.
- [26] M. Zhang, Z. Yu, Z. Sun, A. Wang, J. Zhang, Y.Y. Liu, Y. Wang, Continuous synthesis of ZIF-67 by a microchannel mixer: A recyclable approach, *Microporous Mesoporous Mater.* 327 (2021) 111423. <https://doi.org/10.1016/j.micromeso.2021.111423>.

- [27] P. Shrimal, G. Jadeja, J. Naik, S. Patel, Continuous microchannel precipitation to enhance the solubility of telmisartan with poloxamer 407 using Box-Behnken design approach, *J. Drug Deliv. Sci. Technol.* 53 (2019) 101225.
<https://doi.org/10.1016/j.jddst.2019.101225>.
- [28] L. You, J. Cao, F. Liu, A novel microchannel synthesis strategy for continuous fabrication of nanosized γ -CuI and their photocatalytic performance, *Ind. Eng. Chem. Res.* 58 (2019) 10941–10950. <https://doi.org/10.1021/acs.iecr.9b00354>.
- [29] E. Effati, B. Pourabbas, M.S. Zakerhamidi, Continuous microfluidic fabrication of polypyrrole nanoparticles, *RSC Adv.* 9 (2019) 16977–16988.
<https://doi.org/10.1039/c9ra00946a>.
- [30] Y. Yang, L. Zhang, K. Jin, M. He, W. Wei, X. Chen, Q. Yang, Y. Wang, W. Pang, X. Ren, X. Duan, Self-adaptive virtual microchannel for continuous enrichment and separation of nanoparticles, *Sci. Adv.* 8 (2022). <https://doi.org/10.1126/sciadv.abn8440>.
- [31] S.O. Hong, K.S. Park, D.Y. Kim, S.S. Lee, C.S. Lee, J.M. Kim, Gear-shaped micromixer for synthesis of silica particles utilizing inertio-elastic flow instability, *Lab Chip.* 21 (2021) 513–520. <https://doi.org/10.1039/d0lc00834f>.
- [32] S. Kim, H. Wang, L. Yan, X. Zhang, Y. Cheng, Continuous preparation of itraconazole nanoparticles using droplet-based microreactor, *Chem. Eng. J.* 393 (2020) 124721.
<https://doi.org/10.1016/j.cej.2020.124721>.
- [33] B. Prakash, V. Katoch, A. Shah, M. Sharma, M.M. Devi, J.J. Panda, J. Sharma, A.K. Ganguli, Continuous flow reactor for the controlled synthesis and inline photocatalysis of antibacterial Ag₂S nanoparticles, *Photochem. Photobiol.* 96 (2020) 1273–1282.
<https://doi.org/10.1111/php.13297>.
- [34] H. Ma, Q. Zhao, C. Yao, Y. Zhao, G. Chen, Effect of fluid viscosities on the liquid-liquid slug flow and pressure drop in a rectangular microreactor, *Chem. Eng. Sci.* 241 (2021) 116697. <https://doi.org/10.1016/j.ces.2021.116697>.
- [35] H. Lv, Z. Yang, J. Zhang, G. Qian, X. Duan, Z. Shu, X. Zhou, Liquid flow and mass transfer behaviors in a butterfly-shaped microreactor, *Micromachines.* 12 (2021).

- <https://doi.org/10.3390/mi12080883>.
- [36] A. V. Kovalev, A.A. Yagodnitsyna, A. V. Bilsky, Flow hydrodynamics of immiscible liquids with low viscosity ratio in a rectangular microchannel with T-junction, *Chem. Eng. J.* 352 (2018) 120–132. <https://doi.org/10.1016/j.cej.2018.07.013>.
- [37] M. Li, Y. Zhang, J. Zhang, M. Peng, L. Yan, Z. Tang, Q. Wu, Continuous Gas-Liquid-Solid Slug Flow for Sustainable Heterogeneously Catalyzed PET-RAFT Polymerization, *Ind. Eng. Chem. Res.* 60 (2021) 5451–5462. <https://doi.org/10.1021/acs.iecr.1c00361>.
- [38] J.R. Burns, C. Ramshaw, The intensification of rapid reactions in multiphase systems using slug flow in capillaries, *Lab Chip.* 1 (2001) 10–15.
<https://doi.org/10.1039/b102818a>.
- [39] Z. Cao, Z. Wu, B. Sundén, Dimensionless analysis on liquid-liquid flow patterns and scaling law on slug hydrodynamics in cross-junction microchannels, *Chem. Eng. J.* 344 (2018) 604–615. <https://doi.org/10.1016/j.cej.2018.03.119>.
- [40] A. Salim, M. Fourar, J. Pironon, J. Sausse, Oil-water two-phase flow in microchannels: FLOW patterns and pressure drop measurements, *Can. J. Chem. Eng.* 86 (2008) 978–988.
<https://doi.org/10.1002/cjce.20108>.
- [41] Q. Zhang, H. Liu, S. Zhao, C. Yao, G. Chen, Hydrodynamics and mass transfer characteristics of liquid–liquid slug flow in microchannels: The effects of temperature, fluid properties and channel size, *Chem. Eng. J.* 358 (2019) 794–805.
<https://doi.org/10.1016/j.cej.2018.10.056>.
- [42] G.N. Ahn, S. Taniguchi, T. Aoyama, S. Hasebe, D.P. Kim, O. Tonomura, Formation of gas-liquid slugs in millimeter-scale T-junctions – Slug size estimation framework, *Chem. Eng. J.* 385 (2020) 123492. <https://doi.org/10.1016/j.cej.2019.123492>.
- [43] V. Van Steijn, C.R. Kleijn, M.T. Kreutzer, Predictive model for the size of bubbles and droplets created in microfluidic T-junctions, *Lab Chip.* 10 (2010) 2513–2518.
<https://doi.org/10.1039/c002625e>.
- [44] N. von Vietinghoff, D. Hellmann, J. Priebe, D.W. Agar, Intermediate gas feed in bi-or triphasic gas–liquid(–liquid) segmented slug flow capillary reactors, *Symmetry (Basel)*.

- 12 (2020) 1–21. <https://doi.org/10.3390/sym12122092>.
- [45] M.N. Kashid, I. Gerlach, S. Goetz, J. Franzke, J.F. Acker, F. Platte, D.W. Agar, S. Turek, Internal circulation within the liquid slugs of a liquid-liquid slug-flow capillary microreactor, *Ind. Eng. Chem. Res.* 44 (2005) 5003–5010. <https://doi.org/10.1021/ie0490536>.
- [46] Y. Yin, C. Zhu, T. Fu, Y. Ma, K. Wang, G. Luo, Enhancement effect and mechanism of gas-liquid mass transfer by baffles embedded in the microchannel, *Chem. Eng. Sci.* 201 (2019) 264–273. <https://doi.org/10.1016/j.ces.2019.02.039>.
- [47] P. Sobieszuk, R. Pohorecki, P. Cygański, J. Grzelka, Determination of the interfacial area and mass transfer coefficients in the Taylor gas-liquid flow in a microchannel, *Chem. Eng. Sci.* 66 (2011) 6048–6056. <https://doi.org/10.1016/j.ces.2011.08.029>.
- [48] A. Ghaini, M.N. Kashid, D.W. Agar, Effective interfacial area for mass transfer in the liquid-liquid slug flow capillary microreactors, *Chem. Eng. Process. Process Intensif.* 49 (2010) 358–366. <https://doi.org/10.1016/j.cep.2010.03.009>.
- [49] M. Sattari-Najafabadi, M. Nasr Esfahany, Z. Wu, B. Sundén, Hydrodynamics and mass transfer in liquid-liquid non-circular microchannels: Comparison of two aspect ratios and three junction structures, *Chem. Eng. J.* 322 (2017) 328–338. <https://doi.org/10.1016/j.cej.2017.04.028>.
- [50] C. Butler, B. Lalanne, K. Sandmann, E. Cid, A.M. Billet, Mass transfer in Taylor flow: Transfer rate modelling from measurements at the slug and film scale, *Int. J. Multiph. Flow.* 105 (2018) 185–201. <https://doi.org/10.1016/j.ijmultiphaseflow.2018.04.005>.
- [51] Y. Liu, Q. Zhao, J. Yue, C. Yao, G. Chen, Effect of mixing on mass transfer characterization in continuous slugs and dispersed droplets in biphasic slug flow microreactors, *Chem. Eng. J.* 406 (2021) 126885. <https://doi.org/10.1016/j.cej.2020.126885>.
- [52] Z. Xu, T. Wang, J. Wu, L. Wang, X. Zhang, H. Dong, C. Sun, Mass Transfer Characteristics of CO₂ and Blended Aqueous Solutions of [C₂OHmim][Lys]/MDEA in a Microchannel, *Ind. Eng. Chem. Res.* 62 (2023) 8926–8938.

- <https://doi.org/10.1021/acs.iecr.2c04407>.
- [53] Y. Liu, J. Yue, C. Xu, S. Zhao, C. Yao, G. Chen, Hydrodynamics and local mass transfer characterization under gas–liquid–liquid slug flow in a rectangular microchannel, *AIChE J.* 66 (2020) 1–13. <https://doi.org/10.1002/aic.16805>.
- [54] P. Plouffe, D.M. Roberge, A. Macchi, Liquid-liquid flow regimes and mass transfer in various micro-reactors, *Chem. Eng. J.* 300 (2016) 9–19. <https://doi.org/10.1016/j.cej.2016.04.072>.
- [55] C. Yao, Y. Zhao, J. Zheng, Q. Zhang, G. Chen, The effect of liquid viscosity and modeling of mass transfer in gas–liquid slug flow in a rectangular microchannel, *AIChE J.* 66 (2020). <https://doi.org/10.1002/aic.16934>.
- [56] N. Aoki, S. Tanigawa, K. Mae, A new index for precise design and advanced operation of mass transfer in slug flow, *Chem. Eng. J.* 167 (2011) 651–656. <https://doi.org/10.1016/j.cej.2010.07.071>.
- [57] J. Ren, S. He, C. Ye, G. Chen, C. Sun, The ozone mass transfer characteristics and ozonation of pentachlorophenol in a novel microchannel reactor, *Chem. Eng. J.* 210 (2012) 374–384. <https://doi.org/10.1016/j.cej.2012.09.011>.
- [58] A.W. Gladius, J. Vondran, Y. Ramesh, T. Seidensticker, D.W. Agar, Slug flow as tool for selectivity control in the homogeneously catalysed solvent-free epoxidation of methyl oleate, *J. Flow Chem.* 11 (2021) 407–427. <https://doi.org/10.1007/s41981-021-00199-6>.
- [59] N. Di Miceli Raimondi, L. Prat, C. Gourdon, J. Tasselli, Experiments of mass transfer with liquid-liquid slug flow in square microchannels, *Chem. Eng. Sci.* 105 (2014) 169–178. <https://doi.org/10.1016/j.ces.2013.11.009>.
- [60] L. Arsenjuk, M. Asshoff, J. Kleinheider, D.W. Agar, A device for continuous and flexible adjustment of liquid-liquid slug size in micro-channels, *J. Flow Chem.* 10 (2020) 409–422. <https://doi.org/10.1007/s41981-019-00064-7>.
- [61] B. Xu, W. Cai, X. Liu, X. Zhang, Mass transfer behavior of liquid-liquid slug flow in circular cross-section microchannel, *Chem. Eng. Res. Des.* 91 (2013) 1203–1211.

- <https://doi.org/10.1016/j.cherd.2013.01.014>.
- [62] N.J. Mozdierz, Y. Lee, M.S. Hong, M.H.P. Benisch, M.L. Rasche, U.E. Tropp, M. Jiang, A.S. Myerson, R.D. Braatz, Mathematical modeling and experimental validation of continuous slug-flow tubular crystallization with ultrasonication-induced nucleation and spatially varying temperature, *Chem. Eng. Res. Des.* 169 (2021) 275–287. <https://doi.org/10.1016/j.cherd.2021.03.026>.
- [63] M. Termühlen, M.M. Etmanski, I. Kryschewski, A.C. Kufner, G. Schembecker, K. Wohlgemuth, Continuous slug flow crystallization: Impact of design and operating parameters on product quality, *Chem. Eng. Res. Des.* 170 (2021) 290–303. <https://doi.org/10.1016/j.cherd.2021.04.006>.
- [64] M. Jiang, R.D. Braatz, Low-cost noninvasive real-time imaging for tubular continuous-flow crystallization, *Chem. Eng. Technol.* 41 (2018) 143–148. <https://doi.org/10.1002/ceat.201600276>.
- [65] N. Aoki, R. Ando, K. Mae, Gas-liquid-liquid slug flow for improving liquid-liquid extraction in miniaturized channels, *Ind. Eng. Chem. Res.* 50 (2011) 4672–4677. <https://doi.org/10.1021/ie1024326>.
- [66] S.K. Kurt, F. Warnebold, K.D.P. Nigam, N. Kockmann, Gas-liquid reaction and mass transfer in microstructured coiled flow inverter, *Chem. Eng. Sci.* 169 (2017) 164–178. <https://doi.org/10.1016/j.ces.2017.01.017>.
- [67] S. Yamasaki, K.I. Sotowa, T. Horikawa, Effect of fluid flow on crystallization in a segmented flow microchannel, *J. Chem. Eng. Japan.* 54 (2021) 603–611. <https://doi.org/10.1252/jcej.21we059>.
- [68] Y. Asano, Y. Ito, Study on a recirculation microreactor system for gas-liquid reactions, *J. Chem. Eng. Japan.* 54 (2021) 541–548. <https://doi.org/10.1252/jcej.21we055>.
- [69] Susanti, J.G.M. Winkelman, B. Schuur, H.J. Heeres, J. Yue, Lactic Acid Extraction and Mass Transfer Characteristics in Slug Flow Capillary Microreactors, *Ind. Eng. Chem. Res.* 55 (2016) 4691–4702. <https://doi.org/10.1021/acs.iecr.5b04917>.
- [70] Y. Hirayama, M. Hinoue, H. Tokumoto, A. Matsuoka, K. Noishiki, A. Muto, Liquid-

- liquid extraction and separation of cobalt and lithium ions using a slug flow microreactor, *J. Chem. Eng. Japan*. 51 (2018) 222–228.
<https://doi.org/10.1252/jcej.17we152>.
- [71] G. Ochoa-Vazquez, B. Kharisov, A. Arizmendi-Morquecho, A. Cario, C. Aymonier, S. Marre, I. Lopez, Continuous Segmented-Flow Synthesis of Ag and Au Nanoparticles Using a Low Cost Microfluidic PTFE Tubing Reactor, *IEEE Trans. Nanobioscience*. 21 (2022) 135–140. <https://doi.org/10.1109/TNB.2021.3101189>.
- [72] H. Huang, H. Du Toit, S. Ben-Jaber, G. Wu, L. Panariello, N.T.K. Thanh, I.P. Parkin, A. Gavriilidis, Rapid synthesis of gold nanoparticles with carbon monoxide in a microfluidic segmented flow system, *React. Chem. Eng.* 4 (2019) 884–890.
<https://doi.org/10.1039/c8re00351c>.
- [73] S. Duraiswamy, S.A. Khan, Droplet-based microfluidic synthesis of anisotropic metal nanocrystals, *Small*. 5 (2009) 2828–2834. <https://doi.org/10.1002/sml.200901453>.
- [74] V. Sebastian, C.D. Smith, K.F. Jensen, Shape-controlled continuous synthesis of metal nanostructures, *Nanoscale*. 8 (2016) 7534–7543. <https://doi.org/10.1039/c5nr08531d>.
- [75] M. Termühlen, B. Strakeljahn, G. Schembecker, K. Wohlgemuth, Characterization of slug formation towards the performance of air-liquid segmented flow, *Chem. Eng. Sci.* 207 (2019) 1288–1298. <https://doi.org/10.1016/j.ces.2019.07.033>.
- [76] T. Abadie, J. Aubin, D. Legendre, C. Xuereb, Hydrodynamics of gas-liquid Taylor flow in rectangular microchannels, *Microfluid. Nanofluidics*. 12 (2012) 355–369.
<https://doi.org/10.1007/s10404-011-0880-8>.
- [77] P. Garstecki, M.J. Fuerstman, H.A. Stone, G.M. Whitesides, Formation of droplets and bubbles in a microfluidic T-junction - Scaling and mechanism of break-up, *Lab Chip*. 6 (2006) 437–446. <https://doi.org/10.1039/b510841a>.
- [78] K. Miyabayashi, O. Tonomura, S. Hasebe, Estimation of gas and liquid slug lengths for T-shaped microreactors, *Chem. Eng. J.* 262 (2015) 1137–1143.
<https://doi.org/10.1016/j.cej.2014.10.075>.
- [79] Y. Kawakami, N. Kadowaki, K. Suzumori, Y. Sakata, E. Fujii, Development of micro

- sliding valve for micro chemical reactors and its application to micro beaker process, 2012 19th Int. Conf. Mechatronics Mach. Vis. Pract. M2VIP 2012. (2012) 495–499.
- [80] N. Kadowaki, K. Suzumori, Y. Kawakami, Y. Sakata, Micro-beaker chemical process using a slide type three-port valve system for slug flow generation, *Kagaku Kogaku Ronbunshu*. 40 (2014) 38–42. <https://doi.org/10.1252/kakoronbunshu.40.38>.
- [81] Y. Kawaguchi, N. Kadowaki, K. Suzumori, A. Muto, M. Kawakami, Achievement of chemical process by active slug flow using micro valve, *Trans. Japan Soc. Mech. Eng.* (2009).
- [82] N. Kadowaki, K. Suzumori, A. Muto, Three-Port Valve to Generate Length-Controllable Slug Flow for Chemical Process, *Trans. Japan Soc. Mech. Eng. Part C*. 76 (2010) 266–272.
- [83] N. Kadowaki, K. Suzumori, A. Muto, Development of active separation system for slug flow in chemical process, *Trans. Japan Soc. Mech. Eng. Part C*. 77 (2011) 1109–1118. <https://doi.org/10.1299/kikaic.77.1109>.
- [84] Y. Zhang, J. Zhang, Z. Tang, Q. Wu, Regulation of gas-liquid Taylor flow by pulsating gas intake in micro-channel, *Chem. Eng. J.* 417 (2021) 129055. <https://doi.org/10.1016/j.cej.2021.129055>.
- [85] S.L. Gawali, S.B. Shelar, J. Gupta, K.C. Barick, P.A. Hassan, Immobilization of protein on Fe₃O₄ nanoparticles for magnetic hyperthermia application, *Int. J. Biol. Macromol.* 166 (2021) 851–860. <https://doi.org/10.1016/j.ijbiomac.2020.10.241>.
- [86] S. Tang, M. Zhao, D. Yuan, X. Li, Z. Wang, X. Zhang, T. Jiao, J. Ke, Fe₃O₄ nanoparticles three-dimensional electro-peroxydisulfate for improving tetracycline degradation, *Chemosphere*. 268 (2021) 129315. <https://doi.org/10.1016/j.chemosphere.2020.129315>.
- [87] J. Zhang, Y. Ji, P. Wang, Q. Shao, Y. Li, X. Huang, Adsorbing and activating N₂ on heterogeneous Au-Fe₃O₄ nanoparticles for N₂ fixation, *Adv. Funct. Mater.* 30 (2020) 1906579. <https://doi.org/10.1002/adfm.201906579>.
- [88] A. Rajan, M. Sharma, N.K. Sahu, Assessing magnetic and inductive thermal properties

- of various surfactants functionalised Fe₃O₄ nanoparticles for hyperthermia, *Sci. Rep.* 10 (2020) 1–15. <https://doi.org/10.1038/s41598-020-71703-6>.
- [89] J. Yu, F. Zhao, W. Gao, X. Yang, Y. Ju, L. Zhao, W. Guo, J. Xie, X.J. Liang, X. Tao, J. Li, Y. Ying, W. Li, J. Zheng, L. Qiao, S. Xiong, X. Mou, S. Che, Y. Hou, Magnetic reactive oxygen species nanoreactor for switchable magnetic resonance imaging guided cancer therapy based on pH-sensitive Fe₅C₂@Fe₃O₄ nanoparticles, *ACS Nano*. 13 (2019) 10002–10014. <https://doi.org/10.1021/acsnano.9b01740>.
- [90] S. Venkateswarlu, M. Yoon, M.J. Kim, An environmentally benign synthesis of Fe₃O₄ nanoparticles to Fe₃O₄ nanoclusters: Rapid separation and removal of Hg(II) from an aqueous medium, *Chemosphere*. 286 (2022) 131673. <https://doi.org/10.1016/j.chemosphere.2021.131673>.
- [91] H.M.A. Sharif, A. Mahmood, H.Y. Cheng, R. Djellabi, J. Ali, W.L. Jiang, S. Sen Wang, M.R. Haider, N. Mahmood, A.J. Wang, Fe₃O₄ nanoparticles coated with EDTA and Ag nanoparticles for the catalytic reduction of organic dyes from wastewater, *ACS Appl. Nano Mater.* 2 (2019) 5310–5319. <https://doi.org/10.1021/acsanm.9b01250>.
- [92] M.D. Nguyen, H.V. Tran, S. Xu, T.R. Lee, Fe₃O₄ nanoparticles: Structures, synthesis, magnetic properties, surface functionalization, and emerging applications, *Appl. Sci.* 11 (2021) 11301. <https://doi.org/10.3390/app112311301>.
- [93] M. Lübke, N.M. Makwana, R. Gruar, C. Tighe, D. Brett, P. Shearing, Z. Liu, J.A. Darr, High capacity nanocomposite Fe₃O₄/Fe anodes for Li-ion batteries, *J. Power Sources*. 291 (2015) 102–107. <https://doi.org/10.1016/j.jpowsour.2015.04.100>.
- [94] S. Zhang, X. Zhao, H. Niu, Y. Shi, Y. Cai, G. Jiang, Superparamagnetic Fe₃O₄ nanoparticles as catalysts for the catalytic oxidation of phenolic and aniline compounds, *J. Hazard. Mater.* 167 (2009) 560–566. <https://doi.org/10.1016/j.jhazmat.2009.01.024>.
- [95] J. Ge, Y. Hu, M. Biasini, W.P. Beyermann, Y. Yin, Superparamagnetic magnetite colloidal nanocrystal clusters, *Angew. Chemie - Int. Ed.* 46 (2007) 4342–4345. <https://doi.org/10.1002/anie.200700197>.
- [96] K. Petcharoen, A. Sirivat, Synthesis and characterization of magnetite nanoparticles via

- the chemical co-precipitation method, *Mater. Sci. Eng. B.* 177 (2012) 421–427.
<https://doi.org/10.1016/j.mseb.2012.01.003>.
- [97] J. Baumgartner, A. Dey, P.H.H. Bomans, C. Le Coadou, P. Fratzl, N.A.J.M. Sommerdijk, D. Faivre, Nucleation and growth of magnetite from solution, *Nat. Mater.* 12 (2013) 310–314. <https://doi.org/10.1038/nmat3558>.
- [98] N.T.K. Thanh, N. Maclean, S. Mahiddine, Mechanisms of nucleation and growth of nanoparticles in solution, *Chem. Rev.* 114 (2014) 7610–7630.
<https://doi.org/10.1021/cr400544s>.
- [99] S.M. Dadfar, K. Roemhild, N.I. Drude, S. von Stillfried, R. Knüchel, F. Kiessling, T. Lammers, Iron oxide nanoparticles: Diagnostic, therapeutic and theranostic applications, *Adv. Drug Deliv. Rev.* 138 (2019) 302–325. <https://doi.org/10.1016/j.addr.2019.01.005>.
- [100] T. Ozkaya, M.S. Toprak, A. Baykal, H. Kavas, Y. Köseoğlu, B. Aktaş, Synthesis of Fe₃O₄ nanoparticles at 100 °C and its magnetic characterization, *J. Alloys Compd.* 472 (2009) 18–23. <https://doi.org/10.1016/j.jallcom.2008.04.101>.
- [101] C.C. Lin, J.M. Ho, M.S. Wu, Continuous preparation of Fe₃O₄ nanoparticles using a rotating packed bed: Dependence of size and magnetic property on temperature, *Powder Technol.* 274 (2015) 441–445. <https://doi.org/10.1016/j.powtec.2015.01.013>.
- [102] H.L. Fan, S.F. Zhou, J. Gao, Y.Z. Liu, Continuous preparation of Fe₃O₄ nanoparticles through Impinging Stream-Rotating Packed Bed reactor and their electrochemistry detection toward heavy metal ions, *J. Alloys Compd.* 671 (2016) 354–359.
<https://doi.org/10.1016/j.jallcom.2016.02.062>.
- [103] H.L. Fan, S.F. Zhou, G.S. Qi, Y.Z. Liu, Continuous preparation of Fe₃O₄ nanoparticles using impinging stream-rotating packed bed reactor and magnetic property thereof, *J. Alloys Compd.* 662 (2016) 497–504. <https://doi.org/10.1016/j.jallcom.2015.12.025>.
- [104] H.L. Fan, L. Li, S.F. Zhou, Y.Z. Liu, Continuous preparation of Fe₃O₄ nanoparticles combined with surface modification by L-cysteine and their application in heavy metal adsorption, *Ceram. Int.* 42 (2016) 4228–4237.
<https://doi.org/10.1016/j.ceramint.2015.11.098>.

- [105] L. Zou, B. Huang, X. Zheng, H. Pan, Q. Zhang, W. Xie, Z. Zhao, X. Li, Microfluidic synthesis of magnetic nanoparticles in droplet-based microreactors, *Mater. Chem. Phys.* 276 (2022) 125384. <https://doi.org/10.1016/j.matchemphys.2021.125384>.
- [106] Atomic Layer Deposition (ALD) Valves, (n.d.). <https://www.swagelok.com/>.
- [107] Z.R. He, S.T. Luo, C.S. Liu, X.H. Jie, W.Q. Lian, Hierarchical micro/nano structure surface fabricated by electrical discharge machining for anti-fouling application, *J. Mater. Res. Technol.* 8 (2019) 3878–3890. <https://doi.org/10.1016/j.jmrt.2019.06.051>.
- [108] H.I. Madsen, J. Vollertsen, T. Hvitved-Jacobsen, Air-water mass transfer and tracer gases in stormwater systems, *Water Sci. Technol.* 56 (2007) 267–275. <https://doi.org/10.2166/wst.2007.461>.
- [109] L. Yang, N. Dietrich, K. Loubière, C. Gourdon, G. Hébrard, Visualization and characterization of gas–liquid mass transfer around a Taylor bubble right after the formation stage in microreactors, *Chem. Eng. Sci.* 143 (2016) 364–368. <https://doi.org/10.1016/j.ces.2016.01.013>.
- [110] C. Yao, Z. Dong, Y. Zhao, G. Chen, Gas-liquid flow and mass transfer in a microchannel under elevated pressures, *Chem. Eng. Sci.* 123 (2015) 137–145. <https://doi.org/10.1016/j.ces.2014.11.005>.
- [111] J. Tan, Y.C. Lu, J.H. Xu, G.S. Luo, Mass transfer characteristic in the formation stage of gas-liquid segmented flow in microchannel, *Chem. Eng. J.* 185–186 (2012) 314–320. <https://doi.org/10.1016/j.cej.2012.01.054>.
- [112] H. Zhao, S. Liu, M. Shang, Y. Su, Direct oxidation of benzene to phenol in a microreactor: Process parameters and reaction kinetics study, *Chem. Eng. Sci.* 246 (2021) 116907. <https://doi.org/10.1016/j.ces.2021.116907>.
- [113] G. Asab, E.A. Zereffa, T. Abdo Seghne, Synthesis of silica-coated Fe₃O₄ nanoparticles by microemulsion method: characterization and evaluation of antimicrobial activity, *Int. J. Biomater.* (2020) 4783612. <https://doi.org/10.1155/2020/4783612>.
- [114] R.Y. Hong, J.H. Li, H.Z. Li, J. Ding, Y. Zheng, D.G. Wei, Synthesis of Fe₃O₄ nanoparticles without inert gas protection used as precursors of magnetic fluids, *J. Magn.*

Magn. Mater. 320 (2008) 1605–1614. <https://doi.org/10.1016/j.jmmm.2008.01.015>.

- [115] M. Whitfield, The hydrolysis of ammonium ions in sea water-a theoretical study, J. Mar. Biol. Assoc. United Kingdom. 54 (1974) 565–580.
<https://doi.org/10.1017/S002531540002275X>.

Supplementary Materials

A: Control logic of high-speed valve

To realize the function of the control valve, the control scheme in Fig. A-1 is designed. There are two loops in the scheme:

1. The Raspberry Pi provide a 5 V power supply to an optical coupler (フォトカプ
ラ).
2. The optical coupler and the transistor became conductive successively, then the control valve gets a 24 V power supply and opens.

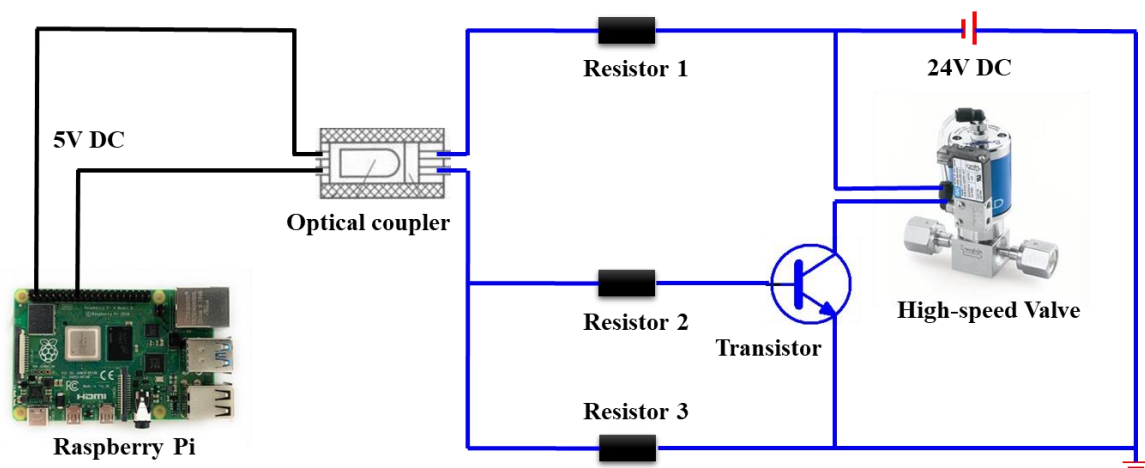


Fig. A-1 Control logic of the ALD valve

Since that the frequency and the duration time of the 5 V power supply to the optical coupler can be controlled by a program (Fig. A-2) on the Raspberry Pi, so the voltage across the control valve can vary like the waveform in Fig. A-3. Both the period T and

the power supply duration time in each period can be regulated in the Raspberry Pi program.

```
led1.py**
1 import RPi.GPIO as GPIO
2 import time
3
4
5 GPIO.setmode(GPIO.BCM)
6
7
8 led_pin = 4
9 GPIO.setup(led_pin, GPIO.OUT)
10
11 led1 = GPIO.PWM(led_pin,27.5)
12 led1.start(60)
13
14 time.sleep(100000)
15
16
17 led1.stop()
18 GPIO.cleanup()
19
```

Fig. A-2 Python code for controlling the ALD valve

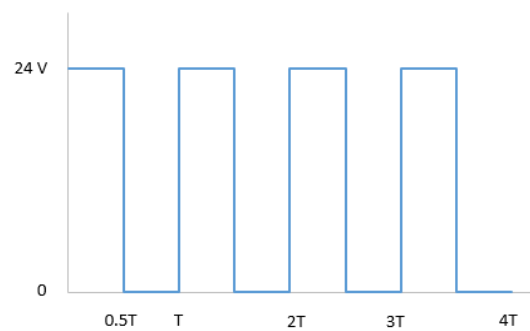


Fig. A-3 Voltage variation across the control valve

Therefore, once the program is executed on the Raspberry Pi, the control valve will cyclically open and close. This action directly impacts the volume of air entering the junction, consequently affecting the eventual length of the segment.

B: Strategy for stable segmented flow generation

In most of the conditions, the formation of segmented flow was continuous, as is shown in Fig.B-1 (a). Whereas, it was observed that sometimes the formation of segmented flow was not continuous during the experiment. In some conditions, the segmented flow in the output channel suddenly stop to move on, and the liquid phase began to flow into the tube of the gas phase, as is shown in Fig.B-1 (b). After a period, the liquid phase in the gas tube was exhausted out and the segmented flow in the output channel continued to form and moved on.

Hence there should be some parameters that can influence the continuous formation of segmented flow, it is of paramount importance to find them out.

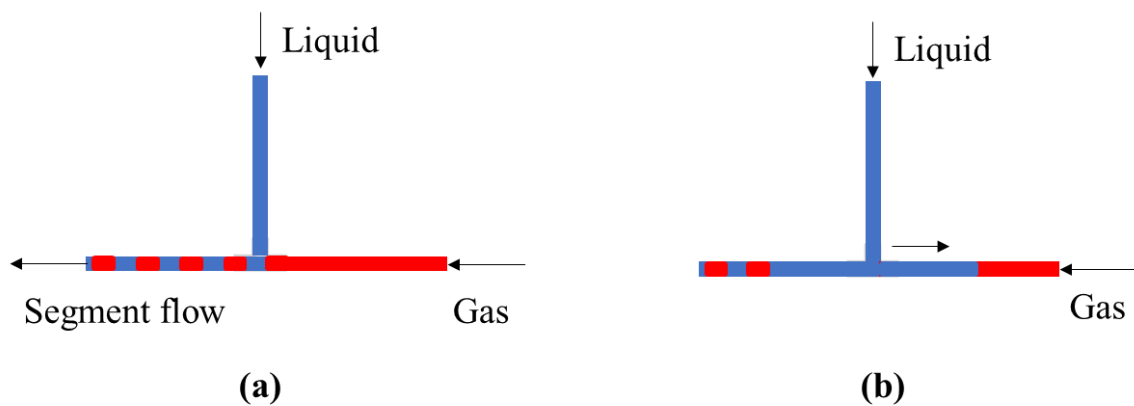


Fig. B-1 Flow status near T-junction under different conditions

B-1 Influence of gas pressure on segmented flow formation under low liquid flowrate

The first time the unstable phenomenon occurs when the liquid flowrate was reduced to 1.5 mL/min, it was obviously observed that the liquid phase flow into the gas phase feed tube. It indicated that the gas pressure p_g was less than the liquid pressure p_l , so the gas pressure was adjusted to different values to investigate the influence of gas pressure on the formation of segmented flow, the results was shown in Table B-1.

Table B-1 Influence of gas pressure on segmented flow formation under low liquid flow rate

<u>Liquid</u>		<u>Gas</u>		<u>Duration Time</u>	
Pressure (MPa)	Flow rate (mL/min)	Pressure (MPa)	Flow rate (mL/min)	T_C^{*1} (s)	T_I^{*2} (s)
0.5	1.5	0.17	2.0	50	35
0.5	1.5	0.34	2.0	64	30
0.5	1.5	0.51	2.0	63	30

*1. T_C – the duration time of continuous segmented flow formation in the outlet microchannel.

*2. T_I -- the duration time from the liquid flow into the gas tube till being exhausted from the gas tube.

As is shown in Table B-1, three different gas pressure was investigated, there was no obvious difference between the T_C and T_I at 0.34 MPa and 0.51 MPa; whereas the T_C decreased while the T_I increased at 0.17 MPa. So it seemed that gas pressure was not the key parameter for the occurrence of the interruption.

B-2 Influence of liquid flowrate on segmented flow formation

As the interruption occurred when liquid flowrate decreased to 1.5 mL/min, so the liquid flowrate was increased to 1.6 mL/min and 1.7 mL/min to investigate the influence of liquid flowrate on the formation of segmented flow, the results was shown in Table B-2.

Table B-2 Influence of liquid flow rate on segmented flow formation

<u>Liquid</u>		<u>Gas</u>		<u>Duration Time</u>	
Pressure (MPa)	Flow rate (mL/min)	Pressure (MPa)	Flow rate (mL/min)	T_C (s)	T_I (s)
0.5	1.5	0.51	2.0	63	30
0.5	1.6	0.51	2.0	++ ^{*3}	0
0.5	1.7	0.51	2.0	++	0

*3. ‘++’ means the formation of segmented flow continues without interruption.

It can be seen that, when the liquid flowrate is higher than 1.6 mL/min, the formation of segmented flow became continuous. Therefore, the liquid flowrate is one of the key parameters impact the formation of continuous segmented flow.

B-3 Influence of gas pressure on segmented flow formation under higher liquid flowrate

Table B-3 Influence of gas pressure on segmented flow formation under higher liquid flow rate

<u>Liquid</u>		<u>Gas</u>		<u>Duration Time</u>	
Pressure	Flow rate	Pressure	Flow rate	T_c	T_1
(MPa)	(mL/min)	(MPa)	(mL/min)	(s)	(s)
0.5	1.6	0.51	2.0	++	0
0.5	1.6	0.34	2.0	++	0
0.5	1.6	0.17	2.0	++	0

Table B-3 shows the influence of gas pressure on segmented flow formation at liquid flowrate of 1.6 mL/min, and the results manifested that continuous segmented flow can be obtained with the variation of gas pressure from 0.17 MPa to 0.51 MPa, which enhanced the conclusion that gas pressure was not the key parameter for the occurrence of the interruption.

B-4 Influence of gas flow rate on segmented flow formation under higher liquid flow rate

Table B-4 Influence of gas flow rate on segmented flow formation under higher liquid flow rate

<u>Liquid</u>		<u>Gas</u>		<u>Duration Time</u>	
Pressure	Flow rate	Pressure	Flow rate	T_c	T_l
(MPa)	(mL/min)	(MPa)	(mL/min)	(s)	(s)
0.5	1.6	0.17	2.0	++	0
0.5	1.6	0.17	1.5	++	0
0.5	1.6	0.17	1.0	88	36

Furthermore, the influence of gas flowrate on segmented flow formation was studied under liquid flowrate was 1.6 mL/min and the results are listed in Table 4. Even under low gas pressure (0.17 MPa), sustained segmented flow generation could be acquired when gas flowrate not lower than 1.5 mL/min; but when the gas flowrate was too low, maybe due to it was not able to maintain the gas pressure near the T-junction while the consumption of gas for the formation of the segmented flow, so the interruption appeared until the gas pressure built up.

B-5 Repetitive experiments

The experiments above were carried out on the same day, and lowest liquid flowrate was 1.5 mL/min under which the interruption just occurred. To get sufficient evidence for indicating the interruption was not casually phenomenon, expanding experiment B-2 to lower liquid flowrate is necessary.

Whereas, when experiment B-2 was repeated under liquid flowrate of 1.5 mL/min, it was curious to observe continuous segmented flow in the outlet channel, without any interruption definitely, even after the liquid flowrate was reduced to 1.4 or 1.3 mL/min, it had no influence on the flow status in the outlet channel.

After checking the whole outlet channel, something unnormal was found in the midpiece, the uniformed segmented flow formed in the T-junction merged with each other and formed new segmented flow with random slug length (see Fig. B-2). This phenomenon might attribute to the impurity components in the feed flow, which adhere to the inner wall of the channel and accumulated. As a consequence, the interforce between the tube wall and fluid changed, and the short-segmented flow could not be maintained while passing by this region.

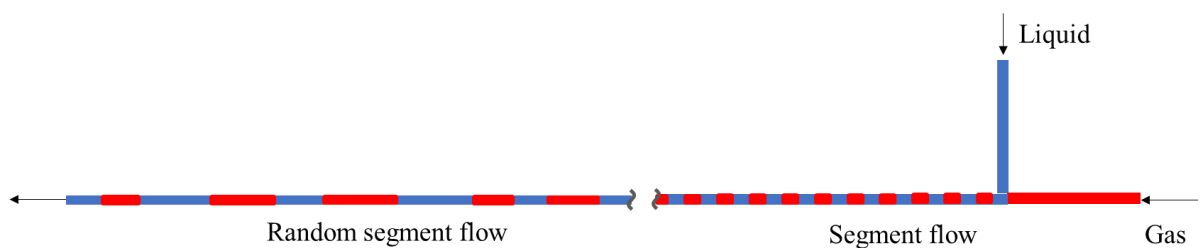


Fig. B-2 Unnormal flow status in midpiece of outlet channel

In order to confirm the assumption about the impurity components, the outlet channel was washed by alcohol, then experiment B-2 was repeated again under liquid flowrate of

1.5 mL/min, and the flow status of segmented flow in outlet channel recovered, the slug length kept the same in the whole flow path, meanwhile the interruption also occurred again. Subsequently, experiment B-2 was repeated under different liquid flowrate, the results were shown in Table B-5.

Table B-5 Influence of liquid flow rate on segmented flow formation (Repetitive experiments)

<u>Liquid</u>		<u>Gas</u>		<u>Duration Time</u>	
Pressure	Flow rate	Pressure	Flow rate	T_c	T_l
(MPa)	(mL/min)	(MPa)	(mL/min)	(s)	(s)
0.5	1.2	0.51	2.0	55	26
0.5	1.3	0.51	2.0	47	30
0.5	1.4	0.51	2.0	45	31
0.5	1.5	0.51	2.0	40	34
0.5	1.6	0.51	2.0	++	0
0.5	1.7	0.51	2.0	++	0

The results of the repetitive experiments indicated that liquid flowrate was a significant parameter for continuous segmented flow formation, to obtain persistent segmented flow formation, the liquid flowrate was recommended to higher than 1.6 mL/min in the condition of experiment B-2.

List of Tables

Table 1.1 Parameters of organolithium reaction in batch and micro-reactor [25].....	5
Table 1.2 Typical correlations for predicting segment length	17
Table 2.1 Apparatus and instruments used in this study.....	29
Table 2.2 Chemicals used in this study.....	33
Table 2.3 Segment lengths obtained using different measurement methods.....	34
Table 3.1 Segment lengths obtained without the high-speed valve.....	41
Table 4.1 Comparison of k_{LA} and k_L with literature.....	67
Table 5.1 Parameters of different experiments	76
Table 5.2 Crystal size of samples in Fig. 5.2(b) determined using the Scherrer equation	78
Table 5.3 Calculation of productivity in different processes.....	89
Table 6.1 Reaction products obtained under the different experimental conditions	96
Table 6.2 Crystal sizes calculated by the Scherrer equation in the different experiments	98
Table B-1 Influence of gas pressure on segmented flow formation under low liquid flow rate	132
Table B-2 Influence of liquid flow rate on segmented flow formation.....	133
Table B-3 Influence of gas pressure on segmented flow formation under higher liquid flow rate.....	134
Table B-4 Influence of gas flow rate on segmented flow formation under higher liquid	

flow rate.....	135
Table B-5 Influence of liquid flow rate on segmented flow formation (Repetitive experiments)	137

List of Figures

Fig. 1.1 Schematic of the compact heat sink incorporated into an integrated circuit chip	2
Fig. 1.2 The first microfabricated reactor by DuPont.....	2
Fig. 1.3 Corning G1 reactor (155×125 mm)	3
Fig. 1.4 Ehrfeld's modular microreaction system	3
Fig. 1.5. Flow pattern transitions in microchannels initially saturated with oil as a function of oil and water velocities	7
Fig. 1.6. Typical flow patterns observed in the microchannel with 1.2mm inner diameter and at 0.5 °C	8
Fig. 1.7. Continuous Gas-Liquid-Solid segmented flow for PET-RAFT polymerization	9
Fig. 1.8. Formation of segment at a planar T-junction	10
Fig. 1.9. Velocity field of the G-L-S segmented flow in capillary tube.....	11
Fig. 1.10. Mass transfer in Gas-Liquid segmented flow	13
Fig. 1.11. Gas-liquid segmented flow for synthesizing shape-controlled Pt nanocrystals	14
Fig. 1.12. Average segmented length at different flow rate.....	16
Fig. 1.13. The application of three-port valve for segmented flow generation	18
Fig. 1.14. Bubble and liquid segment lengths with different pulsating frequencies	18
Fig. 1.15. Image and schematic of the generator and geometric parameters	19

Fig. 1.16. Conventional batch process for Fe ₃ O ₄ nanoparticle synthesis	21
Fig. 1.17. Continuous synthesis of Fe ₃ O ₄ nanoparticle in packed-bed reactor	22
Fig. 1.18. Continuous synthesis of Fe ₃ O ₄ nanoparticle in microfluidic chip	23
Fig. 2.1 Image and structure of the ALD valve	30
Fig. 2.2 (a) Schematic of segmented flow generating system; (b) Configuration of T-junction and PFA tube.....	32
Fig. 2.3 Image of the T-junction	32
Fig. 2.4 Measurement methods for segmented flow	34
Fig. 2.5 Schematic of experimental setup for mass transfer measurement	36
Fig. 3.1 Segment images obtained at various high-speed valve frequencies	42
Fig. 3.2 Influence of valve frequency on segment length	43
Fig. 3.3 Reproducibility of segment length control at various high-speed valve frequencies.....	44
Fig. 3.4 Influence of higher valve frequencies on segment length.....	45
Fig. 3.5 Segment images at higher valve frequencies	46
Fig. 3.6 Qualitative analysis of gas velocity variation at different valve frequencies.....	48
Fig. 3.7 Influence of flow rate on segment length at a high-speed valve frequency of 8 s ⁻¹	50
Fig. 3.8 Images of the segmented flow at different valve frequencies	51
Fig. 3.9 Influence of valve frequency on the segment length.....	52
Fig. 3.10 Performance of the correlation for predicting segment length at low flow rate	54

Fig. 3.11 Performance of the correlation for predicting the segment length at higher flow rate	55
Fig. 4.1 Mass transfer performance at different valve frequencies	58
Fig. 4.2 Influence of tube length on $[k_{LA}]_{overall}$	60
Fig. 4.3. Influence of the tube length on $[k_{LA}]_s$	61
Fig. 4.4 Influence of valve frequency on $[k_{LA}]_s$	63
Fig. 4.5 Influence of segment length on $[k_{LA}]_s$	63
Fig. 4.6 Influence of valve frequency on a	65
Fig. 4.7 Performance of the correlation for predicting a	65
Fig. 4.8 Influence of valve frequency on $[k_L]_s$	66
Fig. 5.1 Schematic of the experimental setup.....	72
Fig. 5.2 (a) Image of nanoFe ₃ O ₄ ; (b) XRD patterns of nanoFe ₃ O ₄ synthesized by the batch method and segmented flow with conditions (1)-(3) in Table 5.1	75
Fig. 5.3 NanoFe ₃ O ₄ products in the microchannel at different iron concentrations.....	78
Fig. 5.4 SEM micrographs of Fe ₃ O ₄	80
Fig. 5.5 TEM images and average diameters of nanoFe ₃ O ₄ synthesis at different valve frequencies.....	83
Fig. 5.6 Influence of valve frequency on nanoFe ₃ O ₄ size	84
Fig. 5.7. Principles of coprecipitation in a batch reactor and segmented flow.....	85
Fig. 5.8 Comparison of segmented flow synthesis with batch and other continuous methods.....	87
Fig. 6.1 Schematic of (a) the experimental setup. (b) partially oxidation coprecipitation of Fe ²⁺ and OH ⁻ to form nano-Fe ₃ O ₄ in liquid segment	93

Fig. 6.2 XRD patterns of the Fe ₃ O ₄ nanoparticles obtained in the different experiments	97
Fig. 6.3 TEM images of Fe ₃ O ₄ nanoparticles obtained with (a) EG in FeCl ₂ aq. and (b)– (h) EG in NaOH aq. at different oxidation times	100
Fig. 6.4 Influence of oxidation time on the Fe ₃ O ₄ nanoparticle size.....	100
Fig. 6.5 Correlation between the Fe ²⁺ :Fe ³⁺ ratio and conversion at pH = 7 and pH < 7	102
Fig. 6.6 Influence of the acid additive on the Fe ₃ O ₄ nanoparticle size under different oxidation times.	103
Fig. 6.7 Fe ₃ O ₄ nanoparticle size obtained with different H ⁺ :Fe ²⁺ ratios	105
Fig. 6.8 Fe ₃ O ₄ nanoparticle sizes obtained with different OH ⁻ :Fe ²⁺ ratios.....	106
Fig. 6.9 Fe ₃ O ₄ nanoparticle sizes obtained with different OH ⁻ :Fe ²⁺ ratios.....	107
Fig. A-1 Control logic of the ALD valve.....	129
Fig. A-2 Python code for controlling the ALD valve	130
Fig. A-3 Voltage variation across the control valve.....	130
Fig. B-1 Voltage flow status near T-junction	131
Fig. B-2 Unnormal flow status in midpiece of outlet channel.....	136

List of Publications

Journals

1. Xiaoyang Jiang, Ken-Ichiro Sotowa*, Osamu Tonomura. Controlling gas–liquid segment length in microchannels using a high-speed valve. *Chemical Engineering Research and Design*, 188 (2022) 868-876. (Chapter 3)
<https://doi.org/10.1016/j.cherd.2022.10.038>
2. Xiaoyang Jiang, Ken-Ichiro Sotowa*, Osamu Tonomura, Tae Hoon Oh. Investigation of mass transfer in valve-controlled gas-liquid segmented flow. *Chemical Engineering and Processing: Process Intensification*, 194 (2023) 109578. (Chapter 4)
<https://doi.org/10.1016/j.cep.2023.109578>
3. Xiaoyang Jiang, Sihui Li, Ken-Ichiro Sotowa*, Osamu Tonomura, Tae Hoon Oh. High throughput continuous synthesis of size-controlled nanoFe₃O₄ in segmented flow. *Chemical Engineering Journal*, 471 (2023) 144546. (Chapter 5)
<https://doi.org/10.1016/j.cej.2023.144546>
4. Xiaoyang Jiang, Ken-Ichiro Sotowa*, Sihui Li, Tae Hoon Oh, Osamu Tonomura. Continuous preparation of Fe₃O₄ nanoparticle with narrow size distribution by partial oxidation coprecipitation of Fe²⁺ ion in microchannel. *Industrial & Engineering Chemistry Research*, 62 (2023) 21182-21190. (Supplementary cover) (Chapter 6)
<https://doi.org/10.1021/acs.iecr.3c01536>

Conferences

1. Xiaoyang Jiang, Ken-Ichiro Sotowa*, Osamu Tonomura. Strategy for controlling biphasic slug length in microchannel. *SCEJ Regional Meeting in Kansai 2021*. Online, Japan, December 14-15 (2021). (Chapter 3)
2. Xiaoyang Jiang, Ken-Ichiro Sotowa*, Osamu Tonomura. Mass transfer in valve-controlled gas-liquid segmented flow in microchannel. *The 16th International Microreaction Technology Conference (IMRET)*. Melbourne, Australia, November 27-30 (2022). (Chapter 4)
3. Xiaoyang Jiang, Ken-Ichiro Sotowa*, Osamu Tonomura. Investigation of mass transfer in valve-controlled multiphase segmented flow. *International Chemical Engineering Symposia 2023*. Tokyo, Japan, March 15-17 (2023). (Chapter 4)
4. Xiaoyang Jiang, Sihui Li, Ken-Ichiro Sotowa*, Osamu Tonomura, Tae Hoon Oh. Continuous synthesis of size-controlled Fe₃O₄ nanoparticles in a multiphase microreactor. *The Asian Pacific Confederation of Chemical Engineering (APCChE 2023)*. Manila, Philippines, September 5-9 (2023). (Chapter 5)
5. Xiaoyang Jiang, Ken-Ichiro Sotowa*, Sihui Li, Tae Hoon Oh, Osamu Tonomura. Continuous preparation of Fe₃O₄ nanoparticle from Fe²⁺ ions by partial oxidation coprecipitation in microreactor. *The 34th International Symposium on Chemical Engineering (ISChE 2023)*. Gyeongju, Korea, December 1-3(2023). (Chapter 6)

Acknowledgements

I would like to express my sincere gratitude to my supervisor, Professor Ken-Ichiro Sotowa. His expert guidance has been invaluable to my research endeavors. Possessing extensive expertise not only in the field of chemical engineering but also in computer and electronic sciences, he significantly expedited the design and construction of experimental systems, as well as the analysis of experimental outcomes and refinement of research strategies. Additionally, his thoughtful care for my daily well-being greatly aided in my transition to life abroad.

I extend my heartfelt appreciation to Assistant Professors Osamu Tonomura and Tae Hoon Oh. Their invaluable assistance in analyzing experimental data and reviewing papers for journal submissions has been instrumental in the progress of this research. Additionally, I am grateful to Professor Tonomura for his significant contributions in establishing the experimental system. Their support and expertise have been indispensable to the success of this study.

I'd like to take a moment to convey my appreciation to my dear friend, Li Sihui. She played a pivotal role in inspiring the application of the experimental device for nanoparticle synthesis, which became a significant portion of this thesis. Moreover, her invaluable assistance with the XRD testing of nanoparticles and the interpretation of the resulting curves has been instrumental in advancing this research.

I would also like to extend my gratitude to several other individuals. Mrs. Mai Ishibashi and Mrs. Nana Adachi, the secretaries of our lab, have been instrumental in assisting with various administrative tasks and processes at Kyoto University. Additionally, I am thankful to Professor Ryuichi Ashida and Assistant Professor Yosuke Muranaka for

providing training courses on TEM and SEM operation, ensuring that I had the necessary skills to obtain essential data for nanoparticle analysis. Lastly, my thanks go to Mr. Ryoichi Sugimoto from Swagelok for supplying the high-speed valve and providing technical support.

I am grateful for the support from KAKENHI (grant number 21H01706), which facilitated the procurement of necessary instruments and equipment for conducting the experiments in this research.

Last but certainly not least, I would like to express my deepest gratitude to my family. Their unwavering support has been a constant source of encouragement, enabling me to pursue my studies abroad with confidence. The words and actions of my parents have played a significant role in shaping my character, allowing me to navigate daily life harmoniously with others and ensuring a smooth transition to life in Japan.

JIANG XIAOYANG

Kyoto, 2023